HARVARD UNIVERSITY

THE GRADUATE SCHOOL OF ARTS AND SCIENCES

THESIS ACCEPTANCE CERTIFICATE

(To be placed in Original Copy)

The undersigned, appointed by the

Division

Department of Physics

Committee

have examined a thesis entitled
"Collective Transport and Phase Transitions in Two-Dimensional Magnetic Bubble Arrays"

presented by Junmin Hu

candidate for the degree of Doctor of Philosophy and hereby certify that it is worthy of acceptance.

Signature R.M. Westervelt

Typed name Robert M. Westervelt, Chair

Signature D.R. Nelson

Typed name David R. Nelson

Signature M. Tinkham

Typed name Michael Tinkham

Date September 4, 1996

Collective Transport and Phase Transitions in Two-Dimensional Magnetic Bubble Arrays

A thesis presented

by

Junmin Hu

to

The Department of Physics

in partial fulfillment of the requirements

for the degree of

Doctor of Philosophy

in the subject of

Physics

Harvard University

Cambridge, Massachusetts

September, 1996

ABSTRACT

This thesis presents an experimental investigation of transport phenomena and phase transitions in two-dimensional magnetic bubble arrays. Magnetic bubbles are cylindrical domains in an iron garnet, in which substrate roughness acts as a weak random pinning potential. Artificial pinning is introduced to the system using a lithographically patterned permalloy overlayer. The bubble concentration is controlled by a perpendicular dc magnetic field. Temperature is simulated with an ac field agitation. The system is directly observed using polarization microscopy and computer-video techniques.

We have studied the collective transport of magnetic bubble arrays subject to random substrate pinning. The bubble arrays are triangular arrays with quasi-long-range orientational order and short-range translational order. The bubbles are driven by a gradient dc magnetic field. The velocity-force responses follow power laws $v \propto F^{\alpha}$, with $\alpha \cong 3$ for the measured ac field range. Spatiotemporally resolved bubble array images and local velocity distributions reveal the collective nature of bubble transport: the array moves forward by correlated clusters of bubbles, and although the instantaneous individual velocity fluctuates, the spatiotemporal averaged velocity remains constant. The measured velocity-velocity correlation length ξ_v increases with the applied force F.

We have also studied the commensurate-incommensurate transitions in magnetic bubble arrays subject to periodic line pinning. Bubble array images and structure function analyses show that the commensurate-incommensurate transitions take place by rotation of array orientations as the bubble concentration decreases. Smooth migration of Bragg peaks in structure function plots indicates a continuous second (or weakly first) order transition. We have identified the commensurate and incommensurate phases that have appeared during the phase transitions, including an incommensurate polycrystalline phase and a commensurate smectic phase. Symmetry breaking phase occurs when the pinning periodicity becomes smaller than the bubble row spacing, as expected from theory.

ACKNOWLEDGEMENTS

I would like to thank everyone who has given me guidance, help, and encouragement throughout the completion of this thesis.

I am truly grateful to my advisor Bob Westervelt for teaching me the qualities necessary to become a good experimental physicist: the ability to choose interesting and fruitful research projects, the capability to explain complicated theories with simple pictures, the importance of careful design of experimental setups, and excellent verbal and written presentation skills. He has always been generous in encouraging me, giving me independence and freedom in pursing my thesis research, and introducing me to the physics community at every opportunity.

I would like to thank Professor David Nelson for the invaluable discussions I have had with him. They have always been illuminating, inspiring, and enjoyable. I have benefited tremendously from his suggestions. I would also like to thank Professor Michael Tinkham for his interest in my projects, and Professor Daniel Fisher and Professor Terrence Hwa for helpful discussions.

I am lucky to have been working with an exceptionally talented group of Westerveltians. I thank Raj Seshadri for introducing me to the bubble measurement techniques. I thank Fred Waugh, Doug Mar, John Baskey, Michael Berry, and Scott Yang for their encouragement and guidance during my early years at this group. I thank Aram Adourian, Jordan Katine, Catherine Crouch, Mark Eriksson, Carol Livermore, and Rex Beck for their help and for making this group fun.

I have benefited greatly from discussions with theorists Leon Balents, Onuttom Narayan, Joe Watson, Carlo Carraro, and Karin Dahmen. I thank Steve Shepard and Dave Carter for maintaining the Gordon McKay cleanroom. I also thank Dan Ralph and Mark Itzler for interesting conversations.

Finally, I would like to thank my family members. I thank my husband Jun Wang for his love and support. I thank my parents Huizhen Bu and Gongcheng Hu, without whom it would have been impossible for me to come to Harvard.

TABLE OF CONTENTS

ABSTRACT ..... *iii*

ACKNOWLEDGEMENTS ..... *iv*

TABLE OF CONTENTS ..... *vi*

1. INTRODUCTION 1

1.1 Domain Structures in Ferrimagnetic Garnets 2
1.2 Collective Transport and Commensurate-Incommensurate Transitions 6

2. THE PHYSICS OF MAGNETIC BUBBLES 9

2.1 Origin of Magnetization 9
2.2 Magnetic Interactions and Domain Walls 12
2.3 Magnetic Bubbles 17
2.4 Gradient Propagation of a Bubble 22
2.5 Substrate Roughness and ac Magnetic Field 26
2.6 Pinning by Permalloy Overlayer 29
2.7 Characteristics of Garnet Sample 30

3. EXPERIMENTAL METHODS 34

3.1 Nucleation and Annealing of Magnetic Bubbles 34
3.2 Observation of Magnetic Bubbles 37
3.3 Control of Magnetic Bubbles 42
3.4 Pinning of Magnetic Bubbles 45
3.5 Image Processing and Data Analysis 48

4. COLLECTIVE TRANSPORT 54

4.1 Introduction 55
4.2 Theory of Collective Transport 59
4.3 The Experiment 61
4.4 Velocity-Force Responses 66
4.5 Spatial Behavior of Bubble Transport 69

4.6 Temporal Behavior of Bubble Transport 73
4.7 Velocity-Velocity Correlations 77
4.8 Summary 78

5. COMMENSURATE-INCOMMENSURATE TRANSITIONS IN LINE-PINNED MAGNETIC BUBBLE ARRAYS 82

5.1 Introduction 83
5.2 Theory of Commensurate-Incommensurate Transitions 84
5.3 Experimental Method 89
5.4 Overview of Commensurate-Incommensurate Transitions 92
5.5 Nature of Commensurate-Incommensurate-Commensurate Transition 100
5.6 Translational Correlations 104
5.7 Even-Odd Symmetry Breaking 108
5.8 Further Discussion of Commensurate-Incommensurate Transitions 112
5.9 Summary 115

6. CONCLUSIONS 116

APPENDICES

A. SHEAR FLOW 120

B. SAMPLE CODE OF IMAGE PROCESSING AND DATA ANALYSIS APPLICATIONS 128

REFERENCES 138

CHAPTER 1 INTRODUCTION

A two-dimensional system refers to a large collection of objects arranged in a plane interacting via either short- or long-range forces. Two-dimensional statistical physics has long been an exciting field because of the many interesting phenomena. For example, two-dimensional melting is different from conventional melting in that two-dimensional melting is a dislocation-mediated two-stage melting process [Kosterlitz and Thouless, 1973; Nelson and Halperin, 1979; Young, 1979; Murray and Winkle, 1987; Seshadri and Westervelt, 1991]. In addition, two-dimensional statistical physics has close relations to more complicated three-dimensional physics. Because of the reduced degrees of freedom, it is often easier to study a two-dimensional system than a three-dimensional system both experimentally and theoretically. A grasp of two-dimensional phenomena can give insight into the nature of the three-dimensional phenomena.

Pinning has been the focus of two-dimensional statistical physics in recent years, because it significantly affects the thermodynamical and structural properties of many condensed matter systems. Pinning can be divided into two classes: random pinning and periodic pinning. In most systems, substrate roughness or impurities provide a means for random pinning, which destroys the long-range translational order of the systems and reduces the coherence of motion in transport. Random pinning leads to friction and drag. Although the macroscopic effects of friction can be well modeled, its microscopic origin is still not completely understood. Periodic pinning also exists in some systems, such as rare-gas atoms adsorbed on graphite [Chinn and Fain, 1977; Horn *et al.*, 1978; Moncton *et al.*, 1981]. Periodic pinning introduces the effect of commensurability. For weak pinning, commensurate-incommensurate transitions take place as the density or temperature of the system changes, and new commensurate and incommensurate phases may occur. Because

of the ability to directly observe bubble arrays and the similarity in interaction and pinning between the magnetic bubble system and other condensed matter systems, the two-dimensional magnetic bubble system can be used as a model system to examine the origin of friction and commensurate-incommensurate transitions.

Magnetic bubbles can be modeled as a collection of magnetic dipoles confined in a two-dimensional plane. They form a triangular array under suitable conditions. Random pinning arises naturally from the microscopic substrate roughness and periodic pinning can be introduced via a permalloy overlayer patterned on top of the bubble surface. Using the Faraday effect, the dynamics and structural evolution of the system can be captured in real time with computer-video techniques. Work on two-dimensional melting and forced flow by Seshadri and Westervelt [1991; 1993a] has successfully demonstrated the use of magnetic bubble array as a model system to study two-dimensional statistical physics. We have continued their effort and examined novel phenomena in bubble transport and array structure. In this thesis, we present experimental observations and analysis of collective transport phenomena in the magnetic bubble system subject to random substrate pinning and the commensurate-incommensurate phase transitions in the magnetic bubble system subject to periodic line pinning.

1.1 Domain Structures in Ferrimagnetic Garnets

Ferrimagnetic garnets were discovered in 1958 [Kooy, 1958]. From then to the early 1980s, ferrimagnetic garnets had attracted considerable attention from both the scientific and technology communities. Electrical engineers were interested in them because of their potential applications as computer memory and computing devices and as display and optical devices using their magneto-optical property. Physicists were interested in them because of the fascinating physics principles involved in understanding their rich behavior. Material scientists were interested in them because of challenges in the fabrication of useful

configurations [Eschenfelder, 1981; O'Dell, 1986]. However ferrimagnetic garnets eventually did not succeed as computer memory devices because of competition from large capacity hard disks. Today they are mainly used as magnetic field sensors [Mori and Asahara, 1996; Deeter, 1996], current sensors [Ko and Garmire, 1995], optical isolators [Levy *et al*, 1994], and magnetic recording media [Eppler and Kryder, 1995; Fu *et al*, 1995]. However it was the early efforts that led to an understanding of magnetic bubble physics and a well-developed magnetic bubble technology, making our magnetic bubble experiments possible.

Magnetic domains are small regions in a ferromagnetic material, within which the local magnetization is saturated. A saturated configuration refers to a configuration of the ground state of the ferromagnetic material where all electron spins and magnetic moments are parallel. The minimum magnetic field needed to maintain the material in this configuration is called the saturation field. The formation of domains is a consequence of competition between various energy contributions in a ferromagnetic body: the exchange, anisotropy, and magnetostatic energies [Landau and Lifshitz, 1935; Kittel, 1949]. Domain structure always has its origin in the possibility of lowering the energy of a system by going from a saturated configuration with high magnetic energy to a domain configuration with a lower energy. Domains exist in a ferrimagnetic garnet film as well. They can be observed directly with an optical microscope by means of the Faraday effect. Figures. 1.1(a) to 1.1(d) are Faraday contrast micrographs showing possible domain structures in a garnet film at zero perpendicular bias field and room temperature. The dark (light) regions correspond to magnetization pointing down (up). The occurrence of a particular domain structure depends on the thermomagnetic history of the sample [Molho, *et al.*, 1987]. At zero bias field and room temperature, bubbles, stripes, or a mixture of both can exist. Magnetic bubbles are cylindrical domains. Figure. 1.1(a) shows a disordered sea of magnetic bubbles prepared by applying a strong magnetic field parallel to the film plane for a brief period of time. Figure. 1.1(b) shows an ordered magnetic bubble

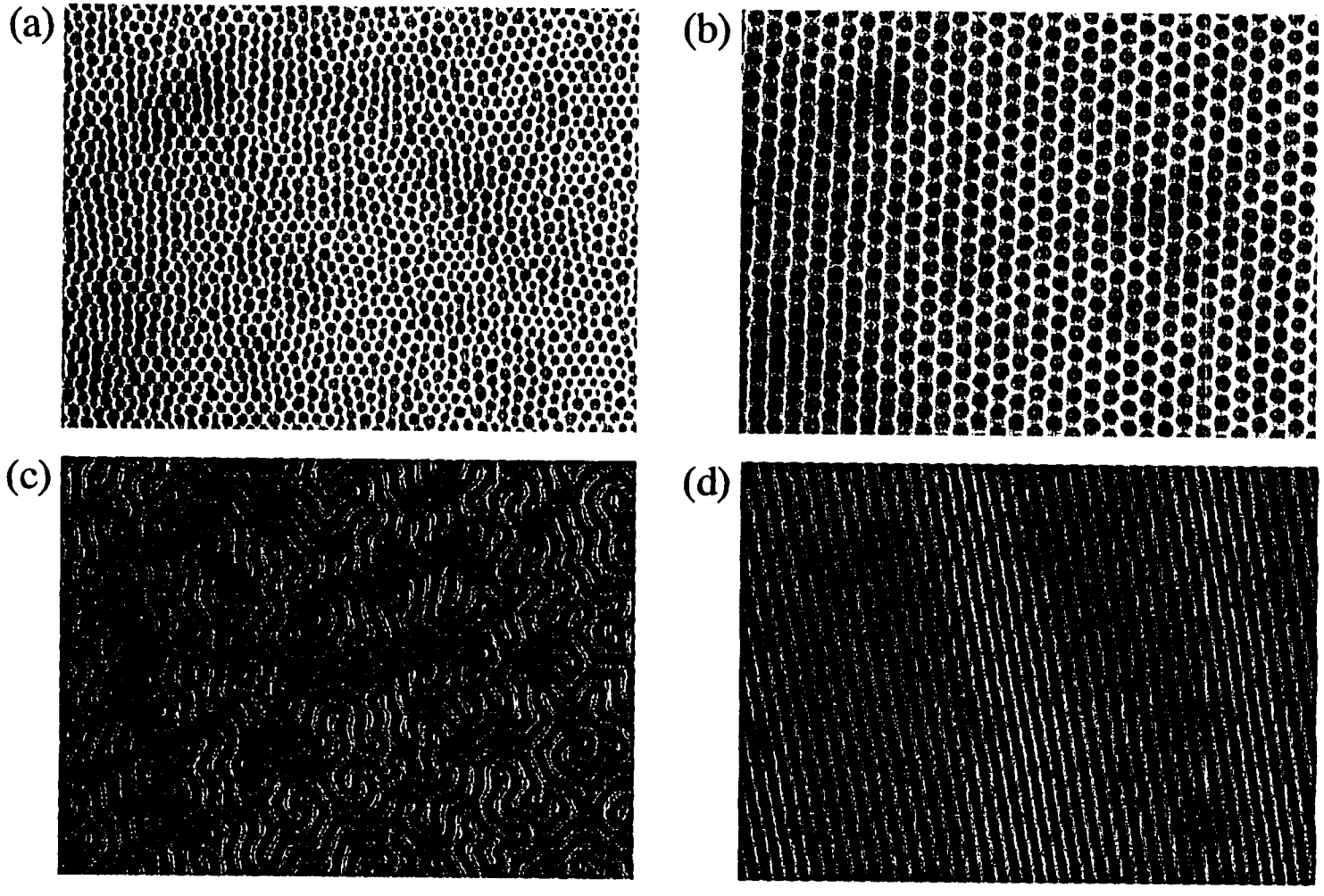

Fig. 1.1 Domain structures in a ferrimagnetic garnet film at zero bias field and room temperature. (a) Disordered magnetic bubbles. (b) Ordered magnetic bubbles. (c) Serpentine stripes. (d) Parallel stripes. Each image is 537 x 394 μm^2.

array prepared by annealing the disordered magnetic bubbles with a perpendicular ac magnetic field. Figure. 1.1(c) shows a serpentine stripe pattern prepared by lowering the applied field from the saturation magnetic field. Figure. 1.1(d) shows an array of parallel stripes prepared by cooling down from the Curie temperature in the absence of any magnetic field. At zero bias field the total area with magnetization down is approximately equal to the total area with magnetization up. When the bias field with an upward direction increases, the dark regions are unfavorable and the total area of down domains decreases while the domains themselves undergo interesting and complex topological changes. If the magnetic field is applied downward, a cellular pattern is formed [Babcock, 1989a; 1990]. A change in temperature also leads to interesting topological changes.

Domain structures in garnet films are common to many other two-dimensional experimental systems. The garnet film is an excellent model system to study two-dimensional statistical physics not only because research into magneto-optics and bubble memory provides well-developed techniques for the observation and manipulation of domains, but also because it is one of the few systems that allows direct observation and identification of topological defects via Voronoi constructions. A continuous hexatic-to-liquid melting transition as a function of bubble concentration has been observed in the two-dimensional magnetic bubble lattices [Seshadri and Westervelt, 1991; 1992c]. Seul and Murray have observed the disordering process of a bubble lattice and investigated the nature of the disorder [Seul and Murray, 1993; Seul, 1994]. With the application of an additional magnetic gradient field and permalloy pinning, Seshadri and Westervelt [1993a; 1993c] have studied the forced shear flow of a magnetic bubble array. Babcock and Westervelt have studied topological melting, coarsening, and avalanches and self-organization of the cellular patterns [Babcock and Westervelt, 1989a and 1990; Babcock, Seshadri, and Westervelt, 1990]. Investigation of two-dimensional stripe phases also reveals a defect-mediated melting transition from a well-ordered lamellar domain phase to a

globally disordered labyrinthine pattern [Seul *et al.*, 1991; Seul and Wolfe, 1992a; 1992b; 1992c].

1.2 Collective Transport and Commensurate-Incommensurate Transitions

When a uniform force is applied to a spatially extended system with random pinning, collective transport phenomena between different parts of the system occur. Collective aspects of the transport arise because the interaction forces are as important as the random and driving forces. Typical systems that demonstrate collective transport phenomena are the frictional motion of a two-dimensional membrane [Vallette and Gollub, 1993; Feder and Feder, 1991], sliding charge density wave transport [see for example, Fisher, 1987; Grüner, 1988; Coppersmith, 1990], flux flow in type II superconductors [see for example, Nelson and Vinokur, 1992; Huse, Fisher, and Fisher, 1992], motion of an interface between two fluids in porous medium [Stokes *et al.*, 1986], and motion of domain walls in disordered magnets [Bruinsma and Aeppli, 1984; Grinstein and Fernandez, 1984; Villain, 1984]. How collective transport takes place has generated considerable attention because in charge density waves and type II superconductors, it determines the conductivity of a material, while in two-dimensional membranes and random magnets, it provides a means to study how random pinning affects local and global motion and allows examination of the origin of friction.

Commensurate-incommensurate transitions occur in a variety of systems with weak periodic pinning, including rare-gas atoms adsorbed on graphite [Coppersmith *et al.*, 1981; 1982; Moncton *et al.*, 1981], thickness modulated superconducting films [Burkov and Pokrovskii, 1980; Burkov and Pokrovsky, 1981; Daldini *et al.*, 1974; Martinoli *et al.*, 1981], and layered superconductors [Balents and Nelson, 1994; 1995]. Periodic pinning induces a broken symmetry in the system. A number of new phases become possible, including a smectic phase characterized by ordering in one direction but disorder in the

perpendicular direction. The mechanism of commensurate-incommensurate transitions is still under investigation. Scattering experiments were used to examine phase transitions in rare-gas atoms adsorbed on graphite, and transport measurements were used for the thickness modulated superconducting films and layered superconductors. Both provide only spatially averaged information. We used polarization microscopy and computer-video techniques to directly observe how the phase transitions take place in bubble arrays subject to periodic line pinning.

This thesis is structured as follows: In Chapter 2 we review the physics of the magnetic bubble system, including bubble interaction, pinning, effective thermal fluctuations, and gradient field propagation. This chapter justifies why we can use the magnetic bubble system as a model system to investigate two-dimensional structures, transport behaviors, and phase transitions. In Chapter 3 we describe experimental techniques used in our experiments, including nucleation and annealing of magnetic bubbles, video polarization microscopy, control with various magnetic fields, fabrication of artificial pinning, as well as image acquisition, processing, and data analysis using computer-video setup and custom developed software. In Chapter 4 we discuss transport phenomena in the magnetic bubble array subject to random substrate potential. We examine the collective nature of the bubble transport from both macroscopic measurements, such as velocity-force response, and microscopic observations, such as spatiotemporal velocity distribution and correlations. In Chapter 5 we discuss commensurate-incommensurate transitions in the magnetic bubble system when an artificial periodic line pinning is superimposed on the system. We identify the phases which appear during the phase transitions using both direct imaging and structure function analysis. We also explore the nature of the commensurate-incommensurate transitions. In Chapter 6 we draw conclusions from our investigation and propose possible directions for future research. Two appendices are attached at the end of this thesis. In Appendix A we discuss results from shear flow measurements, in which the driving force is applied to a bubble array

where half of it is permanently pinned. In Appendix B we give typical computer codes used in image acquisition, processing, and data analysis.

CHAPTER 2 PHYSICS OF MAGNETIC BUBBLES

In this chapter we give the necessary background to understand the magnetic bubble system. First, we review the origin of the magnetization of garnet films and describe the magnetic interactions within the films. We also discuss the energetics of magnetic bubbles. Second, we explain the mechanisms for the application of external forces via magnetic gradients, permalloy pinning, and ac field agitation of the bubble array. We then summarize the properties of our garnet samples. Finally, we extract the key characteristics of the bubble system as a model two-dimensional statistical system.

2.1 Origin of Magnetization

Iron garnets can be generally described using the formula

$$\{RE_3^{3+}\}[Fe_2^{3+}](Fe_3^{3+})O_{12}. \qquad (2.1.1)$$

This is a cubic structure with three different kinds of sublattices between the oxygens: {RE} represents a dodecahedral site occupied by a rare earth and surrounded by 8 oxygens; [Fe] represents an octahedral site occupied by an iron and surrounded by 6 oxygens; (Fe) represents a tetrahedral site occupied by an iron and surrounded by 4 oxygens. In one formula unit there are three dodecahedral sites, two octahedral sites, and three tetrahedral sites. One unit cell of garnet consists of 8 formula units.

Each of the three sublattices has its own magnetization and the sum of the three sublattice magnetizations gives rise to the magnetization of the garnet film, denoted as $4\pi M_S$. Exchange coupling between the ions tends to orient each sublattice antiparallel to

the other. Because the exchange coupling between the octahedral iron and the tetrahedral iron is the strongest and the exchange coupling between the dodecahedral rare earth and the octahedral iron is the weakest, the relative orientations of the sublattice magnetizations are as shown in Fig. 2.1(a). Figure 2.1(b) shows the temperature dependence of the three sublattice magnetizations and Fig. 2.1(c) shows the temperature dependence of the magnetization of the film. The magnetization of the dodecahedral rare earth deteriorates much faster than that of the irons because of the weaker exchange coupling between the dodecahedral rare earth ions themselves. As indicated in Fig. 2.1(c), the temperature at which the net magnetization first becomes zero is called the compensation temperature T_{comp}, and the temperature at which the garnet film becomes paramagnetic is called the Curie temperature T_{Curie}. Above T_{comp} the magnetization will flip in order to align with the applied field. Room temperature T_{room} is often between T_{comp} and T_{Curie}. At T_{room} the magnetization mainly comes from the two antiparallel iron sublattices.

Other nonmagnetic ions are often introduced in order to achieve a desired property, such as larger domain size, larger Faraday rotation, or lower optical absorption. Any nonmagnetic ion that replaces Fe on tetrahedral sites reduces the magnetization $4\pi M_S$ but one that replaces Fe on the octahedral sites increases $4\pi M_S$. For example, when Ga^{3+} is substituted for Fe, ~ 90% goes on the tetrahedral sites and ~ 10% goes on the octahedral sites, therefore Ga is 80% effective in reducing $4\pi M_S$. The chemical composition of our garnet films grown at Litton Airtron is: $(Bi_{1.09}Tm_{0.07}Gd_{0.95}Y_{0.90})(Fe_{3.91}Ga_{0.76}Y_{0.30}Tm_{0.02})O_{12}$, where the first parenthesis contains dodecahedral sites and the second parenthesis contains octahedral and tetrahedral sites. Its saturation magnetization is $4\pi M_S = 190$ G.

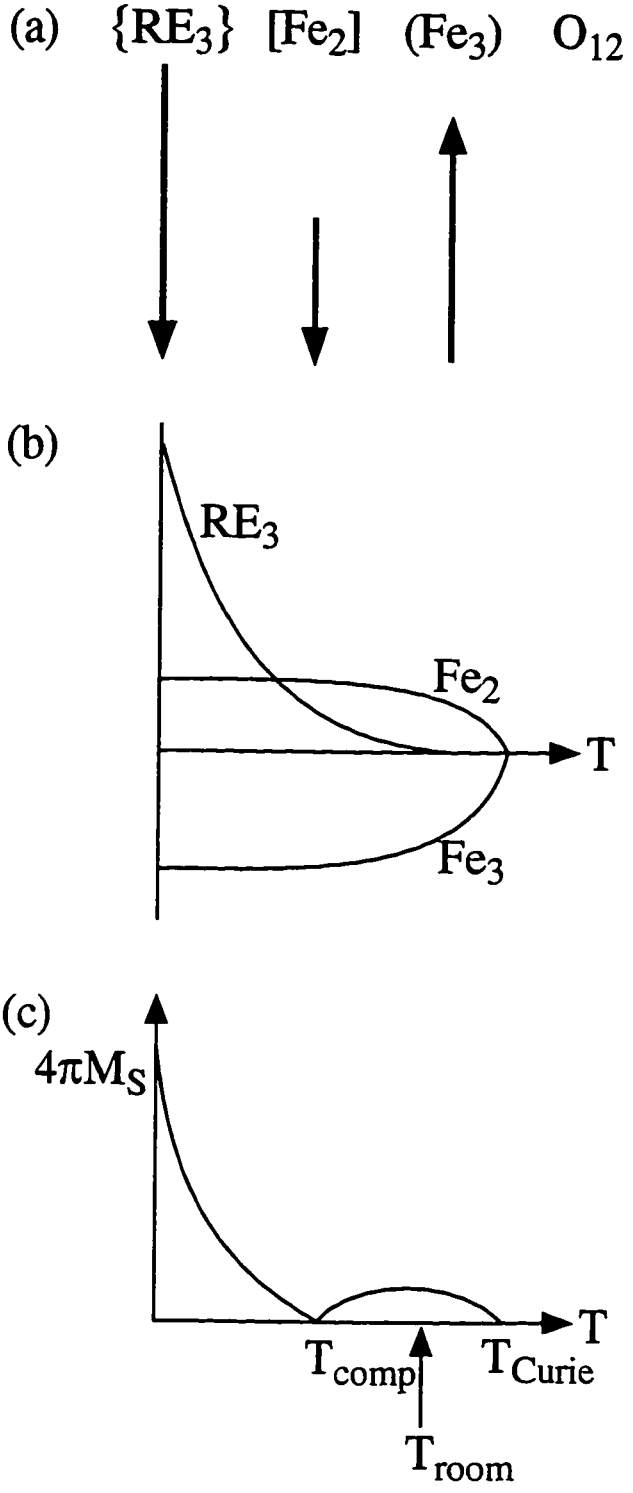

Fig. 2.1 (a) Relative orientations of the sublattice magnetizations. (b) Sublattice magnetizations vs temperature T. (c) Total magnetization $4\pi M_S$ vs temperature T.

2.2 Magnetic Interactions and Domain Walls

Magnetic bubbles are cylindrical magnetic domains of reversed magnetization in a thin uniaxial ferrimagnetic garnet film, as illustrated in Fig. 2.2. In this section we review the magnetic interactions within the garnet film from a micromagnetic approach and discuss the equilibrium configuration of domain walls.

Magnetic Interactions

The garnet film consists of a network of ions having "spin" and magnetic moments involved in four different interactions, each interaction resulting in an interaction energy:

1) Bias Field Energy Density, $E_B = -\bar{M}_S \cdot \bar{H}_B$, where $\bar{H}_B$ is an externally applied bias magnetic field. The energy density E_B results from the interaction between the magnetization and the bias field. In our experiments, $\bar{H}_B$ is a spatially uniform dc magnetic field perpendicular to the film plane.

2) Demagnetization Energy Density,

$$E_D = \frac{H_D{}^2}{8\pi} = -\frac{1}{2}\bar{M}_S \cdot \bar{H}_D,$$

where $\bar{H}_D = \bar{H} - \bar{H}_B$ is the demagnetization field, associated with magnetization. The demagnetization energy density E_D is related to the shape of the film. For bubbles to exist the magnetization must be perpendicular to the film plane. However for garnet films, where the lateral dimension of the film is much larger than the film thickness, $H_D = -4\pi M_S$ if the magnetization is perpendicular to the film plane and $H_D = 0$ if the magnetization is parallel to the film plane; thus E_D is $2\pi M_S{}^2$ higher in the perpendicular case than in the parallel case. Therefore the magnetization would tend to collapse into the film plane to minimize E_D. To prevent the collapse, the garnet film must possess a strong uniaxial

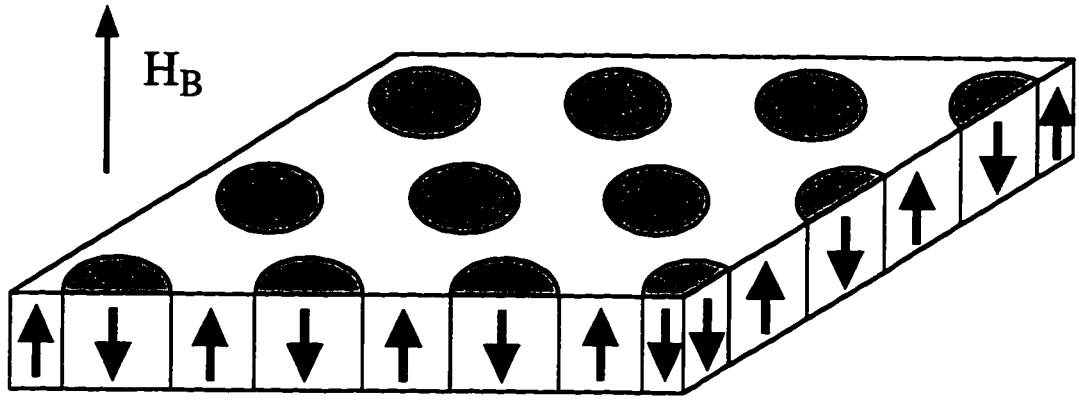

Fig. 2.2 Schematic illustration of magnetic bubbles in a thin garnet film.

anisotropy with its easy axis perpendicular to the plane. The energy density advantage for perpendicular vs in-plane orientation of the magnetization is labeled K_u. It follows that K_u must exceed $2\pi M_S^2$. The ratio $Q = K_u/2\pi M_S^2$ is called quality factor. It is necessary that $Q > 1$ for bubble materials.

The demagnetization energy is reduced by the formation of domains of reversed magnetization [Kittel, 1949]. In bubble films E_D approaches zero as the reverse domains equal half of the volume so that the net magnetization is zero and as the lateral dimensions of the domains become very small with respect to the film thickness.

3) Anisotropy Energy Density, $E_K = K_u \sin^2\theta$, where K_u is the uniaxial anisotropy parameter and θ is the angle between the magnetization and the normal to the film plane. The energy density E_K is related to the orientation of the magnetization with respect to some internal structure of the film. Two kinds of internal structure can contribute to the anisotropy energy, the overall crystal structure occurring in crystalline films and the variations in structure induced by the film growth process. The uniaxial anisotropy of our garnet sample is mostly growth induced. The cubic symmetry of the garnet gives zero uniaxial crystalline anisotropy. Anisotropy favors the orientation of the magnetization perpendicular to the film, either up or down.

4) Exchange Energy Density, $E_X = A[(\nabla\alpha_1)^2+(\nabla\alpha_2)^2+(\nabla\alpha_3)^2]$, where A is the exchange constant and α_1, α_2, α_3 are the direction cosines of the orientation of the local magnetization. If only this energy is involved, the local magnetization would favor constant orientation to minimize E_X. When the local magnetization has to change its orientation to form domains to minimize demagnetization energy, the exchange energy would prevent abrupt discontinuities in the orientation of local magnetization and prefer a smooth transition instead.

Domain Walls

A magnetic bubble is a domain of reversed magnetization in a garnet film. The magnetization rotates 180° within a region between neighboring bubble (down) and background (up) domains. This transition region is called the domain wall. The internal structure of domain walls is crucial in bubble transport. The existence of a finite width domain wall results from the competition of exchange and anisotropy energies. Figure 2.3 shows a schematic cross section of a domain wall. Within the domain wall, strong anisotropy prefers either up or down domains, while exchange coupling tends to keep the angle between adjacent spins small. The width of the domain wall, δ_w, can be determined by minimizing the sum of anisotropy and exchange energies

$$\int_{-\infty}^{+\infty}(E_K + E_X)dx \tag{2.2.1}$$

using variational method [Kittel, 1949; Eschenfelder, 1981]. The result is

$$\delta_w = \pi(A/K_u)^{1/2}. \tag{2.2.2}$$

The minimized integral of Eqn. (2.2.1) is defined as the energy density of the domain wall, σ_w. The result is

$$\sigma_w = 4(AK_u)^{1/2}. \tag{2.2.3}$$

Both the exchange constant A and the anisotropy parameter K_u tend to increase σ_w, but A tends to increase δ_w while K_u tends to decrease it. Domain walls can be observed with a pair of crossed polarizer and analyzer. Over the field of view the domains are of equal intensity and the domain walls appear dark.

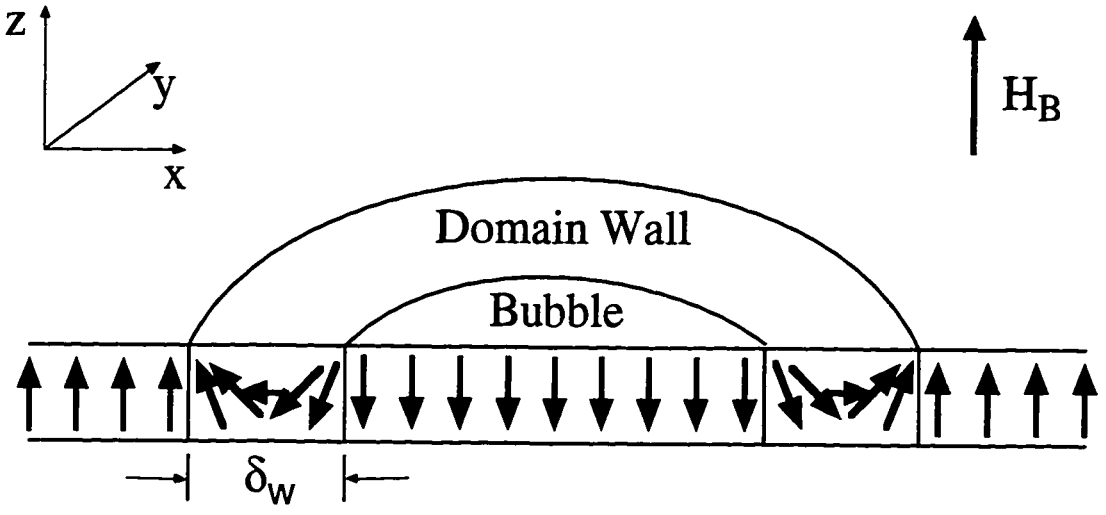

Fig. 2.3 Schematic cross section of a magnetic bubble showing structure of domain wall.

2.3 Magnetic Bubbles

Energetics of Magnetic Bubbles

The total energy of an isolated bubble relative to saturation can be written as

$$\xi_T = 2\pi rh\sigma_w - \xi_D + 2M_S H_B \pi r^2 h, \tag{2.3.1}$$

where r is the bubble radius and h is the film thickness [Bobeck, 1967]. The first term is the wall energy. The second term is the demagnetization energy. The exact expression for ξ_D has been derived by Thiele [1969; 1971]. Under most circumstances, it is sufficient to approximate ξ_D as $\xi_D \cong 2\pi {M_S}^2 V$, where V is the average volume over which reversed spins provide flux closure. Flux closure means that magnetic field lines form closed circuits. For very small r/h, V is a cylinder with a radius 2r, so $V \cong \pi(2r)^2 h$. For large r/h, V is a cylindrical shell with radius r and shell thickness $\cong$ 2h, so $V \cong 4\pi rh^2$. The third term is the bias field energy. It is the energy of a magnetic dipole with a dipole moment $\mu = 2M_S \pi r^2 h$ in the bias field H_B. The factor 2 occurs in this term because the bubble domain is equivalent to the superposition of a domain of magnetization $-2M_S$ and a uniformly magnetized plate. The energy between the magnetization in the bubble wall and the bias field is ignored.

An important dimension is the characteristic length

$$l \equiv \frac{\sigma_w}{4\pi {M_S}^2}, \tag{2.3.2}$$

at which the demagnetization energy balances the wall energy. The length l is a characteristic property of the garnet film and is independent of the domain configuration.

Figure 2.4(a) shows the total energy of an isolated bubble ξ_T as a function of bubble radius r obtained from Eqn. (2.3.1). As shown in the figure, an isolated bubble can only exist within certain range of external bias field. The upper limit is the bubble collapse field H_{CO}, a field above which all bubbles disappear. The lower limit is the strip-out field H_{SO}, a field below which isolated bubbles run out into stripes [Eschenfelder, 1981].

For an array of identical bubbles, the total energy is

$$\xi_{array} = N\xi_T + \frac{1}{2}\sum_{i=1}^{N}\sum_{j=1}^{N}\xi_{int}^{ij}, \qquad (2.3.3)$$

where N is the total number of bubbles in the array. The repulsive interaction between the ith and jth bubbles falls off like a magnetic dipole-dipole interaction as their separation $R_{ij} \to \infty$ [Cape and Lehman, 1971]:

$$\xi_{int}^{ij} \cong \frac{\mu_i \mu_j}{R_{ij}^3}, \qquad \text{with } \mu_i = 2M_S \pi r^2 h. \qquad (2.3.4)$$

A phase diagram for the garnet film in a bias field and at a temperature can be derived from Eqn. (2.3.3) using a Ginzburg-Landau approach [Garel and Doniach, 1982]. Figure 2.4(b) shows the bubble radius r vs the bias field H_B for an isolated bubble and a bubble array. Because the orientation of the magnetic field a bubble feels from the rest of the bubbles is opposite to its own magnetization, H_B must be reduced so that the bubbles can maintain the same size as that of an isolated bubble. Otherwise, at the same applied field bubbles have smaller radius than an isolated bubble. Bubble arrays can exist at zero bias field.

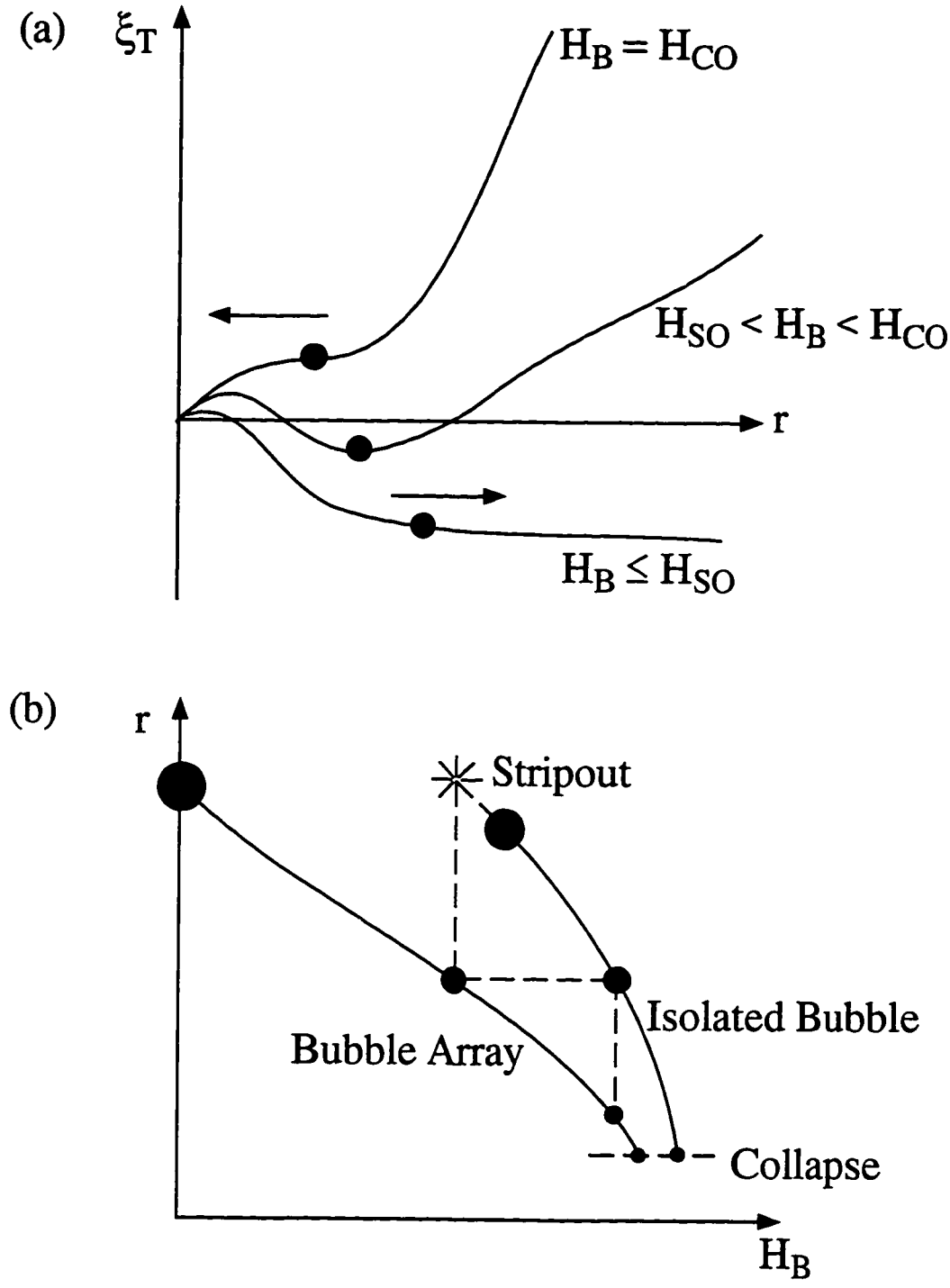

Fig. 2.4 Equilibrium configuration of magnetic bubbles. (a) Total energy of an isolated bubble ξ_T vs bubble radius r. (b) Comparison of bubble size between an isolated bubble and a bubble array vs bias field H_B.

Lamé Coefficients

Bubble arrays can be regarded as two-dimensional elastic media composed of discrete objects. Lamé coefficients λ and μ are important parameters describing the elastic properties of a system [Landau and Lifshitz, 1986]. A deformation can be decomposed into a pure shear with shear modulus μ and a hydrostatic compression with bulk modulus K. The coefficient λ is related to K and μ by $K = \lambda + \mu$. We have calculated the Lamé coefficients λ and μ of a bubble array from the energy density of an oblique bubble lattice. Assume the bubbles are perfect cylinders with radius r, lattice constant D, and thickness h. A shearing angle γ is introduced to allow calculation of the shear modulus. The magnetic energy density η of the oblique lattice, in terms of $4\pi M_S^2$, is [Höfelt, 1973]

$$\eta = \frac{2\pi l k}{\sqrt{3}ts} + \frac{\pi h_B k^2}{\sqrt{3}} + \frac{1}{2}\left[\left(\frac{\pi k^2}{\sqrt{3}} - 1\right)^2 - 1\right] + \frac{sk^2}{3\pi}\left[1 - \exp\left(-\frac{2\pi g_{mn}}{s}\right)\right]\frac{J_1{}^2(\pi k g_{mn})}{g_{mn}{}^3} \tag{2.3.5}$$

where

$$g = \tan\gamma \tag{2.3.6}$$

and

$$g_{mn} = \left[m^2 + (n/\sqrt{3} - gm)^2\right]^{1/2}. \tag{2.3.7}$$

The signs for summation over m and n are suppressed: if m and n appear more than once in a term, the summation is over all even (m+n) values with integer m and n from $-\infty$ to $+\infty$, except $m = n = 0$. For example,

$$g_{mn}^2 = \sum_{m,n} \left[m^2 + (n/\sqrt{3} - gm)^2 \right],$$

where the summation follows the above rule. The symbol J_1 is the first kind Bessel function, $h_B = H_B/4\pi M_S$ is the dimensionless bias field, and l is the characteristic length defined in Eqn. (2.3.2). Dimensionless variables $k = 2r/D$ and $s = D/h$ are used.

The elastic energy density is the difference between the magnetic energy density of the deformed lattice and that in equilibrium configuration. The equilibrium values of s and k can be obtained from

$$\frac{\partial \eta}{\partial s} = \frac{\partial \eta}{\partial k} = 0. \tag{2.3.8}$$

Lamé coefficients can be expressed as

$$\mu = \frac{\partial^2 \eta}{\partial g^2} \tag{2.3.9}$$

and

$$\lambda + \mu = \frac{1}{4} s^2 \left[\frac{\partial^2 \eta}{\partial s^2} - \frac{\left(\frac{\partial^2 \eta}{\partial s \partial k} \right)^2}{\frac{\partial^2 \eta}{\partial k^2}} \right]. \tag{2.3.10}$$

For our garnet film, h = 7.8 μm, l = 0.80 μm, and $4\pi M_S$ = 190 G, the result is $\lambda \cong 32.7$ erg/cm^2 and $\mu \cong 9.60$ erg/cm^2.

Bubble States

The magnetization is rotated 180° when passing through the bubble wall. In the center of the wall the magnetization lies in the plane of the film. A bubble state is represented by a state number S defined as

$$S = \oint \frac{d\phi}{2\pi}, \tag{2.3.11}$$

the net number of revolutions of the magnetization in the center of the wall when tracing around the bubble counterclockwise. The angle ϕ is the wall magnetization angle relative to a fixed direction in the film plane. Figures 2.5(a) and 2.5(b) are examples of two simple bubble states. The transition region of tight, in-plane rotation of magnetization is called a "Bloch line". There are no Bloch lines in Fig. 2.5(a) for S = 1 but two Bloch lines in Fig. 2.5(b) for S = 0. More complicated internal wall structures can exist because of the complexity of Bloch lines. We discuss the importance of bubble states in bubble transport driven by a magnetic field gradient in the next section.

2.4 Gradient Propagation of a Bubble

A magnetic field which is perpendicular to the film plane but has an in-plane field gradient exerts an in-plane force on magnetic bubbles. The direction of the force and the possible resulting bubble motion is determined by the bubble state. This gradient driven propagation mechanism is used in our collective transport experiment.

As shown in Fig. 2.6(a), the field $H_z(x)$ we consider is in the $\hat{z}$ direction but has a constant gradient in the $-\hat{x}$ direction. As discussed in Section 2.3, with the magnetization in the bubble wall ignored, the bubble is like a magnetic dipole with a dipole moment

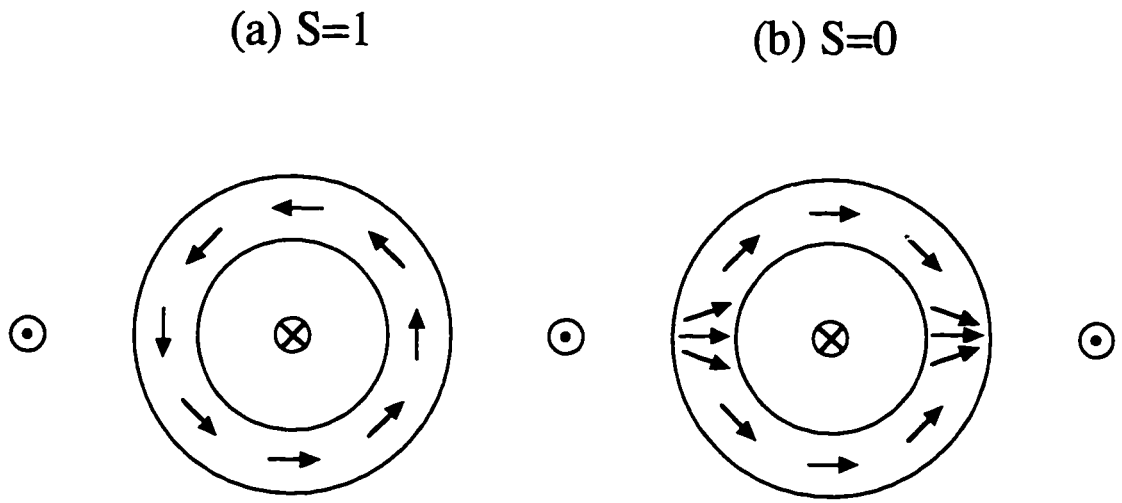

Fig. 2.5 Schematic illustration of the configuration of the local magnetization in the center of a bubble wall for (a) S = 1 and (b) S = 0 states, respectively.

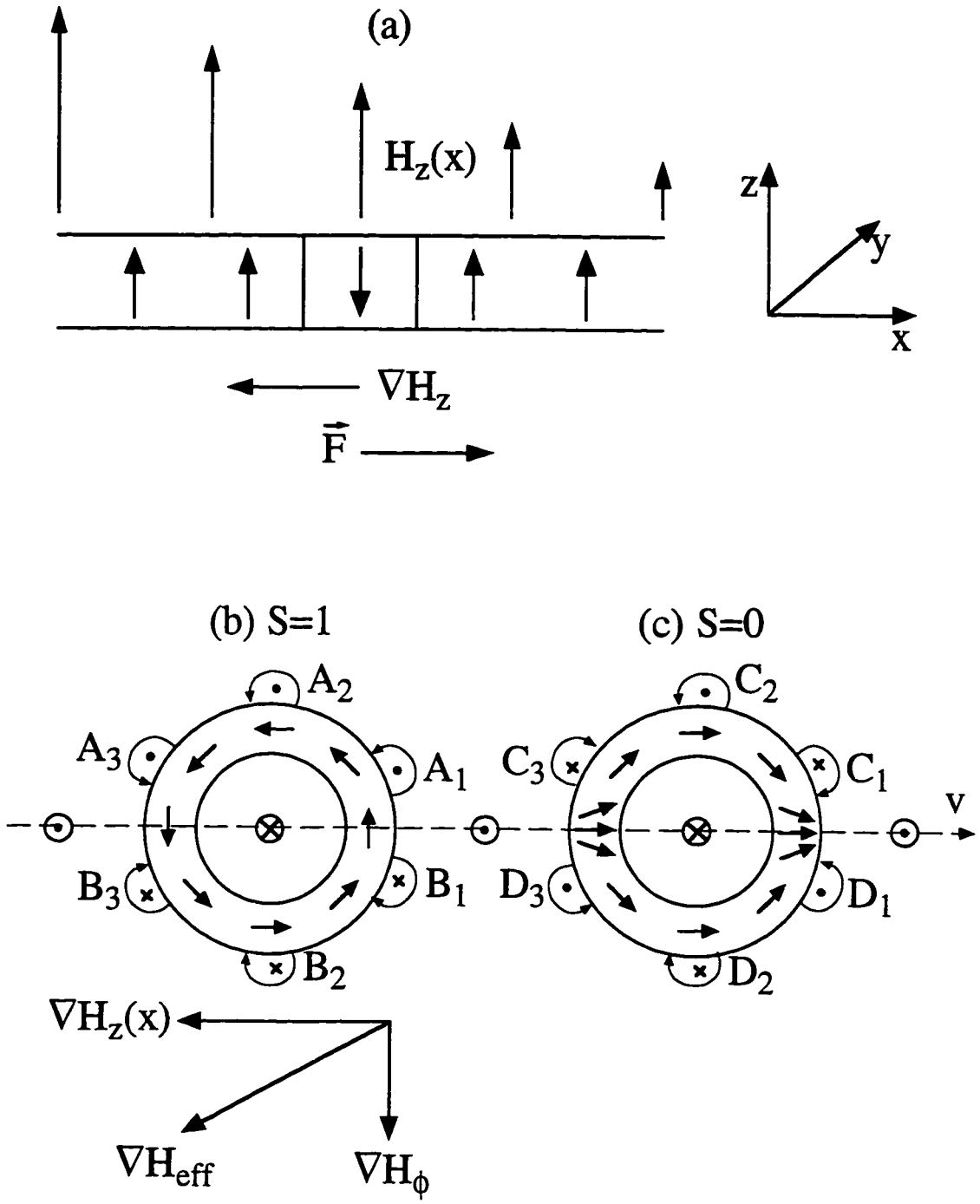

Fig. 2.6 (a) A bubble in a gradient magnetic field $H_z(x)$. (b) Motion of a bubble with S = 1 is deflected in a gradient field $H_z(x)$ due to an effective gradient field H_ϕ associated with spin precession. (c) Motion of a bubble with S = 0 is in the direction of the field gradient $\nabla H_z(x)$ due to the cancellation of H_ϕ.

$\mu = 2M_S\pi r^2 h$. The energy of such a bubble in a magnetic field is equal to the third term in Eqn. (2.3.1) with H_B replaced by $H_z(x)$, that is

$$\xi_B = \mu H_z(x). \tag{2.4.1}$$

The bubble feels a force

$$F = -\mu \frac{dH_z(x)}{dx}. \tag{2.4.2}$$

This force is along the $\hat{x}$ direction, so the bubble will move opposite to the direction of the field gradient. In our experiments we also apply a spatially uniform bias field perpendicular to the film plane to control the bubble concentration. This uniform field does not affect the bubble motion.

However, the internal domain wall structure cannot be ignored in gradient driven bubble motion. A bubble with $S \neq 0$ deflects from the direction of the applied field gradient, while a bubble with $S = 0$ does not deflect. The deflection arises from the nonnegligible spin precession on the flanks of a bubble during bubble motion. Figures 2.6(b) and 2.6(c) illustrate bubbles with $S = 1$ and $S = 0$ in a gradient field to explain how bubble state affects the direction of bubble motion. Bubble motion is simply the motion of spins and magnetic moments. As the bubble moves along the $\hat{x}$ direction, the local spins across which the bubble wall moves will precess in the film plane as indicated. The direction of spin precession can be determined by the change of spin direction at the center of domain wall. An effective magnetic field perpendicular to the film plane must exist in order to produce the precession. For example, in Fig. 2.6(b) the spin precession at point A_1 fixed in the medium is counterclockwise and the spin precession at point B_1 also fixed in the medium is clockwise. The fields at A_1 and B_1 must differ in sign

because the spins precess in opposite directions at these two points. As a result, a field gradient ∇H_ϕ perpendicular to $\nabla H_z(x)$ must exist locally. For S = 1 bubbles, ∇H_ϕ at other places such as along A_2B_2 or A_3B_3 is in the same direction, therefore a bubble with S = 1 deflects from $\nabla H_z(x)$ direction. For S = 0 bubbles in Fig. 2.6(c), although there is spin precession and a field gradient ∇H_ϕ locally, ∇H_ϕ is not in the same direction at different locations and its overall effect is canceled out. Therefore a bubble with S = 0 has zero net ∇H_ϕ and does not deflect.

For bubbles with a small number of Bloch lines, the deflection angle ψ is given by [Malozemoff and Slonczewski, 1979]

$$\tan\psi = \frac{2S\delta_s}{\pi\alpha r}, \tag{2.4.3}$$

where α is the dimensionless Gilbert damping parameter, which measures the strength of the viscous damping the magnetization feels. The term $\tan\psi$ is proportional to S for any number of Bloch lines and does not depend on structural details of bubble walls.

2.5 Substrate Roughness and ac Magnetic Field

The garnet films used for this work were grown on nonmagnetic substrates using liquid phase epitaxy (LPE). The flatness of the substrate is examined using optical and x-ray scattering. The substrate is lapped and polished to ensure that it is smooth and has very few defects before depositing the bubble film. The properties of the substrate for our garnet samples are quite uniform over the wafer on length scale greater than bubble size. This can be tested from observation of how a dilute bubble array diffuses in an ac field as described below. In a garnet film with uniform substrate, the local bubble concentration is uniform over the film. The bubbles diffuse in random directions and there are no correlated

bubble displacements. While in a garnet film with less uniform substrate, the local bubble concentration is non-uniform. Bubble diffusion is not purely random and in some regions bubbles are collectively pinned in a line and they barely diffuse.

Although it is smooth on length scale greater than bubble size, the substrate is microscopically rough due to random alloy fluctuations and film thickness variations on length scale smaller than bubble size. The substrate roughness produces a weak random potential on length scales much shorter than the bubble size, which can be considered as weak random point disorder [Hu and Westervelt, 1995]. The length scale of the point-like pinning potential is ~ 0.4 μm [Seshadri and Westervelt, 1992b].

A small perpendicular sinusoidal magnetic field with frequencies of 10 to 60 Hz causes oscillation of the bubble diameters without changing the bubble concentration [Woolhouse and Chaudhari, 1974]. Seshadri and Westervelt [1992b] proposed that the ac field simulates Brownian motion due to the presence of substrate roughness, and has the effect of thermal fluctuations.

We measured the motion of isolated bubbles at a bubble concentration of 60 mm^{-2} and an ac field of 7.6 Oe peak-to-peak amplitude at 40 Hz. This bubble concentration was achieved by first raising the dc bias field to 100 Oe and then letting the bubbles freely diffuse in zero gradient field for 8 hours. During this process, we recorded bubble diffusion for 6 minutes every 2 hours. Figure 2.7 shows the measured mean-square bubble displacement $\langle(\vec{r} - \vec{r}_0)^2\rangle$ vs diffusion time t after successive 2-hour intervals. As shown, the bubble diffusion at t = 0 is faster than at later times, presumably because the bubbles were just brought to this concentration and the array was not in equilibrium state. The bubble diffusion at t = 2 hrs and later times are similar, suggesting the system reaches equilibrium after 2 hours. Other than some random fluctuations, the diffusion curves at t = 2 hrs and later times follows

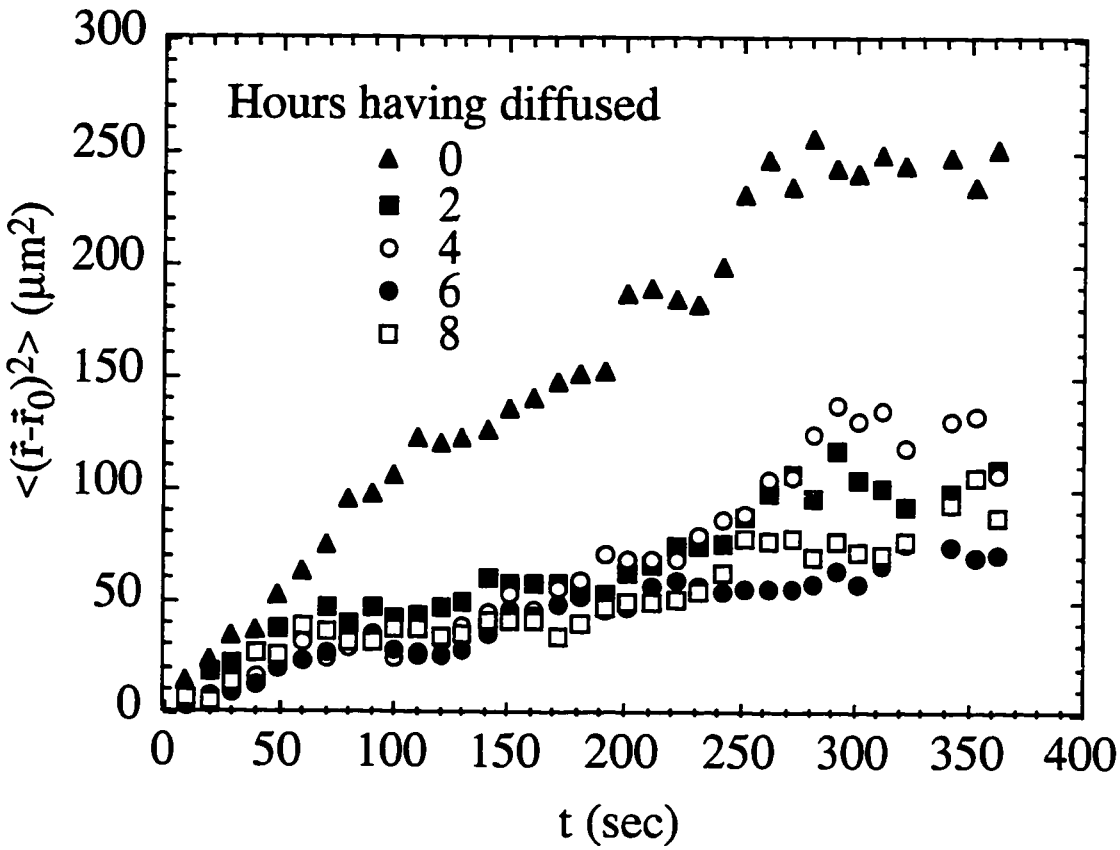

Fig. 2.7 Measured mean-square bubble displacement $<(\vec{r}-\vec{r}_0)^2>$ vs diffusion time t for five diffusion periods. The bubble concentration is 60 mm^{-2} and the ac field is at 40 Hz and 7.6 Oe peak-to-peak amplitude.

$$\left\langle (\bar{r} - \bar{r}_0)^2 \right\rangle = Dt, \tag{2.5.1}$$

indicating that the bubbles undergo Brownian-like motion. Our analyses also showed that the measured velocity distribution during bubble diffusion satisfies

$$\left| \frac{N_+ - N_-}{N} \right| \leq \frac{1}{\sqrt{N}}, \tag{2.5.2}$$

where $N = N_+ + N_-$ is the total number of bubbles and N_+ (N_-) is the number of bubbles with $v > 0$ ($v < 0$). Isolated bubble diffusion characteristics shows that the ac field does simulate thermal fluctuations.

The effective temperature of isolated bubbles can be determined using the Einstein relation [Seshadri and Westervelt, 1992b] because they diffuse freely in the ac field and the drift velocity is proportional to the applied force. However in a bubble array bubble diffusion is restricted. We use the standard deviation σ of the bubble displacement over a fixed amount of time in the absence of applied force to characterize the effective thermal fluctuations of a bubble array produced by H_{ac}. The ratio σ/a, where a is the bubble spacing, can be compared with Lindemann criterion to determine whether the system melts or not. According to Lindemann criterion, a lattice will melt when the amplitude of vibration of the objects in the lattice is 0.1 of the lattice constant, i.e., $\sigma/a = 0.1$.

2.6 Pinning by Permalloy Overlayer

The ability to introduce artificial pinning into the magnetic bubble array enables us to study the effect of pinning with a wide variety of geometries and strengths on a two-dimensional system. There are two ways to introduce artificial pinning into the bubble system [Seshadri, 1992a]. The first way is to etch the garnet film. Etching results in a

thickness modulated garnet film, and the pinning comes from the difference in the bubble height and therefore its dipole moment. Etching causes permanent damage to the garnet film. In our experiments, we use another method, that is to deposit a permalloy layer of certain pattern on top of the garnet film, as shown in Fig. 2.8.

Permalloy is a soft magnetic material with very high permeability. A permalloy overlayer pins magnetic bubbles underneath by providing flux closure between bubbles and neighboring domains with opposite magnetization: if a bubble is located under one end of a permalloy layer initially (Fig. 2.8(a)), it tends to move toward the center of the permalloy layer to achieve maximum flux closure to minimize its magnetic energy (Fig. 2.8(b)). The magnetization on the left of the permalloy layer flips from Figs. 2.8(a) to 2.8(b) because otherwise the total magnetic energy of the system would be higher. The pinning strength can be controlled by the thickness and in-plane dimension of the permalloy layer. We chose this pinning method rather than etching because permalloy layers are removable and do not cause permanent damage to the film.

A permalloy film thickness of 30 Å to 6000 Å can achieve effective pinning. The lower limit is required for spontaneous magnetization [Chikazumi, 1964]. The upper limit is required so that the magnetization lies in the in-plane direction [Kittel, 1946; Seshadri, 1992a]. The deposition of permalloy layer changes the bubble size only slightly; we can ignore this effect in our experiments.

2.7 Characteristics of Garnet Sample

Large lattice constant (LLC) garnets are used in our experiments. LLC garnet is a bismuth-substituted iron garnet, grown at the Airtron Division of Litton Industries [Belt and Ings, 1987]. The bubble films were grown on both surfaces of the substrate; the side with a higher collapse field H_{CO} is used in our experiments. Table 2.1 lists typical

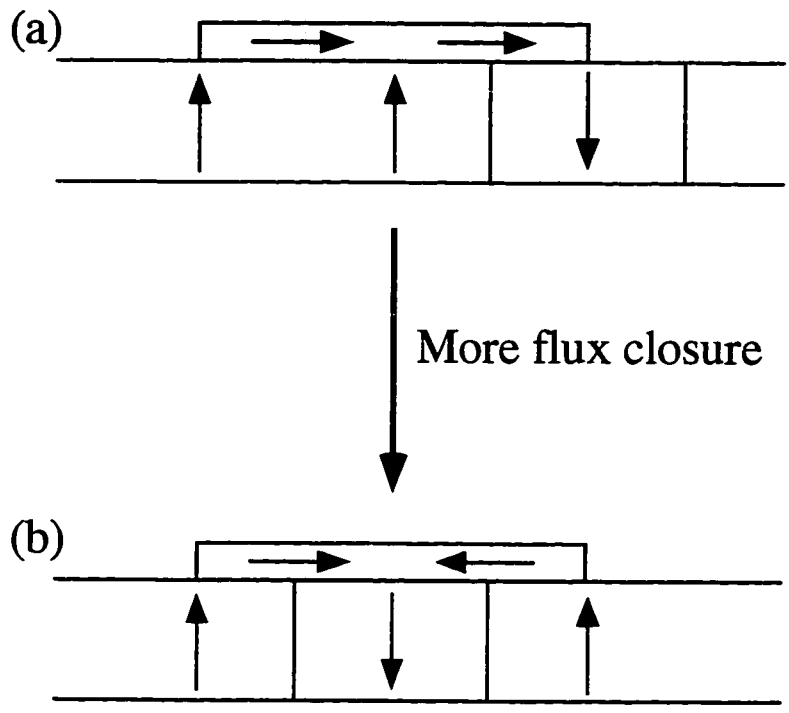

Fig. 2.8 Schematic illustration of pinning of a bubble by permalloy overlayer. The bottom layer with vertical arrows is the garnet film; the top hatched layer is the permalloy layer. (a) An unhappy bubble, partially pinned by the permalloy overlayer. (b) A happy bubble pinned by the permalloy overlayer.

Table 2.1 Characteristics of the LLC Garnet Sample

Structural Parameters	
Film Composition	$(Bi_{1.09}Tm_{0.07}Gd_{0.95}Y_{0.90})(Fe_{3.91}Ga_{0.76}Y_{0.30}Tm_{0.02})O_{12}$
Lattice Constant of Film	12.493 Å
Substrate Composition	$(Gd_{2.68}Ca_{0.32})(Ga_{3.02}Mg_{0.33}Zr_{0.65})O_{12}$
Lattice Constant of Substrate	12.495 Å
Film Thickness	$h = 7.8 \pm 0.2$ μm
Defect Density	0 - 5 defects/cm^2
Magneto-optical Parameters	
Faraday Rotation	1.4°/μm at 632 nm
	3.5°/μm at 546 nm
Figure of Merit	4°/dB
Magnetic Parameters	
Bulk Magnetization	$4\pi M_S = 190$ G
Curie Temperature	$T_{Curie} = 170$°C
Exchange Constant	$A = 2.1 \times 10^{-7}$ erg/cm
Anisotropy Parameter	$K_u = 1.6 \times 10^4$ erg/cm^3
Quality Factor	$Q = 11.1$
Wall Energy Density	$\sigma_w = 0.23$ erg/cm^2
Wall Thickness	$\delta_w = 0.11$ μm
Characteristic Length	$l = \sigma_w / 4\pi M_S^2 = 0.80$ μm
Anisotropy Field	$H_\mu = 2K_\mu / M_S = 2.1$ KOe
Collapse Field	$H_{CO} = 103$ Oe
Bubble Collapse Radius	$r_{CO} = 2.0$ μm
Coercive Field	$H_c = 0.2$ - 0.4 Oe
Stripe Run-In Field	$H_{RI} = 83.5$ Oe

parameters of the LLC garnets, obtained from a LLC garnet sample. Parameters for other LLC garnet samples are close to those listed in Table 2.1.

For LLC garnets, substitution of part of the Y^{3+} ions by the diamagnetic ion Bi^{3+} improves the figure of merit (defined as the ratio of Faraday rotation angle to optical absorption), making it an ideal bubble material for optical observation [Geller *et al.*, 1963; Buhrer, 1969; Belt and Ings, 1987]. The lattice spacing of the nonmagnetic substrate is matched to that of the film to reduce the stress in the bubble film.

Coercive field H_c is a material parameter below which domain wall motion is impossible. It arises from the interaction of the domain wall with defects or inhomogeneities, and is analogous to dynamic friction in classical mechanics [Malozemoff and Slonczewski, 1979]. It is also a measure of substrate pinning strength. Our garnet sample has a low defect density, therefore H_c is comparable for that of device quality garnets: $H_c = 0.2 - 0.4$ Oe.

In our experiments, the bubble diameter ranges from about 12 μm at zero bias field to 4 μm before they collapse at $H_{CO} = 103$ Oe. This bubble size is suitable for direct microscopic observation. Seshadri [1992a] measured the evolution of the triangular bubble array as a function of bias field and showed that, for 85 Oe < H_B < 95 Oe, the bubble radius remains constant, that is, $r = 3.26 \pm 0.13$ μm. Raising the bias field H_B reduces the bubble concentration ρ. We use this property to study the physics as a function of bubble concentration while keeping the bubble dipole moment fairly constant.

To summarize, the magnetic bubble system is a good model system to study two-dimensional statistical physics. The key characteristics of the bubble system can be summarized as follows: the magnetic bubbles interact with each other via a repulsive magnetic dipole-dipole potential; the nonmagnetic substrate has a microscopic roughness that acts like a random point disorder with pinning length scale ~ 0.4 μm [Seshadri and Westervelt, 1992b]; the ac agitation coupled with substrate roughness makes bubbles undergo Brownian motion and effectively simulates thermal fluctuations.

CHAPTER 3 EXPERIMENTAL METHODS

In this chapter we describe the techniques and apparatus used in our magnetic bubble experiments. In Section 3.1 we describe how to nucleate magnetic bubbles by brief application of a strong in-plane magnetic field on the garnet film. We also describe how to anneal the bubbles with an ac field to form a triangular bubble array. In Section 3.2 we describe how to observe and record the motion of magnetic bubbles in real time using polarization microscopy and computer-video techniques. In Section 3.3 we describe how to control the bubble concentration, simulate temperature, and apply external forces on bubbles with magnetic fields. In Section 3.4 we describe how to produce pinning patterns using photolithography and electron beam evaporation techniques. Finally, in Section 3.5 we describe custom developed image processing and data analysis codes.

3.1 Nucleation and Annealing of Magnetic Bubbles

Several domain structures can exist in a garnet sample at zero magnetic field and room temperature: bubbles, stripes, and mixture of bubbles and stripes. Figure 1.1 shows some possible domain structures. The occurrence of a particular domain structure depends on the thermomagnetic history of the sample. The evolution of the topology of the domains as a function of magnetic field and temperature is irreversible [Molho, *et al.*, 1987].

Preparation of the bubble domains involves temporary disruption of the ferrimagnetic domain structure of the bubble material with a magnetic field or temperature, followed by removal of the magnetic field or temperature. Magnetic bubbles can be nucleated by applying a strong in-plane magnetic field H_{ip} along a preferred direction in the garnet sample, then reducing the magnetic field to zero within a few seconds [Woolhouse and

Chaudhari, 1974]. It is essential that H_{ip} be greater than the anisotropy field of the garnet sample $H_\mu = 2K_\mu/M_S$, in order to rotate the magnetization of the garnet sample 90° from its uniaxial axis and destroy the domain structure. Away from the preferred direction, stripes or mixtures of bubbles and stripes are formed. The preferred direction is determined experimentally by repeating the nucleation process at different orientations until perfect bubble domains are obtained. In our experiments this nucleation method is used. The in-plane magnetic field H_{ip} (> 2.1 kOe) is supplied by a commercial magnet Model HV-4H from Walker Scientific. Because the cooling system of the magnet is not installed, it is advised that the application time be less than 1 minute to avoid overheating. The bubbles nucleated using this method are all in S = 0 state.

Magnetic bubbles can also be nucleated using a field cooling method [Molho, *et al.*, 1987]. This technique involves first heating the garnet sample to above the Curie temperature T_{Curie} = 170°C so that the garnet becomes paramagnetic instead of ferrimagnetic. The sample is then cooled down to room temperature in a small constant perpendicular magnetic field of a few oersted. Finally, the field is suppressed. In the absence of any perpendicular magnetic field, stripes would form, and at larger magnetic fields mixtures of bubbles and stripes would form.

The bubble arrays thus prepared have a disordered structure, as shown in Fig. 3.1(a), and the bubbles have different sizes. However, a nice triangular bubble array containing 1,000 to over 10,000 uniform bubbles can be obtained by annealing the garnet sample in an ac magnetic field perpendicular to the film plane for an extended period of time. This ac magnetic field produces an effective thermal agitation that allows the strain in the bubble system to relax. The annealing process improves the homogeneity of bubble size and the order of the bubble arrays by the collapse of smaller bubbles and the rearrangement and annihilation of dislocations. An ac field with peak-to-peak amplitude H_{ac} = 20.7 Oe and frequency 40 Hz is used to anneal our garnet samples. Typical annealing time is a few hours to 2 days. Figures 3.1(a) to 3.1(c) show the initial,

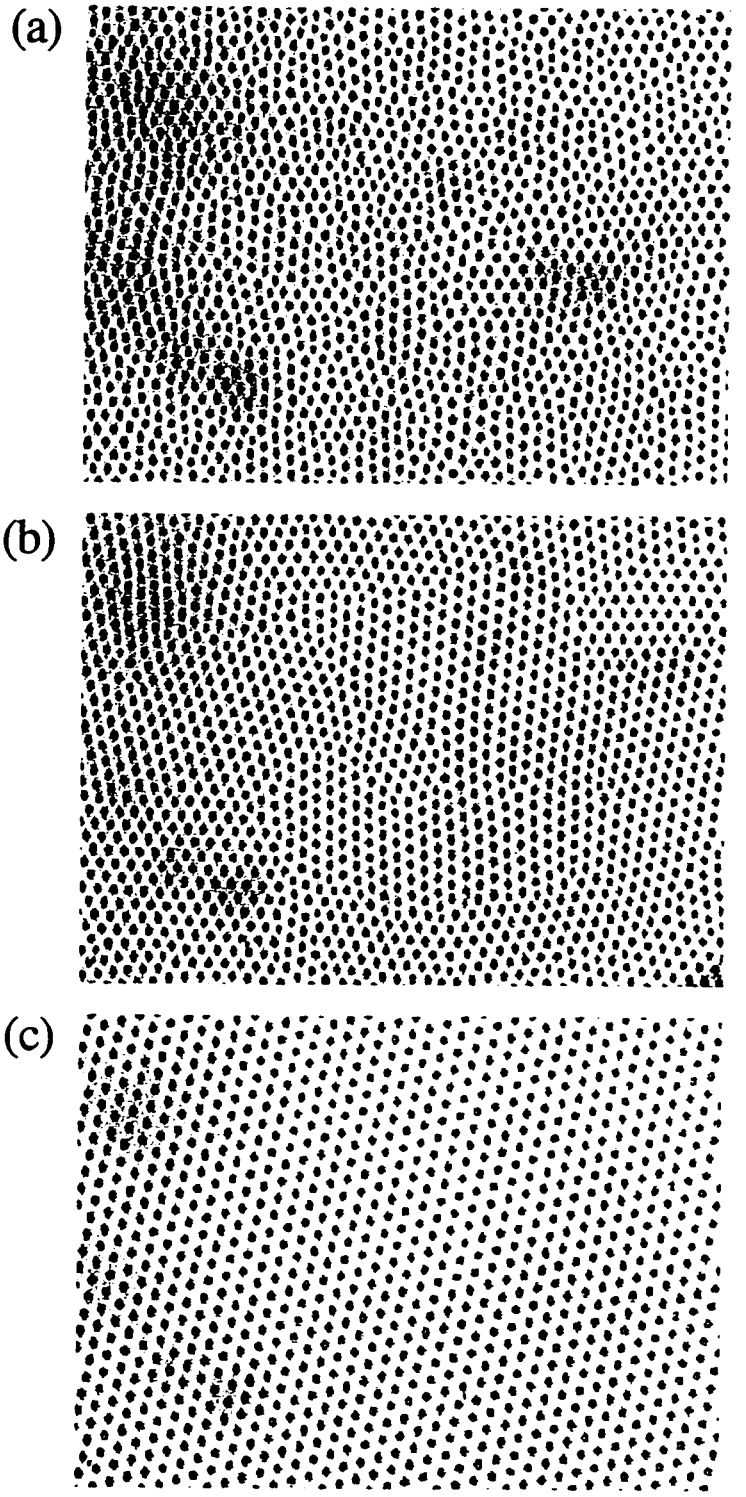

Fig. 3.1 Images of bubble array showing effect of annealing. (a) Before annealing, amorphous. (b) Immediately after applying the annealing field, polycrystalline. (c) 1.5 hours after applying the annealing field, singlecrystalline. All images are taken at a bias field $H_B = 46.8$ Oe. The image size is 537 x 394 μm^2.

intermediate, and final structures of the bubble domains during annealing. Before applying the annealing field, the bubbles are in an amorphous phase with no hexagonal order (Fig. 3.1(a)), and the bubble sizes vary at different locations. Upon application of the annealing field the bubbles form a polycrystalline array (Fig. 3.1(b)). Local bubble grains with hexagonal order of a few bubble spacings are separated by grain boundaries. The bubbles also become more uniform in size. Continuing application of the annealing field makes certain grains extend over a larger area. For a garnet sample with low defect density and low coercive field, a single crystal bubble array can cover the field of view after a few hours of annealing (Fig. 3.1(c)).

3.2 Observation of Magnetic Bubbles

One advantage of using the magnetic bubble system as a model system to study the statistical physics of two-dimensional systems is that the bubble system is directly observable by means of the Faraday effect. The Faraday effect refers to the rotation of a linearly polarized light when the light goes through a material in the presence of a magnetic field oriented in the light propagation direction [Hecht, 1987; Schwartz, 1972]. The Faraday rotation angle is proportional to the magnetic induction and to the traveling length of light in the medium. For ferrimagnetic materials, such as garnet films, the effective magnetic induction is the component of the magnetization in the propagation direction.

Figure 3.2 illustrates how the Faraday effect is used in our experiments. Unpolarized light is first converted to linearly polarized light by a polarizer. The polarized light then enters the garnet sample. Since the magnetization of the bubble domain points down and the magnetization of the background points up, the polarization of the light passing through these up and down domains rotates to opposite directions due to the Faraday effect. By orienting the polarization of the analyzer along the polarization of the light passing through the background, the light passing through the bubble domains is attenuated and as a result,

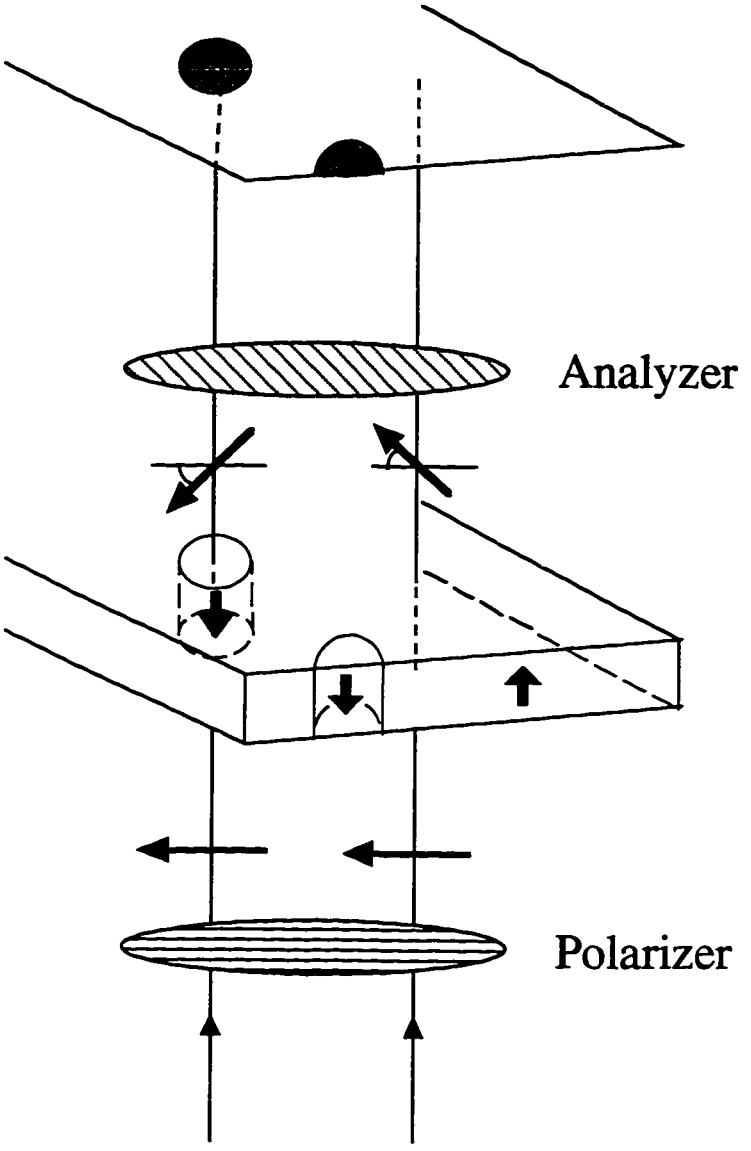

Fig. 3.2 Visualization of magnetic bubbles using the Faraday effect of rotating light.

the bubble domains appear as dark disks in a bright background. The polarization of the analyzer is adjustable in the setup so we rotate the polarization orientation of the analyzer to achieve maximum contrast between the bubbles and the background. The large amount of bismuth in our LLC garnet contributes to large Faraday rotation [Belt and Ings, 1987] and makes the bubbles readily distinguishable. For garnet of thickness 7.8 μm, the Faraday rotation angle is 10° - 30° over the wavelength range of the incoming light.

Magnetic bubbles are viewed in transmitting mode (Fig. 3.3). The white light comes from an incandescent lamp controlled by an Olympus TF transformer. The condensing lens, an inverted 10x objective, provides uniform illumination over a circular area of diameter 2 mm of the sample. Light is linearly polarized using a dichroic sheet polarizer before entering the sample. The sample is placed on a transparent Lucite sample holder that is fixed on an aluminum frame. The frame is mounted onto an NRC translational stage allowing fine position adjustment in x, y, z directions. An Olympus BHMJ optical microscope magnifies the domains in the sample, and an analyzer oriented along the polarization of the light coming out of the background creates contrast between the bubble domains and the background for direct visualization and image recording. We can view the bubble system either directly from the eyepiece or on the monitor through a CCD (Charge Coupled Device) video camera. Available magnifications are 25x to 800x at the eyepiece and 0.66 to 28.6 μm/pixel for video image. Using white light rather than monochromatic light can optimize the contrast between the bubble domain and the background by adjusting the orientation of the analyzer. White incoming light also makes the image colored. We have observed the change of color when rotating the analyzer. Both the sample stage and the optical setup are mounted on a 4'x 8' optical table. During data-taking, the optical table is floated with nitrogen gas so as to isolate it from vibration of the environment.

The digital-imaging setup (Fig. 3.3) allows us to capture, record, and analyze bubble array images. A VSP model SC505 high resolution CCD camera picks up monochrome images and converts them to video. We use NTSC (National Television Systems

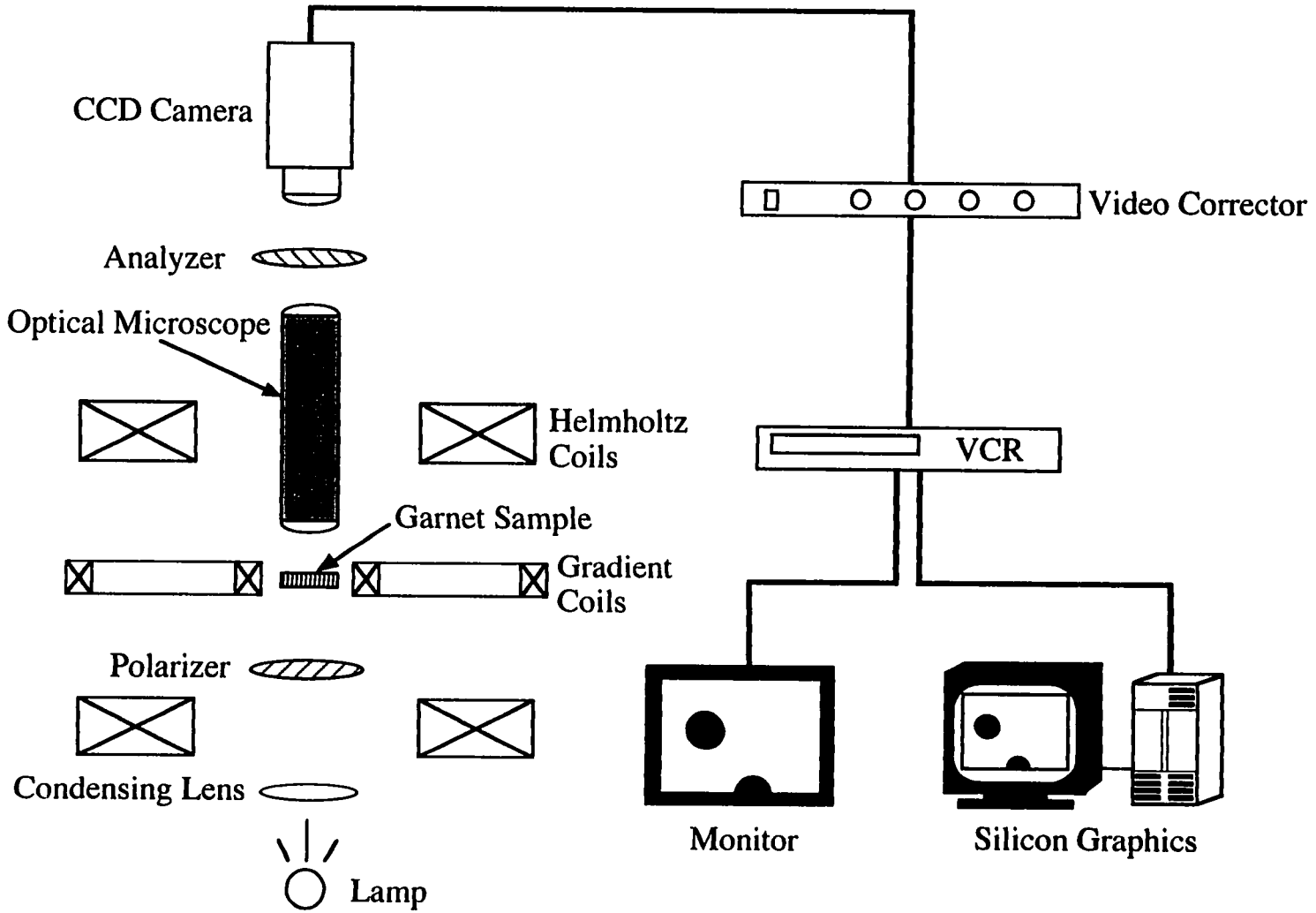

Fig. 3.3 Schematic diagram of the apparatus showing the optical, magnetic and computer-video setups.

Committee) standard output. It features a standard video image of size 640 x 480 pixels^2 and a frame rate of 30 frames/sec. The video signal goes through a Laird model VC-2000 video corrector that enhances the contrast and the sharpness of an image and reduces the noise. A Sony model SLV-R1000 SVHS video cassette recorder (VCR) is used to record images on Maxell SVHS tapes. A Sony Trinitron color monitor model SSM-2010 is used to monitor the images. The VCR is then interfaced to a Silicon Graphics workstation model IRIS Indigo Entry Graphics R4000 with an IndigoVideo real time video card. With the Indigo video card we can display the video images from the VCR or the CCD camera on the Silicon Graphics workstation in real time. We can also capture and convert a sequence of video images into digitized images. In Section 3.5 we will describe digital image processing and data analysis techniques.

We have carefully checked the geometric distortions of our optical and computer-video setups. Geometric distortions arise from an increase (for pincushion distortion) or a decrease (for barrel distortion) in the magnification of a lens toward the edge of the field. They can cause systematic errors in determining the locations of bubble centers on an image, while other aberrations only cause image blur and do not change the positions of bubble centers on the image. Geometric distortions directly affect the structure function and correlation function measurements. We first imaged an Olympus eyepiece micrometer which consists of 100 x 100 squares with each square being 100 μm x 100 μm. We then compared the area of each square along horizontal and vertical directions respectively to determine the distortions. Our measurements show that the geometric distortions associated with the optical setup are less than 1% in both directions, and the distortions associated with both the optical and computer-video setups are less than 1 pixel in both directions. Our imaging setup has such low distortions because we use Olympus MS-Plan and MD-Plan objectives which provide super flat field of view.

3.3 Control of Magnetic Bubbles

Our experiments are conducted at room temperature. Our sample is located at the center of a pair of Helmholtz coils which is 14 cm apart, as shown in Fig. 3.3. These coils produce a dc magnetic field perpendicular to the film plane at the sample location. The bubble concentration is controlled by this field. The coils are made of Cu tape, with a total resistance R = 1.5 Ω, inductance L = 51 mH and time constant L/R = 34 ms [Babcock, 1989b]. They are driven by a Kepco model BOP 20 - 20M bipolar operational power supply/amplifier in voltage mode. The magnitude of the field H_B at the sample location is determined by the current I_B with a Fluke 45 dual display multimeter (0 - 10 A) [Babcock, 1989b]:

$$H_B \text{ (Oe)} = (18.74 \pm 0.2)\ I_B \text{ (amp)}. \qquad (3.3.1)$$

The field H_B is uniform to better than within 1% over a circular area of about 3 mm in diameter. The current I_B should not exceed 6 amp if the current needs to be applied for longer than a few minutes. A higher current might generate enough heat to damage the insulating layer of the Cu tape.

A small ac magnetic field is used to agitate the bubble system and simulate thermal fluctuations. This ac field is generated by feeding the output of a Wavetek model 132 VCG/noise generator into the voltage programming input of the Kepco power supply mentioned above. As a result, an ac component I_{ac} is superimposed onto the dc current I_B. The currents I_{ac} and I_B are monitored simultaneously using the same Fluke 45 multimeter in ac and dc current modes. The ac field used in our experiment is 40 Hz and the peak-to-peak amplitude is [Seshadri, 1992a]

$$H_{ac} \text{ (Oe)} = 35.24\ I_{ac} \text{ (amp)} - 0.45. \qquad (3.3.2)$$

The Helmholtz coils have a corner frequency of 25 Hz below which eddy current is serious [Seshadri, 1992a].

In the collective transport experiment which we will discuss in Chapter 4 we drive the bubble array with a uniform in-plane force. This in-plane force is supplied by a pair of custom made gradient coils (Fig. 3.4(a)). Each coil consists of 100 turns of 16 awg high temperature magnet wire with heavy insulation. The resistance of the two coils in series is $R = 1.12\ \Omega$ and the inductance is $L = 4.89$ mH. As shown in Fig. 3.4(a), the garnet film is located in the middle of the two coils. For two parallel wires having equal currents flowing in the same direction, the magnetic field at a point on the plane containing the two wires is approximately linear in the distance from the center line between the two wires. Both its constant and quadratic terms vanish. This arrangement produces a perpendicular magnetic field with a uniform in-plane field gradient at the center region. The spacing between the two coils is adjustable within 0 to 2.5 inches. In our collective transport experiment the spacing was set to 0.866 inch. The coils are driven by a Kepco model BOP 20 - 20M power supply in voltage mode, with the current I_G monitored with a Fluke 75 multimeter.

We determine the magnetic field gradient using the bubble collapse field H_{CO} because for a garnet sample H_{CO} is well defined: the bubbles all disappear once the total magnetic field goes above H_{CO}. Figure 3.4(b) illustrates our scheme. We place a garnet sample with a disordered sea of bubbles at the sample holder between the two coils. We fix the gradient current I_G at 4 amps in the absence of any ac field. As H_B increases, the total magnetic field on the right side of the sample will first surpass H_{CO}, while the total field on the left will still be below H_{CO}. As a result, there will be an interface perpendicular to the field gradient and there are no bubbles to the right of the interface. We first overlap the interface with a fixed line in the microscope. An increase of H_B makes the interface move to the left. We then move the aluminum frame to which the sample and the gradient coils are mounted so that the interface overlaps with the fixed line again. By increasing H_B in

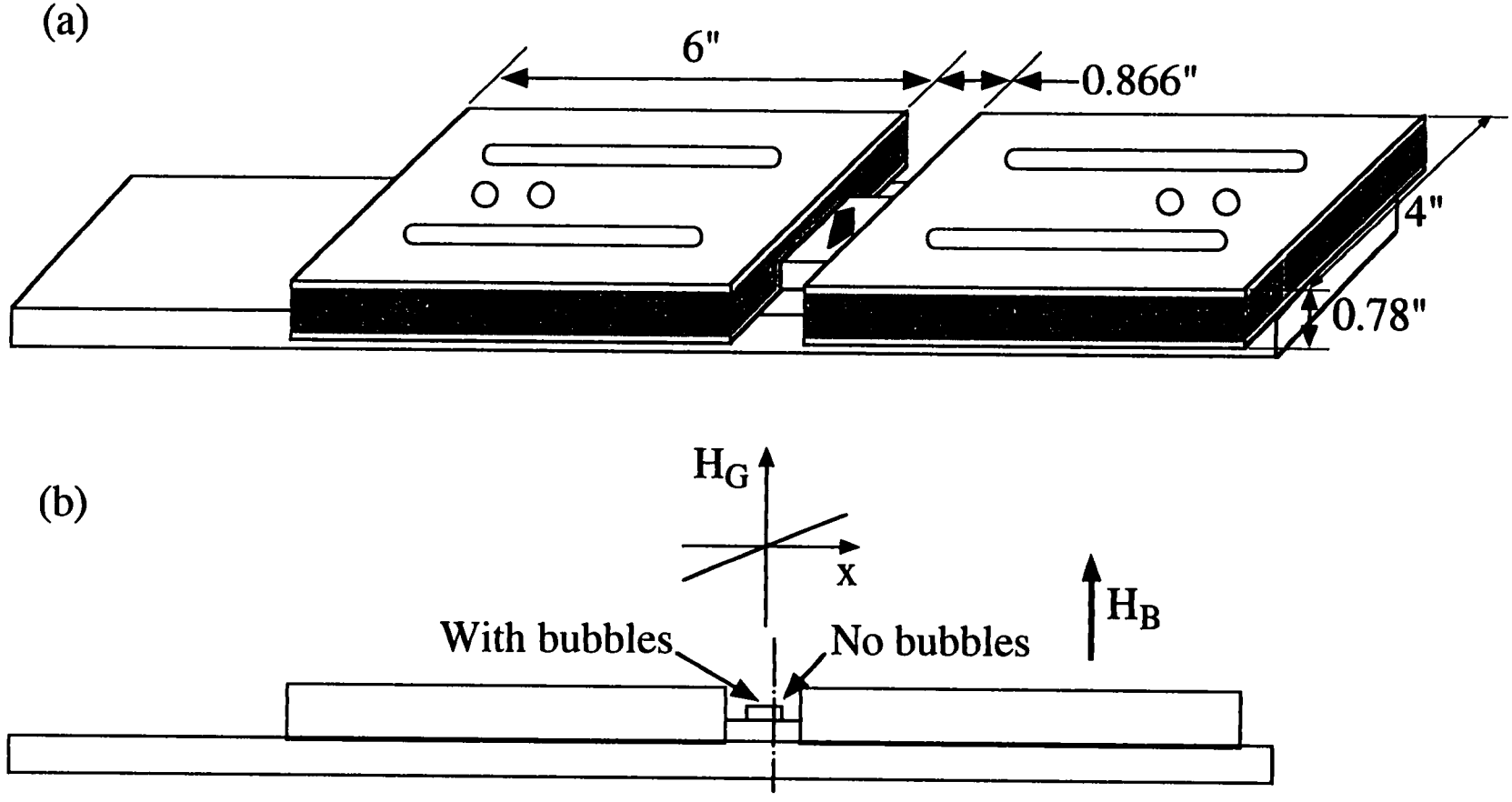

Fig. 3.4 (a) Schematic diagram of the gradient coils and the sample holder. Each coil contains 100 turns of close packed wires (hatched areas). The sample is shown as a black piece at the center between the two coils. The gradient coils and the sample holder are mounted on the aluminum frame. (b) Schematic illustration of gradient field measurement using bubble collapse field.

small steps and repeat the above step at every H_B, we can plot the interface location as a function of H_B. We then fit the data points linearly. The field gradient is

$$[\nabla H_z(x)]_x \text{ (Oe/}\mu\text{m)} = 0.00116\ I_G \text{ (amp)}. \tag{3.3.3}$$

The corresponding force a magnetic bubble feels is

$$F \text{ (dyn)} = 9.08 \times 10^{-8}\ I_G \text{ (amp)}, \tag{3.3.4}$$

assuming the bubble has diameter 6.5 μm and height 7.8 μm. The curve-fitting also shows the force is uniform to better than within 0.8% over 8600 μm in the center region. The current capacity is 10 amps from Joule heating consideration. However the actual maximum current is smaller, ~ 4 amps, limited by the field difference over the garnet sample. A higher magnetic field gradient creates a gradient in bubble concentration in the field gradient direction. A serious concentration gradient would cause diffusion of bubbles in the opposite direction. Both the core of the gradient coils and the supporting frame underneath are made of aluminum, because it is nonmagnetic and has good thermal conductivity. In our garnet samples, the bubble state is always S = 0 so there is no deflection during driven bubble motion.

3.4 Pinning of Magnetic Bubbles

In the commensurate-incommensurate transition experiment which we will discuss in Chapter 5 and shear flow measurement which we will discuss in Appendix A, we pin the magnetic bubble array with thin permalloy overlayers. A high resolution chromium optical mask is made at Advance Reproduction according to our design of the pinning geometry. We then fabricate the pinning pattern on the garnet sample using photolithography, electron

beam evaporation, and lift-off techniques in a cleanroom environment. The pinning patterns can be erased without damaging the garnet film by immersing the sample with permalloy patterns in a solution of 1:40 HCl : H_2O for about 1 minute and then rinsing it with water [Seshadri, 1992a].

In our pinning experiments the permalloy layer was typically between 30 Å to 100 Å. The permalloy layer is transparent gray within this thickness range. We can easily identify the location of the permalloy patterns under optical microscope and also see the bubbles underneath through the permalloy layer. Permalloy layers thicker than 100 Å produce a stronger pinning, different from the regime in which we are interested.

The garnet sample is cut from a 3" wafer of LLC garnet using a diamond saw. We use a Low Speed Diamond Wheel Saw Model 650 made by South Bay Technology. Bubble material is grown on both surfaces of the wafer, but we use the side with a higher collapse field for our experiments. The sample is always handled with caution to avoid being scratched. The procedures are follows:

1) Mount the wafer on a graphite plate. The wafer and the graphite plate are heated to 90°C with a hot plate. The side with a lower collapse field is glued on the graphite plate with melted wax. They are then cooled down to make sure they stick well.

2) Cut the wafer. The wafer and the graphite plate are mounted on the diamond saw. In order to achieve smooth cutting edge, the speed dial is set to 3 and an appropriate tension is exerted on the arm by turning the weight on the saw inward 10 to 15 turns from zero tension position. The diamond saw is being cooled during cutting by coolant made by the same company (P/N 02-02420) diluted with 50 times of water.

3) Separate and clean the sample and the wafer. The sample, the remaining wafer, and the graphite plate is removed from the diamond saw once cutting is finished. The sample and the wafer are then separated by heating up to 90°C. Wax is washed off the sample and the wafer with trichloroethylene at 75°C.

In the photolithography step a reverse pattern of photoresist is made on the sample. Photolithography is performed in a class 100 cleanroom according to the following procedures:

1) Cleaning. Both sample and mask are cleaned in ultrasound (~ 10 minutes / step) with trichloroethylene, acetone, and methanol consecutively, and are then blown dry with nitrogen gas. The clean sample is baked in an oven at 180°C to 200°C for 10 to 15 minutes to remove moisture.

2) Photoresist coating. Photoresist Shipley Microposit 1813 is applied on the sample placed on the vacuum chuck of spinner. The spinner is then turned on for spinning at 150 rpm for 1 to 2 sec and 4000 rpm for 30 sec. As a result, the sample is coated with a 1 μm layer of photoresist uniformly. It is further baked on a hot plate at 105°C for 3.5 minutes to dry the photoresist so that it would react with UV light well.

3) Exposure and development. The sample is aligned with the chromium mask on Karl Suss Model MJB3 Contact Mask Aligner and exposed with mid UV in soft contact mode for 5.5 sec. It is then developed in Shipley Microposit 351 developer diluted with 5 times of water for 45 to 60 sec. The developed sample is then rinsed thoroughly with water to avoid overdeveloping.

In the evaporation step a layer of permalloy is uniformly deposited on top of the sample. Evaporation is performed in a class 10,000 cleanroom. We use an Edward E306A electron beam evaporator. The evaporation material is permalloy powder composed of 80% Ni and 20% Fe. The thickness of the permalloy layer is monitored roughly using a crystal thickness monitor (Edward Model TM-100) during evaporation. After the evaporation this thickness is measured again with a much more accurate Alpha-Step 200 made by Tencor Instruments. To avoid damaging the sample and to improve the precision during this second measurement, we always evaporate another pattern on a piece of cover glass together with our sample, and the pattern on the cover glass is measured. The pattern

on the cover glass has a larger size (≥ 100 μm) than the typical feature size of the permalloy pattern (~ 10 μm).

After the final lift-off a pinning pattern of permalloy is obtained. The sample taken out of the evaporator is immersed into Shipley Microposit 1112A remover which is heated up to 90°C with a hot plate. The remover dissolves photoresist. The permalloy deposition on top of the photoresist is lifted off after about 3 hours while that on top of the garnet film remains. Occasionally the lift-off is not complete even after more than 4 hours. In this case we use a swab to gently remove the unwanted permalloy.

3.5 Image Processing and Data Analysis

The image acquisition, processing, and analysis software is developed in C language and shell scripts in a Silicon Graphics workstation. The functions in the Silicon Graphics graphics library are called extensively. Table 3.1 is an overview of the major applications we developed. Sample source code is listed in Appendix B.

Bubble array images are captured using an IndigoVideo real time video card driven by a custom developed program *LiveVideo.c*. This program is developed for the general case that a sequence of bubble array images need to be captured at constant time intervals. The number of frames to be captured and the time interval are the two input parameters to this program. When only a single bubble array image is needed, both parameters are set to 1. Timing is controlled by the internal clock of the workstation. Each image in the series is labeled with a unique frame ID, from which relative timing of the images can be determined. The upper limit of the image capture rate is 1 frame/sec at full image size 640 x 480 pixels^2. Faster capture rate can be achieved by reducing the image size. The captured images are stored as digitized grayscale images in SGI format, a standard image format for Silicon Graphics workstations. The gray level at each pixel is represented by an integer, grayscale value. It is an integer between 0 and 255, where 0 being black and 255 being

Table 3.1 Overview of Bubble Analysis Applications (*.c represents C code and files without .c represents shell scripts)

Category	Applications	Usage
Image Acquisition	LiveVideo.c	captures single or continuous full video frames. maximum capture rate: 1 frame/sec
Image Processing	FindCenters.c	determines center coordinate of every bubble over the field of view.
Data Analysis	defect	performs Voronoi construction
	transcorr orientcorr	calculates translational correlation functions of bubble array. calculates orientational correlation functions of bubble array.
	FindVelocity.c	calculates individual bubble velocity in the bubble array from 4 sequential video frames.
	NewDrawCluster.c NewDrawCluster1.c NewDrawCluster2.c NewDrawCluster3.c	draw velocity field to show bubble flow.
	vvcorr.c	calculates velocity-velocity correlation function of bubble array.
	StrucFunc.c StrucFuncw.c	calculates structure function of bubble array without any window. calculates structure function of bubble array with a Hanning window.
	LTcorr.c	calculates structural and commensurability correlation functions of bubble array with periodic line pinning.
	Symbrkg1.c Symbrkg2.c	draw bubble array image with binary color coded bubbles to show how symmetry breaking happens.

white. To print the images on paper, they are first converted to TIFF format using a commercial application *imgcopy* in Silicon Graphics workstations, then are transferred to Macintosh computers via ftp in binary mode, and finally they are printed out using a HP LaserJet 4MV with a resolution of 600 dpi (dots per inch).

Once the images are captured, a custom developed application *FindCenters.c* is used to perform image processing and obtain bubble center data, because quantitative analyses of the properties of magnetic bubble arrays are based on the bubble center locations. Image processing consists of filtering, thresholding, and edge detection, as shown in Figs. 3.5(a) to 3.5(c). Only 600 x 440 pixels^2 in the center region of a video image are used, because the pixels near the edge of a video image are often accompanied by distortions.

Figure 3.5(a) is the original grayscale image of a bubble array. Often there are some spurious darker regions in a raw image, such as those on the lower left and lower right corners of Fig. 3.5(a), due to dust on the sample or scratches on the Lucite sample holder. They make both the bubble domains and the background darker than other parts of the image. They can be cleaned in the filtering step described as follows: an image is first divided into areas of 20 x 20 pixels^2 and the average grayscale value of these small areas is calculated for each of these small areas. These values are often not the same: the value for a darker region is smaller than that for a regular area. To suppress the spurious darker regions, the average grayscale value is subtracted from the original grayscale value at each pixel of the same small area. Then a constant integer, 128 in our program, is added to each pixel's grayscale value to make the grayscale value between 0 and 255. If the grayscale value is over 255 (below 0) after addition, it is set to 255 (0). The filtering step effectively removes the darker regions and makes the image background uniform.

The filtered grayscale image is then converted to a black-and-white image by thresholding: a threshold grayscale value is chosen so that for pixels with grayscale value above the threshold, they are set to white, otherwise black. The black disks are bubbles. We can edit the black-and-white image interactively by zooming in the image and removing

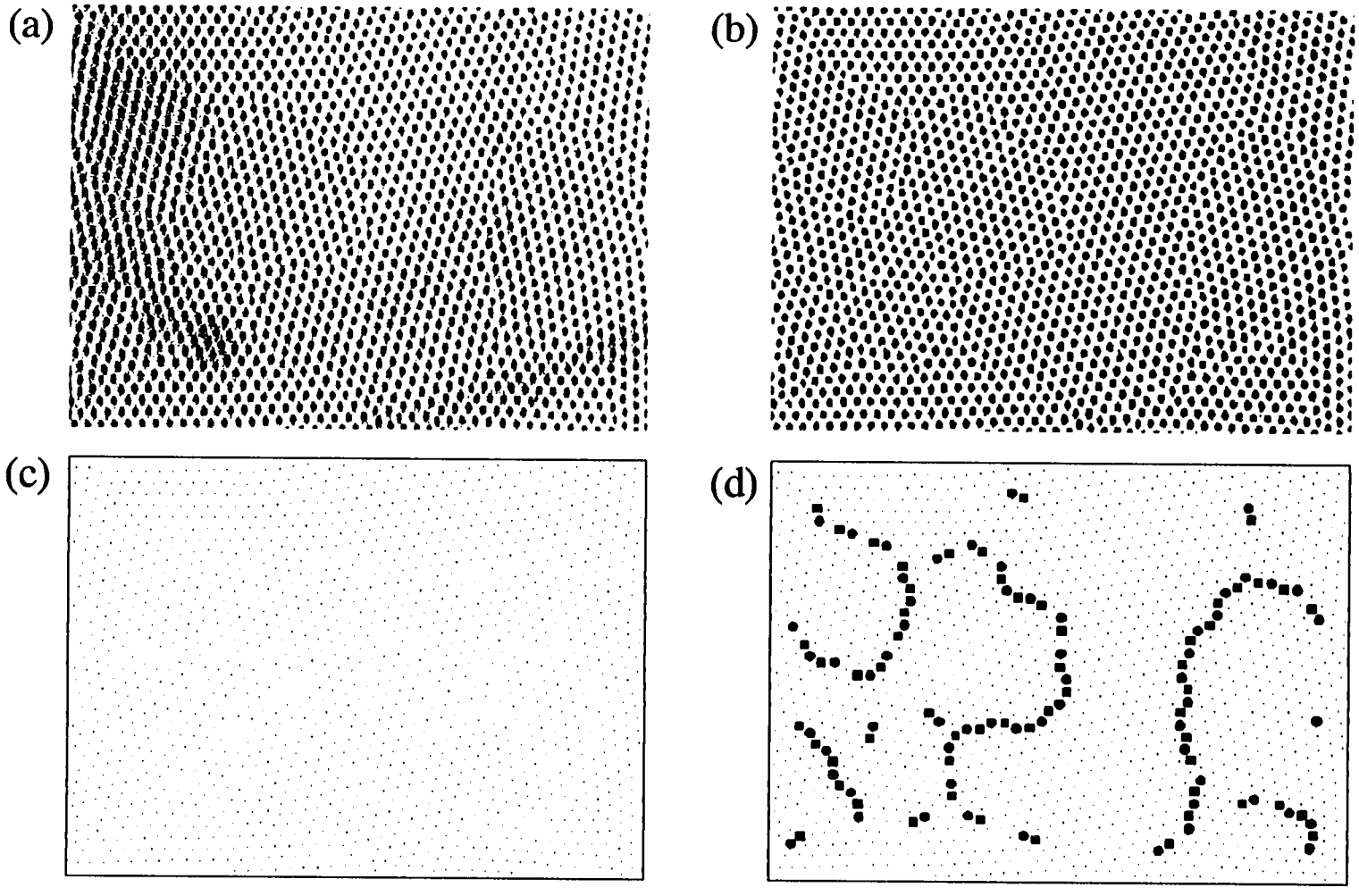

Fig. 3.5 Image processing and defect diagram. (a) Original grayscale image of a bubble array. (b) Black-and-white image. (c) Image showing bubble center positions. (d) Defect diagram of the bubble array. Black square represents a bubble with 5 nearest neighbors, and black circle represents a bubble with 7 nearest neighbors.

spurious pixels or filling in missing black pixels. Figure 3.5(b) is a black-and-white image after editing. The bubble center locations are determined in the edge detection step from the black-and-white image: a recursive function is used to find the edge of each black disk, i.e., each bubble, then the center of a bubble is calculated by averaging the positions of all the black pixels surrounded by the edge. A lower limit of bubble size is used to reduce spurious black pixels. Figure 3.5(c) is an image showing bubble center locations. A comparison of the bubble center locations and the original bubble array image shows that we can correctly determine the bubble centers using the above image processing techniques.

Figure 3.5(d) is a diagram showing topological defects in the bubble array identified from the bubble center data using Voronoi constructions. For a perfect two-dimensional triangular bubble lattice, each bubble has six nearest neighbors. If a bubble has other than six nearest neighbors, then it is a disclination, a type of topological defects. A bubble with five nearest neighbors is a five-fold disclination, indicated by a black square in Fig. 3.5(d). A bubble with seven nearest neighbors is a seven-fold disclination, indicated by a black circle in Fig. 3.5(d). Four- and eight-fold disclinations are also observed in very disordered bubble arrays. They are indicated by open square and open circle respectively. A bound pair of five- and seven-fold disclinations forms a dislocation. The Voronoi construction creates a Voronoi diagram that divides the space into Voronoi polygons, analogous to Wigner-Seitz unit cells for a Bravais lattice. A Voronoi polygon about a bubble is a region that is closer to that bubble than any other bubbles. It is constructed in the following way: a line connecting the bubble to all others in the space is drawn, then another line (a bisector) bisecting each line is drawn, and the smallest polygon containing the bubble bounded by these bisectors is the Voronoi polygon. Application *defect* uses a Voronoi construction algorithm developed by Fortune [1987] to identify the number of nearest neighbors a bubble has and indicate them on the defect diagram if the coordinate numbers are other than six.

Other data analysis applications listed in Table 3.1 are specific to a particular experiment and will be discussed in Chapters 4 and 5.

CHAPTER 4 COLLECTIVE TRANSPORT

In this chapter we present detailed spatiotemporal observations of collective transport phenomena in two-dimensional magnetic bubble arrays subject to random substrate roughness. As discussed in Chapter 2, substrate roughness provides a weak random point-like pinning for the bubbles. Thermal motion is simulated by an adjustable ac magnetic field and bubble transport is driven by a dc gradient field. From direct observation of the bubble transport, we studied the spatiotemporal mechanism for depinning and motion. We also examined the microscopic origins of friction and drag. From measurements made in the nonlinear regime of low bubble velocities, we found that the average array velocity v responds to the applied force F according to the power law $v \propto F^{\alpha}$ with $\alpha \cong 3$. We also found that the measured velocity-velocity correlation function decays exponentially and the velocity-velocity correlation length increases with the applied force.

This chapter is organized as follows. In Section 4.1 we provide the necessary background for our collective transport experiment. In Section 4.2 we review the theory of collective transport of two-dimensional elastic systems. In Section 4.3 we describe the experimental procedures and the characteristics of the bubble array used for this experiment. In Section 4.4 we discuss the velocity-force responses of the bubble array at different ac magnetic fields. In Sections 4.5 and 4.6 we describe two microscopic properties of the transport: spatial and temporal correlations. The time-resolved bubble array images provide direct evidence for a collective motion rather than an independent motion. In Section 4.7 we discuss the behavior of the measured velocity-velocity correlation function and the correlation length as a function of applied force. In Section 4.8 we summarize the major results of this experiment.

4.1 Introduction

The microscopic origins of friction and drag in transport of many physical systems has long been an interesting and controversial issue. There are two types of transport phenomena: one involving independent motion of objects and the other involving collective motion [Fisher, 1987]. This chapter focuses on collective transport. Interesting and important spatiotemporal phenomena arise in a wide variety of different contexts due to the competition between internal ordering forces and external disorder: frictional motion of two-dimensional elastic membrane [Vallette and Gollub, 1993; Feder and Feder, 1991], earthquakes [Carlson and Langer, 1989], surfaces of crystals growing on disordered substrates [Tsai and Shapir, 1992], sliding charge density wave transport [Grüner, 1988; Coppersmith, 1990; Fisher, 1983; 1985], and flux flow in type II superconductors [Koch *et al.*, 1989; Huse, Fisher, and Fisher, 1992; Nelson and Vinokur, 1992]. Figure 4.1 illustrates a model for collective transport: the system has a large number of interacting objects which are subject to a random static pinning potential. If the system is a crystal, the pinning potential is manifested macroscopically as friction during transport; if the system is a liquid, the pinning is manifested macroscopically as drag during transport. A uniform force is applied to the system to make the objects move. Because the forces between the objects can be as strong as or stronger than the applied driving force, there can be a high degree of coherence in the transport. When the pinning is strong, some objects are permanently pinned and transport is characterized by channel flow [Jensen *et al.*, 1988a; 1988b; Narayan and Fisher, 1994]; when the pinning is weak, the whole system moves with a typical coherence length ξ_v [Fisher, 1987]. The subscript v means this correlation length is related to velocity. We will concentrate our discussion on weak pinning because the substrate pinning in the magnetic bubble system belongs to this category.

For a two-dimensional array with a large number of interacting objects and subject to a weak random pinning potential, the spatially averaged velocity v responds differently to

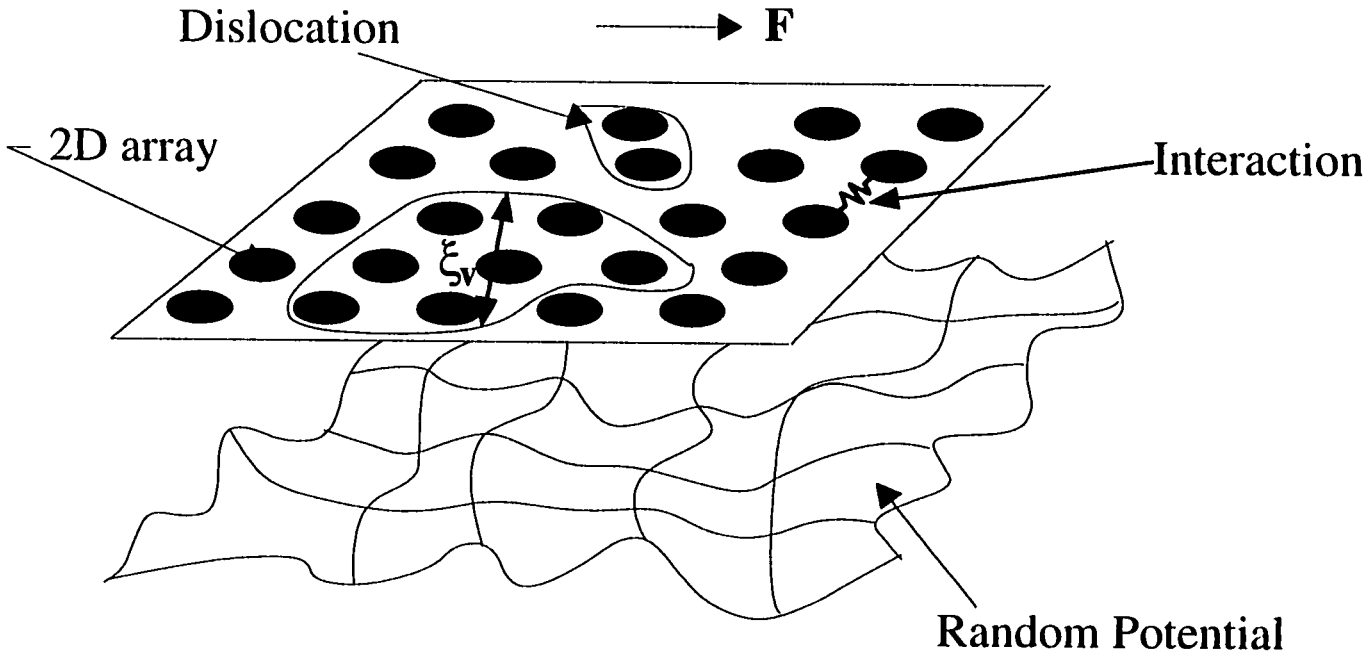

Fig. 4.1 Schematic illustration of a two-dimensional collective transport system.

the applied force F in different temperature regimes, as illustrated in Fig. 4.2. At zero temperature there is a depinning threshold F_T below which the system is pinned. Depinning happens when F exceeds F_T, and the nature of the depinning transition has attracted considerable attention. In the case of charge density wave transport, the Fukuyama-Lee-Rice model [Fukuyama and Lee, 1978; Lee and Rice, 1979] predicts the existence of a unique threshold, while Coppersmith [1990] argued that phase slips lead to the destruction of a depinning threshold. At finite temperatures a nonzero array velocity is expected for any applied force because of creep [Fisher, 1985]. Interesting dynamic behavior happens in the nonlinear regime below a critical temperature T_c. Above T_c or at large forces the response is linear because pinning is negligible relative to the thermal energy or the applied force. Below T_c both the two-dimensional vortex glass model and the defect free elastic media model predict a power law velocity-force response. In the former case the power law comes from the interaction between dislocations [Fisher, Fisher, and Huse, 1991] while in the latter case it comes from the balance between elastic energy and random point pinning [Batrouni and Hwa, 1994; Carraro and Nelson, 1996]. Theories also predict a variety of spatiotemporal behaviors associated with the microscopic picture of the collective motion [Fisher, 1987; Carlson and Langer, 1989; Coppersmith, 1990].

Using the two-dimensional magnetic bubble system as a model system to study collective transport phenomena has advantages over most other computational or experimental systems. Although computational study is important for our understanding, a computational model is often different from a real experimental system and is often limited to a small system size and short duration. By contrast, the magnetic bubble system is a physical system in which interaction and pinning are real and relatively well understood. In addition, even a small sample of size 5 x 10 mm^2 contains over 150,000 bubbles, which is much more than the number of objects a computational study can deal with. On the other hand, it is difficult to observe in real time the individual objects in most experimental

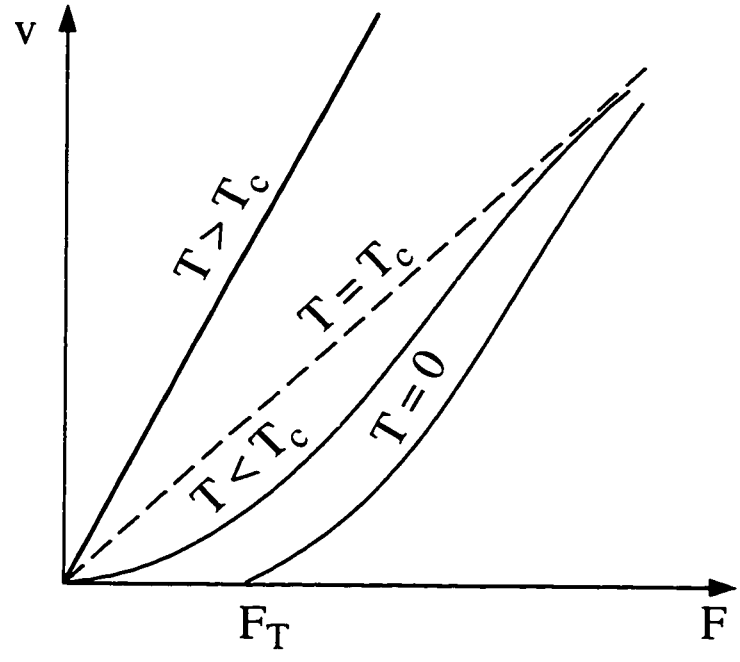

Fig. 4.2 Schematic velocity-force responses at different temperature regimes predicted by collective transport theory.

systems, such as charge density waves and type II superconductors, so measurements are often limited to macroscopic quantities, such as current-voltage characteristics [Koch *et al.*, 1989]. Direct observation of individual bubbles in the array in real time can be easily achieved by means of the Faraday effect and computer-video techniques. The locations and velocities of individual bubbles as well as the locations of topological defects can be determined using image processing techniques.

4.2 Theory of Collective Transport

In this section we summarize the important results in the collective transport theory. The relevant theory for magnetic bubble transport is the transport of a two-dimensional elastic media subject to weak random-point pinning [Batrouni and Hwa, 1994; Carraro and Nelson, 1996]. The elastic media theory describes a defect free system or a system in which the dislocations move with the objects, where the motion creates only elastic distortion and there is no creation or annihilation of dislocations during motion. The bubble arrays in the transport experiment possess these properties. When dislocations are present and move during transport, the phenomenon is described by vortex glass theory [Fisher, Fisher, and Huse, 1991].

At finite temperatures the spatially averaged velocity v of an extended system is given by the collective flux creep theory [Feigel'man *et al.*, 1989]:

$$v \propto e^{-U(F)/k_B T}, \qquad \text{for } T < T_c, \tag{4.2.1}$$

where U(F) is an energy barrier associated with the nature of collective motion. In the three-dimensional case it was found that U(F) is proportional to F^{-v}, i.e. $U(F) \propto F^{-v}$ [Fisher, 1985; Fisher, Fisher, and Huse, 1991; Feigel'man *et al.*, 1989]. This leads to a strongly nonlinear response of the form

$$v \propto e^{-(F_0/F)^{\nu}}, \qquad \text{for } T < T_c. \tag{4.2.2}$$

In two-dimensional elastic media with weak random pinning in the absence of topological defects, the balance between elastic energy and pinning of point impurities gives an energy barrier of the form $U(F) \propto \ln(F/F_0)$. This logarithmic energy barrier leads to power-law velocity-force responses [Batrouni and Hwa, 1994; Carraro and Nelson, 1996; Tsai and Shapir, 1992]:

$$v \propto F^{\alpha}, \qquad \text{for } T < T_c. \tag{4.2.3}$$

For weak pinning α only depends on temperature, the Lamé coefficients λ and μ, and is independent of the pinning strength. The pinning strength is reflected in the coefficient in front of F^{α}.

The uniform driving force F and the interaction between objects tend to make the system move coherently while the random pinning reduces the degree of coherence. The instantaneous velocity of individual objects fluctuates during motion. The instantaneous velocity-velocity correlation function $C(r_{ij})$ measures the coherence of the transport and is predicted to decay exponentially with object-object separation at zero temperature [Fisher, 1987]:

$$C(r_{ij}) = \left\langle \left(\frac{\partial x_i}{\partial t} - v \right) \left(\frac{\partial x_j}{\partial t} - v \right) \right\rangle \propto \exp\left(-\left| \vec{r}_i - \vec{r}_j \right| / \xi_v \right), \tag{4.2.4}$$

where $\vec{r}_i$ is the position of the site i and v is the spatial averaged velocity which is assumed to be in the $\hat{x}$ direction. The correlation length ξ_v is defined as the decay length of the correlation function $C(r_{ij})$ and ξ_v characterizes the size of regions that move coherently.

A characteristic length scale ξ_0 can be defined and is called the Lee-Rice length [Fukuyama and Lee, 1978; Lee and Rice, 1979]. The Lee-Rice length ξ_0 is given by [Fisher, 1987]

$$\xi_0 \sim a\frac{K}{\Phi}, \tag{4.2.5}$$

where K is the elastic constant and Φ is the typical pinning strength. Areas of size ξ_0^2 act like a single degree of freedom. The depinning threshold force F_T is then given by [Fisher, 1987]

$$F_T \sim \frac{K}{a}(\xi_0/a)^{-2}. \tag{4.2.6}$$

4.3 The Experiment

In this section we describe the experiment performed to study the spatiotemporal phenomena of collective transport in two-dimensional magnetic bubble arrays. Experimental results are presented in subsequent sections.

Figure 4.3 is an image of a typical bubble array used in our measurements. The size of the large lattice constant garnet sample used for our transport experiment is 6 x 25 mm^2. Transport of the bubble array at several different ac magnetic field values is studied. For each ac field, a disordered sea of bubbles is first created and then annealed at H_B = 75 Oe and H_{ac} = 20.7 Oe at 40 Hz overnight to obtain a nice triangular bubble array. The dc bias field H_B is then held fixed at 75 Oe while the ac field is brought down to desired value. The array is given 1.5 hours to anneal further before any force is applied. The resulting bubbles have a diameter of 6.5 μm and a concentration of 2996 mm^{-2}. A 5x objective and

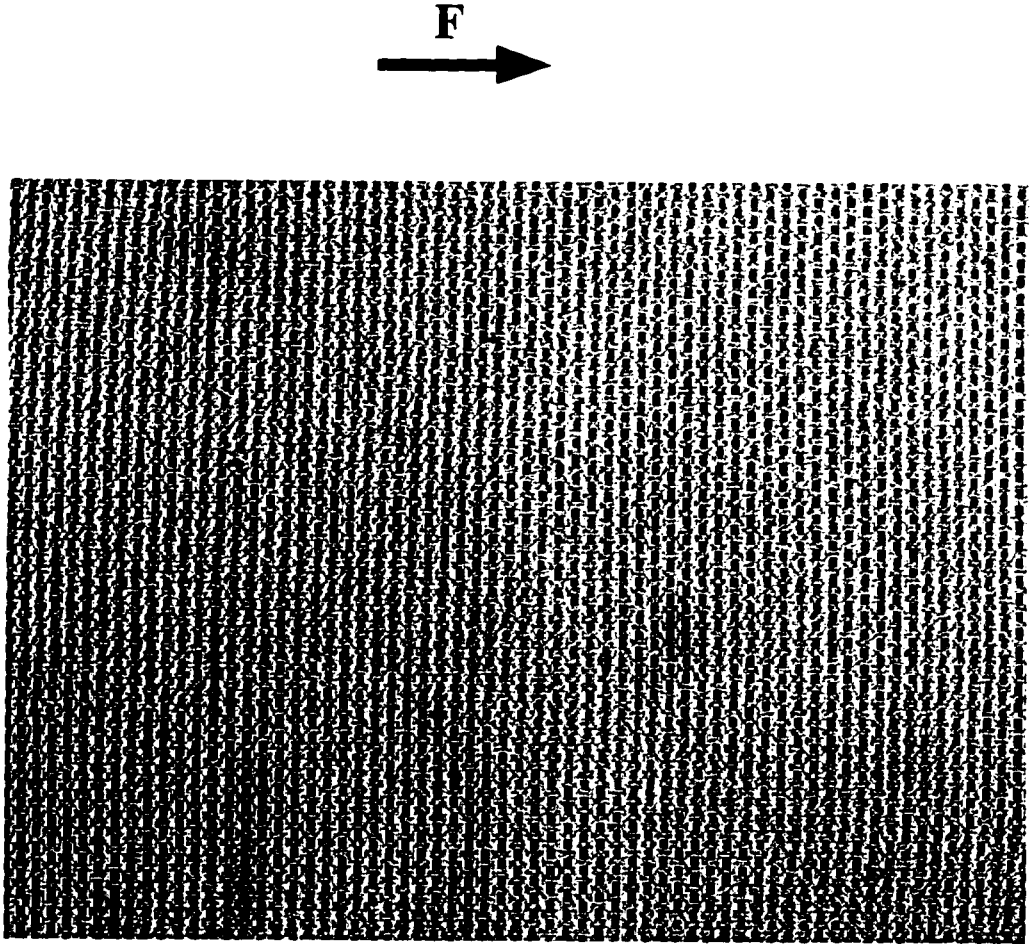

Fig. 4.3 An image of bubble array for collective transport measurement at H_{ac} = 13.6 Oe. The image size is 1024 μm x 760 μm.

a 3.3x eyepiece are used for observation. There are no topological defects over the field of view. The array characteristics and properties were as follows.

We examined translational and orientational order of the bubble array from the bubble center data using the translational and orientational correlation functions. The translational correlation function is defined as

$$G_T(r_{ij}) = \left\langle e^{i\vec{k}\bullet(\vec{r}_i-\vec{r}_j)} \right\rangle, \tag{4.3.1}$$

where the angular brackets indicate an average of all pairs of bubbles separated by a fixed scalar distance r_{ij}. The correlation function $G_T(r_{ij})$ measures the deviation of objects from their perfect lattice points. The value $G_T(r_{ij}) = 1$ means that the bubble array is a perfect lattice and $G_T(r_{ij}) = 0$ means that the bubble array is completely random. The orientational correlation function is defined as

$$G_\theta(r_{ij}) = \left\langle e^{i6\left(\theta(\vec{r}_i)-\theta(\vec{r}_j)\right)} \right\rangle, \tag{4.3.2}$$

where $\theta(\vec{r}_i)$ is the angle of the vector $\vec{r}_i$ relative to a given direction for fixed scalar distance r_{ij}. The correlation function $G_\theta(r_{ij})$ measures the deviation of objects from their original lattice orientation. The computer shell scripts to calculate these correlation functions from bubble centers are *transcorr* and *orientcorr* (Table 3.1). Both correlation functions for the array shown in Fig. 4.3 are plotted in Fig. 4.4. As shown in the figure, $G_T(r_{ij})$ decays exponentially:

$$G_T\left(r_{ij}\right) = e^{-r_{ij}/\xi_T}. \tag{4.3.3}$$

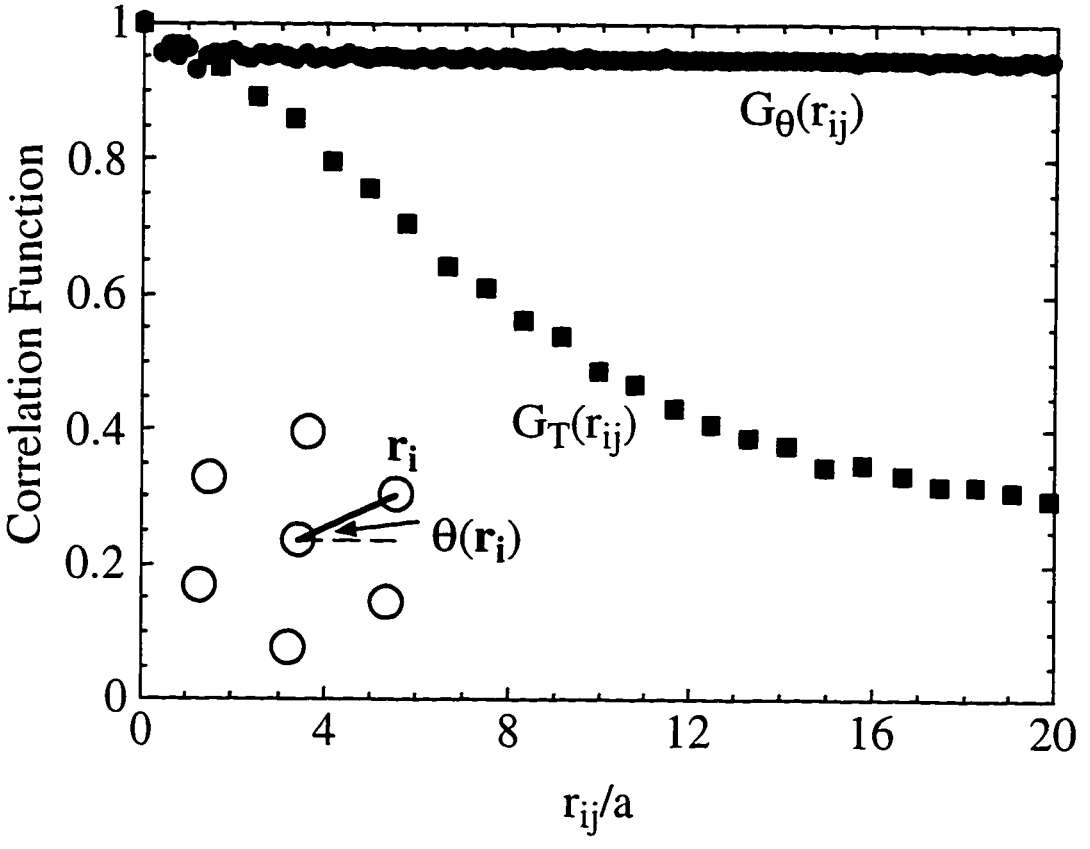

Fig. 4.4 Measured translational and orientational correlation functions $G_\theta(r_{ij})$ and $G_T(r_{ij})$ for the bubble array shown in Fig. 4.3.

The decay length ξ_T is called the translational correlation length. For the array shown in Fig. 4.3, ξ_T = 15a where a is the average bubble spacing. The translational correlation lengths for other arrays we studied are between 8a to 15a. Figure 4.4 also shows that $G_\theta(r_{ij})$ remains almost constant and is close to unity; thus the array has a quasi-long range orientational order. Systems with quasi-long range orientational order but short translational order are often referred to as hexatics [Nelson and Halperin, 1979; Murray and Wenk, 1989; Seshadri and Westervelt, 1991].

In bubble transport, the velocity of each bubble is determined from the bubble displacement over four consecutive video frames taken at constant time intervals. The time interval between two video frames has to be carefully chosen so that the bubble displacement between the two frames is much less than one bubble spacing, otherwise it is difficult to identify the same bubble in different video frames. Four video frames rather than two video frames are used so as to make it possible to track the motion of individual bubbles over a longer displacement. The C program *FindVelocity.c* carries out this velocity computation from experimental data. The array velocity v is computed by averaging over all the bubbles in a video frame.

The experiment was performed by recording bubble array transport data for a series of increasing forces F as follows. For each data point, an in-plane force produced by a magnetic field gradient is applied to make the array move a distance up to 3a, then the force is removed and the array is given adequate time to relax. This distance is a factor ~ 100 longer than the length scale of the random pinning (~ 0.4 μm) [Seshadri and Westervelt, 1992b]. The maximum bubble displacement is limited by compression of the bubble array in the entire sample. As bubbles move along the $\hat{x}$ direction, the bubble concentration at the right end of the sample increases while that at the left end decreases because neither creation nor annihilation of bubbles occurs. A pressure caused by this concentration gradient builds up in time in the direction opposing the driving force.

To ensure high precision bubble displacement measurements, we control the room temperature with a thermostat and carefully fix the aluminum-Lucite sample holder at the center to suppress thermal expansion of aluminum frame. Measurements show the imaging error due to thermal expansion is less than 1 pixel/3.3°C.

4.4 Velocity-Force Responses

Now we discuss the measured array velocity-force responses. Figure 4.5 shows the measured average array velocity v vs applied force F at four values of the ac magnetic field H_{ac}. As discussed in Section 2.5, in the absence of any ac field, the bubble array is pinned by defects and inhomogeneity of the substrate within the available range of applied force. As shown in the figure, the velocity-force response is nonlinear, in agreement with current theory for two-dimensional systems [Batrouni and Hwa, 1994; Carraro and Nelson, 1996]. Figure 4.6 shows the velocity-force response on log-log scale. The velocity is scaled with a parameter c. All data points fall along the same line $v/c = F^3$ on the scaling plot over three decades in velocity. The power law scaling in Fig. 4.6 shows that the velocity-force response does not display a depinning threshold for array motion. The inset in Fig. 4.6 plots the parameter c vs the ac field. A higher ac field gives rise to a larger c. We have also tried to fit our data using Eqn. (4.2.2), but the result is poor: most data points fall on one side of the fitted curves, rather than uniformly fall on both sides of the curves.

Power law velocity-force characteristics have been predicted for defect-free elastic media [Batrouni and Hwa, 1994; Carraro and Nelson, 1996] and also for certain two-dimensional cases due to the interaction of dislocations [Fisher, 1985; Fisher, Fisher, and Huse, 1991]. Elastic media theory is more appropriate to our experiments because the measured dislocation concentration of the bubble array is very small, ~ 4 over the field of view, and the dislocations present are fixed in the array, i.e. they move with the bubble

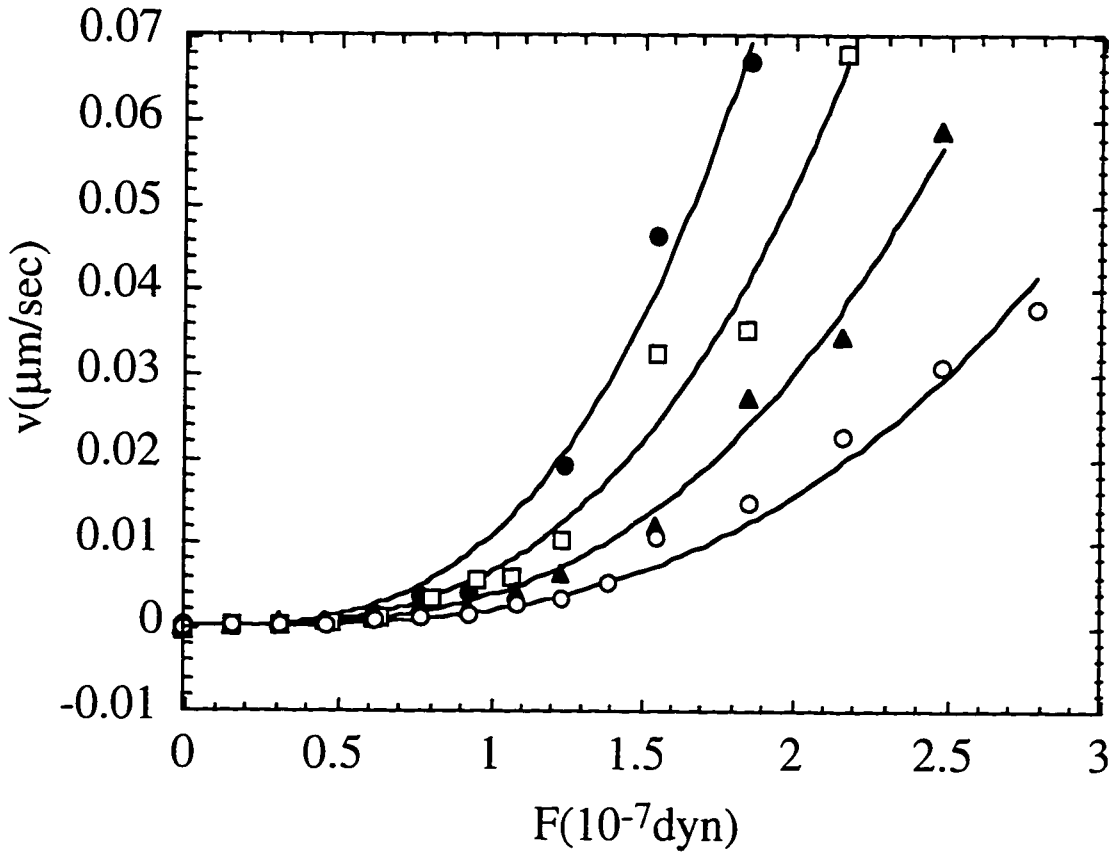

Fig. 4.5 Velocity-force response of the magnetic bubble array for ac magnetic field values H_{ac} = 10.1 Oe (open circles), 13.6 Oe (black triangles), 17.2 Oe (open squares), and 20.7 Oe (black circles). The solid lines are power-law fits with $v = cF^3$; c is the fitting parameter.

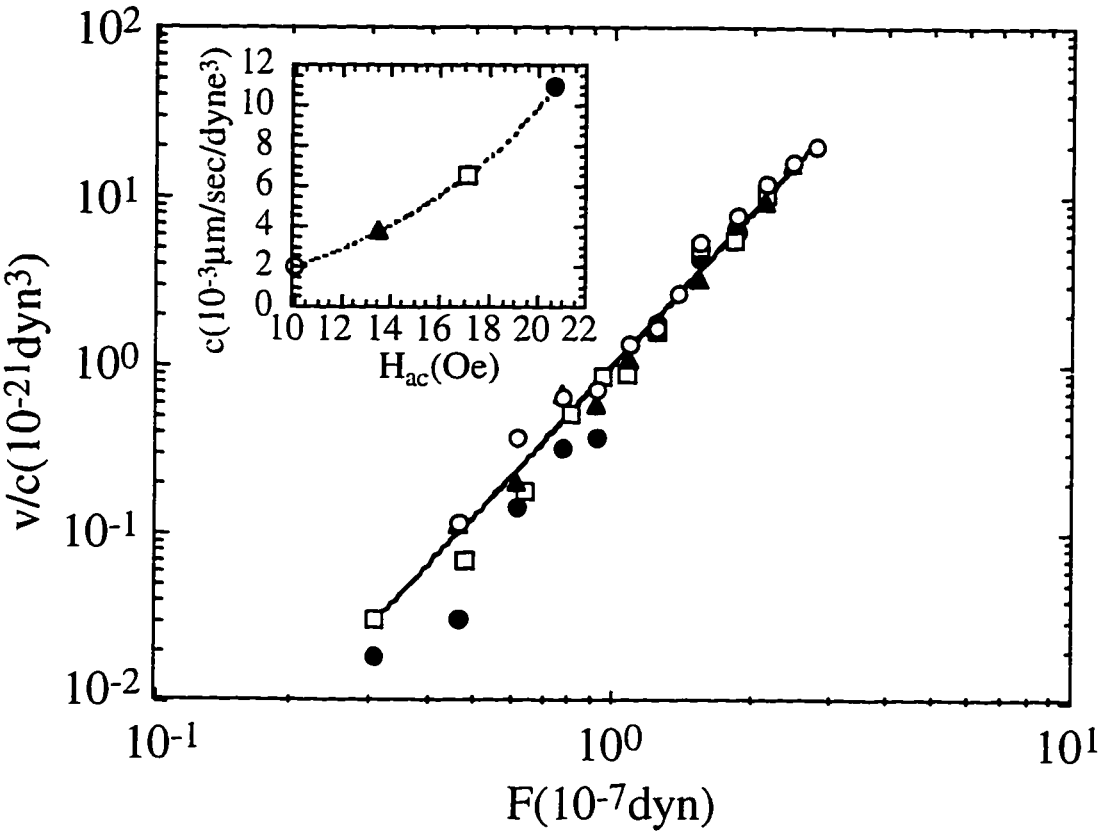

Fig. 4.6 Scaling plot of the velocity-force responses of those shown in Fig. 4.5; the solid line is $v/c = F^3$. Please see caption of Fig. 4.5 for meaning of symbols. The inset is the parameter c vs the ac field. The dashed line is a guide to the eyes.

array. We characterize the effective thermal fluctuation of the magnetic bubble array induced by ac field by measurements of the standard deviation σ of the bubble displacement over 24 minutes in the absence of any applied force. We find similar values $\sigma/a = 0.039 \pm 0.004$ for the four ac fields shown in Figs. 4.5 and 4.6. It is interesting that although a higher ac field reduces the pinning strength, thereby makes the array move more freely, the effective temperature represented by σ/a does not increase appreciably. The elastic media theory predicts that the exponent α in the formula $v = cF^{\alpha}$ only depends on temperature and the Lamé coefficients and is independent of the pinning strength, while the constant c could depend on the pinning strength. The measured velocity-force responses agree well with the above predictions. A comparison of σ/a with Lindemann criterion $\sigma/a \cong 0.1$ for melting indicates that the bubble array is still well below the melting temperature.

The available range of ac agitation and array "temperature" is limited. We note that the ac agitation fields applied in the above measurements did not exceed the field H_{ac} = 20.7 Oe used to anneal the sample (see Section 3.1). To study bubble transport at higher ac fields, we have to anneal the sample at the same ac field or higher. Otherwise the bubble array would be in a nonequilibrium state where collapse of bubbles and rearrangement and annihilation of dislocations would occur. Such high annealing field would result in a serious reduction in bubble concentration. It is very difficult to prepare a bubble array with very few defects at such low bubble concentrations because of a much weaker bubble-bubble interaction.

4.5 Spatial Behavior of Bubble Transport

The ability to make microscopic observations of how transport takes place in bubble arrays is an important advantage of bubble arrays over other systems. Spatial velocity patterns can tell us the nature of the transport, that is, whether it is a collective motion of the

bubble array or a collection of independent motions of individual bubbles. These patterns can also reveal the nature of friction and drag and how different energies compete in the transport as the applied force changes. We have analyzed bubble velocity distributions for a series of forces at H_{ac} = 10.1 Oe. At this ac field the effective temperature is well below the melting temperature, according to $\sigma/a \cong 0.04$. The bubble velocities are obtained by dividing the displacements by the measurement interval $\Delta t = 2$ min. This time interval is chosen so it is long enough to minimize random fluctuations due to ac field agitation, but is still short enough so that the displacement is smaller than the bubble separation a.

Figure 4.7 shows the pattern of bubble motion in the bubble array at $F = 9.3 \times 10^{-8}$ dyn. The average array velocity at this force is v = 0.0014 μm/sec. On this image, each bubble is represented by a solid dot. The color of a dot represents the magnitude of its velocity averaged over 2 minutes. As shown the motion of the bubble array is spatially nonuniform. The fluctuations arise from ac agitation and random substrate pinning. The velocities of neighboring bubbles are correlated and neighboring bubbles form clusters with similar velocity as shown in Fig. 4.7.

In order to study spatial correlations and suppress the effect of ac agitation, we show in Figs. 4.8(a) to 4.8(c) velocity histograms and thresholded images of the moving array for three increasing values of applied force. In the absence of any applied force, the velocity distribution is approximately Gaussian due to the ac field. With an applied force, the velocity distribution deviates from a simple Gaussian as shown on the velocity histograms in Fig. 4.8. It develops non-thermal tails and bimodal structure. We artificially remove the Gaussian peak so that we can concentrate on the non-thermal tails and bimodal structure. We apply a cutoff velocity to the array as indicated by the arrow on the corresponding velocity histogram and only plot bubbles with velocities above the cutoff on the right of Figs. 4.8(a) to 4.8(c). For Figs. 4.8(a) and 4.8(b) the cutoff velocity is chosen to be 2 standard deviations of the main Gaussian peak, and for Fig. 4.8(c) the cutoff is chosen in the valley between the two maxima of the bimodal distribution. This simple

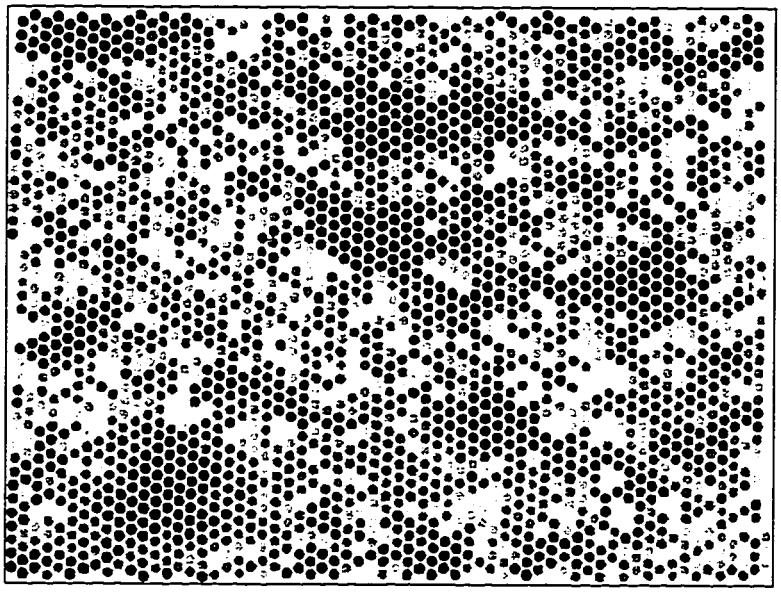

Fig. 4.7(color) Velocity distribution in the bubble array during a 2 min average at H_{ac} = 10.1 Oe and F = 9.3×10^{-8} dyn.

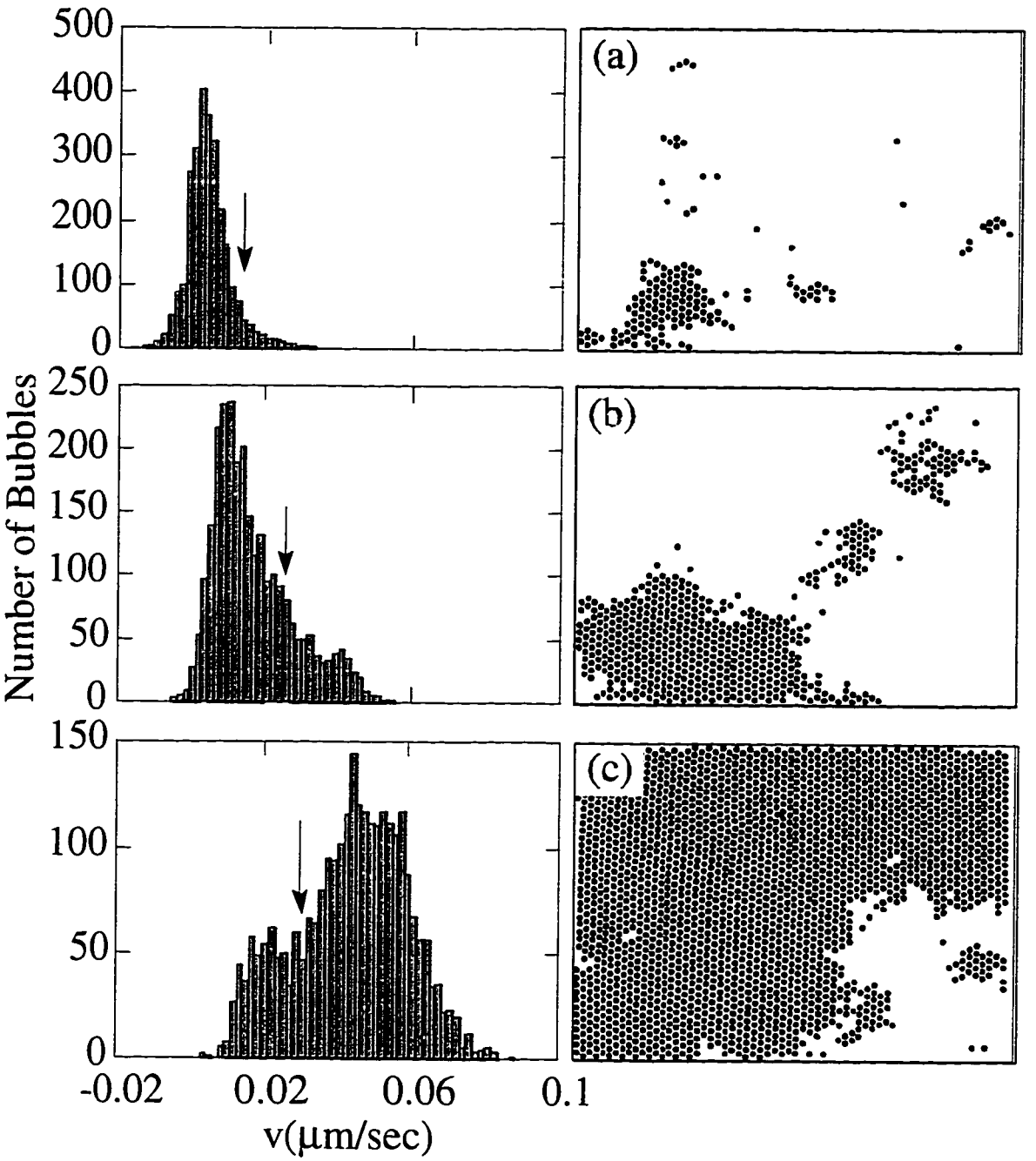

Fig. 4.8 Histograms of bubble velocity and distributions of moving bubble clusters for H_{ac} = 10.1 Oe and (a) F = 0.93x10^{-7} dyn, (b) F = 1.86x10^{-7} dyn, and (c) F = 2.79x10^{-7} dyn. The black dots represent bubbles with velocities above the cutoffs indicated by the arrows on the corresponding histograms. Image sizes are all 1027x768 μm^2.

thresholding is adequate because a qualitative analysis suffices here. In these figures, the array moves via correlated displacement of groups of neighboring bubbles. The size of the displaced region increases with applied force. Much of the random bubble motion produced by ac agitation is suppressed by thresholding. In Fig. 4.8(a) the small high velocity tail in the distribution corresponds to one small cluster of bubbles as shown in the thresholded bubble array image. In Fig. 4.8(b) the force is larger, and the high velocity tail is bigger. This tail corresponds to the three clusters in the right image. In Fig. 4.8(c) the distribution is bimodal: the higher velocity peak in the velocity histogram corresponds to a single spatially correlated group of bubbles in the moving array.

From the images and histograms of the bubble velocities, it is clear that the motion is a collective phenomenon produced by correlated bubble displacements. These displacements are nonuniform across the array at a given time. The array motion is not simply a consequence of the random motion of individual bubbles because the velocity distribution becomes distinctly non-Gaussian. A more quantitative discussion of the dependence of the size of coherent bubble clusters on the applied force will be given later in Section 4.7.

4.6 Temporal Behavior of Bubble Transport

To observe temporal correlations of the bubble transport, we recorded a sequence of four time-resolved images of the bubble flow. The force was applied for a total of 24 minutes during which the array moved 4.6 μm. Figures 4.9(a) to 4.9(d) are velocity histograms for the four sequential 6-minute intervals and Fig. 4.9(e) is velocity histogram for the whole 24 minutes. The average array velocity during each succeeding 6-minute interval has similar value for all four intervals: $v = 0.0058 \pm 0.0004$ μm/sec. The solid curves are Gaussian fits to the peaks. The standard deviations of the Gaussian fits for Figs. 4.9(a) to 4.9(d) are set to the same value, and the standard deviation of the Gaussian

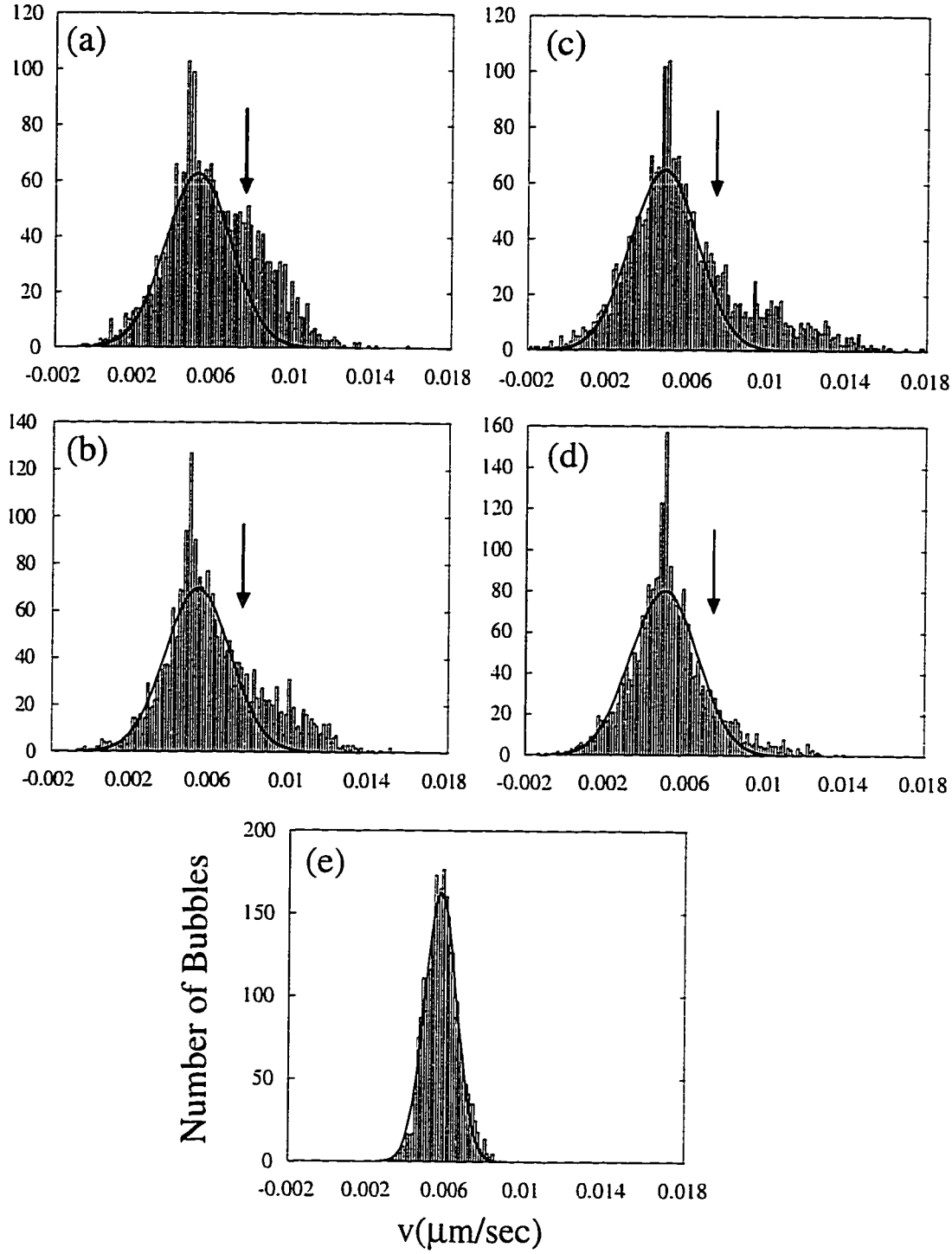

Fig. 4.9 Velocity histograms of the moving bubble array at H_{ac} = 10.1 Oe and F = 1.24x10^{-7} dyn. The solid curves are Gaussian fits to the peak. The arrows indicate the cutoff velocity 0.0075 μm/sec. (a)-(d) are averaged over 6 minutes in continuous sequence; (e) is averaged over 24 minutes.

fit for Fig. 4.9(e) is half of that for Figs. 4.9(a) to 4.9(d) as predicted by simple statistics. Figures 4.9(a) to 4.9(d) show that the instantaneous motion is non-Gaussian and a high velocity tail can be easily identified in each histogram. Figure 4.9(e) shows that the motion averaged over a longer time is much more uniform and the histogram is well fit by a Gaussian profile without a high velocity tail. This long time uniform motion indicates that the time averaged individual bubble velocity tends to be constant in all parts of the array. Theoretically it can be understood by applying the continuity equation for two-dimensional systems:

$$\frac{\partial \rho}{\partial t} + \nabla \bullet \bar{J} = 0, \tag{4.6.1}$$

where ρ is the bubble concentration and $\bar{J}$ corresponds to the instantaneous local velocity. We assume the velocity $\bar{J}$ is in the $+\hat{x}$ direction and choose a closed rectangular circuit on the bubble array. We use J_1 and J_2 to represent the velocities along the two sides perpendicular to the velocity, l_1 and l_2, where $l_1 = l_2$. The integral form of the continuity equation is

$$\frac{d}{dt}\iint_{Area} \rho dA + (J_1 l_1 - J_2 l_2) = 0. \tag{4.6.2}$$

Because the total number of bubbles within the closed circuit is a constant over time, the first term in Eqn. (4.6.2) is zero. Thus we have $J_1 = J_2$, indicating that the time averaged velocity is a constant at different parts of the array.

To understand microscopically how spatially nonuniform motion over the short times results a uniform flow over longer times in the bubble array, we examine the bubbles in the high velocity tails in Figs. 4.9(a) to 4.9(d) as below. Figures 4.10(a) to 4.10(d) are the thresholded images showing the location of bubbles in the high velocity tails,

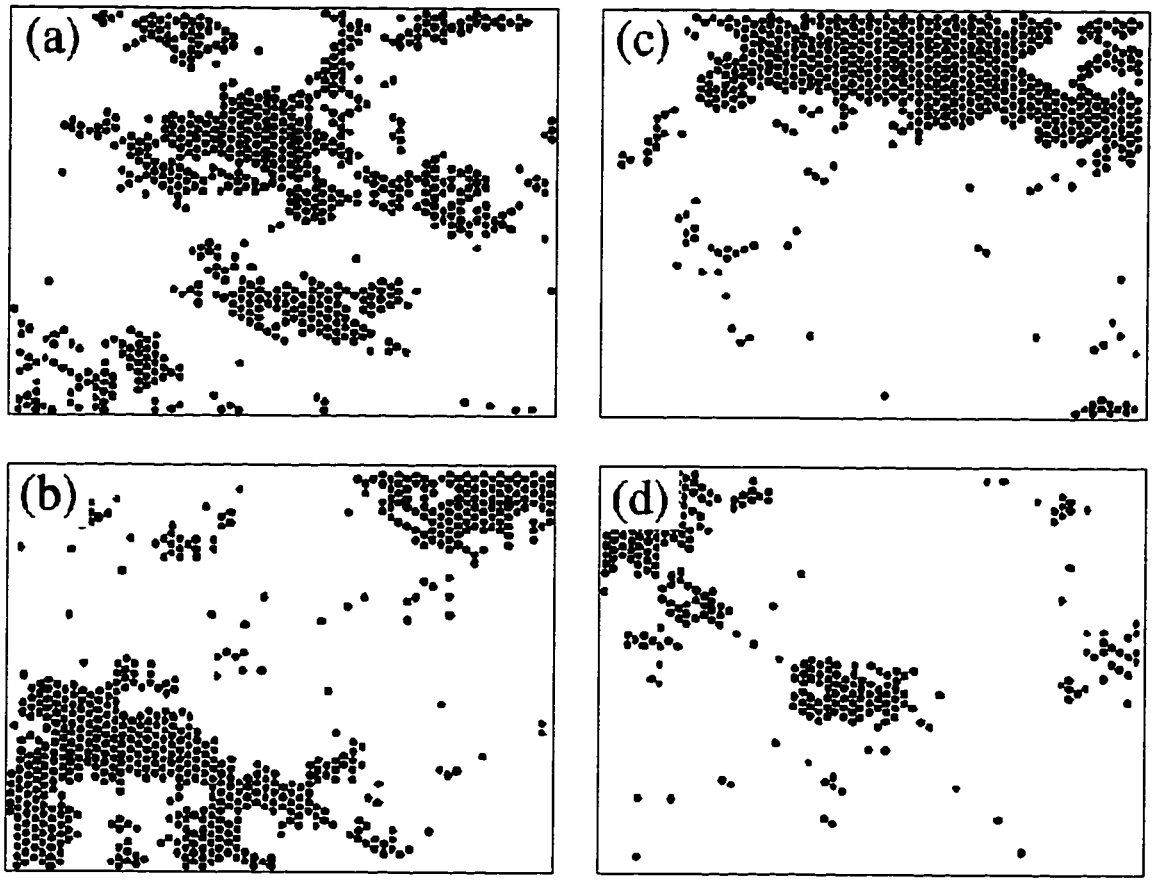

Fig. 4.10 Sequence of moving bubble images (1027x768 μm^2) for H_{ac} = 10.1 Oe and F = 1.24x10^{-7} dyn. The cutoff velocity is 0.0075 μm/sec. Each image is averaged over 6 minutes, corresponding to the velocity histogram shown in Figs. 4.9(a)-4.9(d).

corresponding to Figs. 4.9(a) to 4.9(d). These images are processed similarly as described in Section 4.5. The cutoff velocity, indicated by the arrows in Figs. 4.9(a) to 4.9(d), is 0.0075 μm/sec. It is interesting to see how bubble motion spreads through the array. Quickly moving clusters of bubbles in Fig. 4.10(a) exert stress on neighboring slowly moving parts of the array. This quickly moving part of the array changes in location and shape from frame to frame in Figs. 4.10(a) to 4.10(d) as the stress created by nonuniform motion is passed through the array, producing more uniform motion over longer time scales. Image analysis indicates that no creation or annihilation of dislocations occurs in Figs. 4.10(a) to 4.10(d), or in other typical data of similar conditions. The few dislocations present simply move with the array, therefore the elastic medium theory is applicable.

Höfelt [1973] studied the elastic wave phenomena in the bubble lattice under the influence of an external force. He obtained the velocities of propagation for deformation of a triangular magnetic bubble lattice, i.e. speeds of sound: the velocity of the longitudinal propagation $v_l = \sqrt{(\lambda + 2\mu)/\rho}$ and the velocity of the transverse propagation $v_t = \sqrt{\mu/\rho}$, where ρ is the effective mass density due to domain wall motion. For our bubble array $v_l \cong 3\text{x}10^4$ cm/sec and $v_t \cong 10^4$ cm/sec. These velocities is much greater than the average array velocity, indicating that the stress is passed through the array with velocities much faster than the array velocity. This type of bubble motion is analogous to sliding charge density wave transport [Fisher, 1984; 1987], for which it is also predicted that the velocity for wave propagation of deformations is much faster than array motion.

4.7 Velocity-Velocity Correlations

As discussed in the last two sections, the array motion is collective property of magnetic bubbles. Although the individual bubble velocities fluctuate, they are correlated over the velocity-velocity correlation length ξ_v, defined in Eqn. (4.2.4).

Figure 4.11 shows semi-log plots of the measured velocity-velocity correlation function $C(r_{ij})$ vs the bubble separation r_{ij} for five representative values of force (see caption). The velocities used are obtained at H_{ac} = 10.1 Oe and averaged over a 2-minute interval. As shown in the figure, $C(r_{ij})$ decays exponentially. The drop at large separations is due to finite image size. Figure 4.11 also shows that the magnitude of the slope decreases with increasing force, indicating that ξ_v increases with force at these five force values. Figure 4.12 shows the measured velocity-velocity correlation length ξ_v vs applied force F. The values of ξ_v were determined from data at small bubble separations using an exponential fit to $C(r_{ij})$ according to Eqn. (4.2.4). For a small applied force F, when the array velocity is small, the correlation length ξ_v is of the order of the lattice spacing a. The length ξ_v is associated with random bubble agitation by the ac field. It is easy to see from the figure that the velocity-velocity correlation length ξ_v increases monotonically with applied force. We do not observe a peak in ξ_v.

We are not able to obtain the Lee-Rice length and the threshold force, which are determined by the pinning strength, elastic constant, and bubble spacing according to Eqns. (4.2.5) and (4.2.6), because the pinning strength is difficult to measure.

4.8 Summary

In this chapter we have discussed our study of the collective transport phenomena of two-dimensional magnetic bubble arrays. The bubble array used for detailed spatiotemporal study of the transport is defect free over the field of view and no creation and annihilation of dislocations occurs during transport. The velocity-force responses at various ac magnetic fields agree with transport theory for two-dimensional elastic media [Batrouni and Hwa, 1994; Carraro and Nelson, 1996]: $v \propto F^{\alpha}$, with $\alpha \cong 3$. A similar α at different ac fields is understandable because the effective temperature for those ac fields, characterized by $\sigma/a = 0.039 \pm 0.004$, are similar. Compared with Lindemann

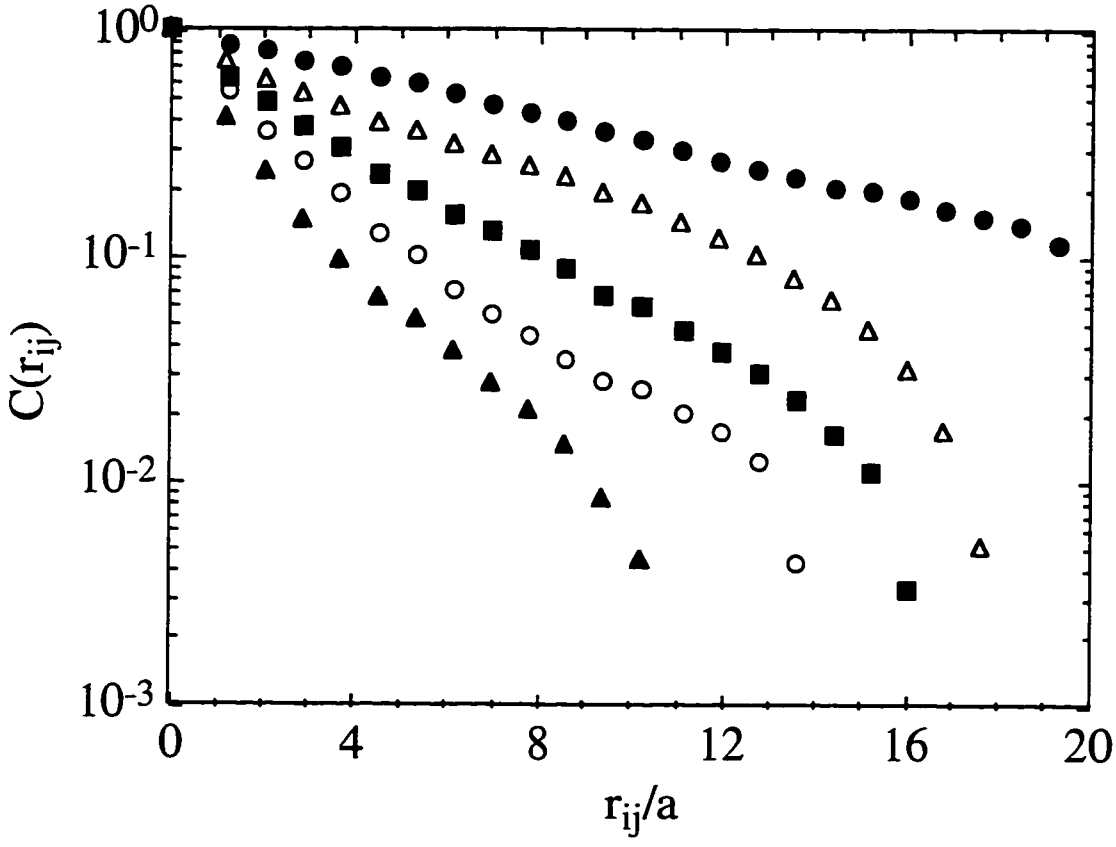

Fig. 4.11 The velocity-velocity correlation function $C(r_{ij})$ vs bubble separation r_{ij} at forces $F = 2.79 \times 10^{-7}$ dyn (black dots), 1.86×10^{-7} dyn (open triangles), 1.24×10^{-7} dyn (black squares), 0.93×10^{-7} dyn (open circles), and 0.46×10^{-7} dyn (black triangles).

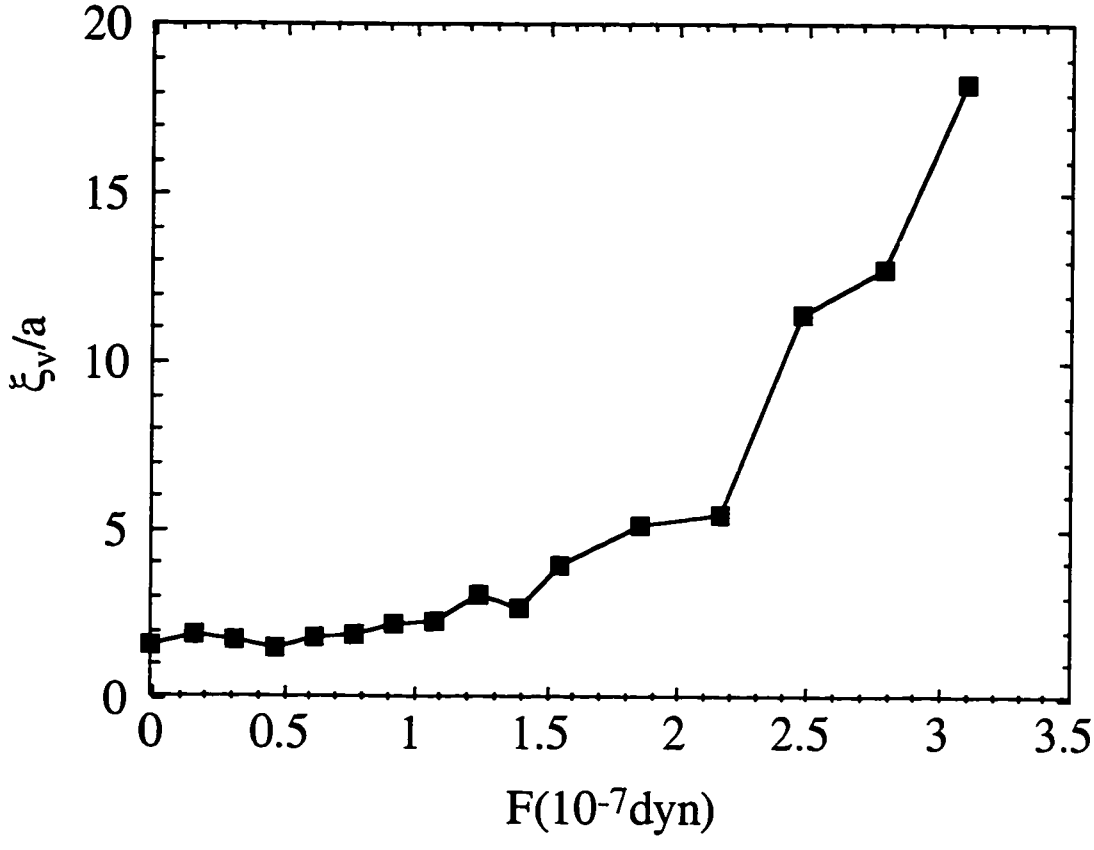

Fig. 4.12 Velocity-velocity correlation length ξ_v vs applied force F at H_{ac} = 10.1 Oe.

criterion, the array is well below the melting temperature. This explains why there is no creation and annihilation of dislocations in a defect free area during transport and why existing dislocations are frozen in the moving array. The collective nature of the transport is clearly demonstrated in the images of bubble velocity distribution: bubbles move forward via correlated bubble clusters rather than individual bubbles. Subsequent bubble array images and corresponding velocity histograms show that although there are spatial and temporal fluctuations in the instantaneous velocity, the time averaged velocity remains constant over the sample area. Spatiotemporal observation of bubble transport also examines the microscopic origins for friction and drag in the system: the weak random pinning due to substrate roughness. The measured velocity-velocity correlation length increases monotonically with applied force.

Through the transport experiment of two-dimensional magnetic bubble arrays we have investigated the dynamic response of a two-dimensional system with weak random pinning to a uniform applied force. Direct spatiotemporal observation of driven bubble motion provides microscopic pictures of the collective transport. The bubble system is similar to many other systems in terms of interaction, pinning, and driving force. Results from the magnetic bubble system allows us to compare with current collective transport theory and help draw possible microscopic picture of motion for systems that are difficult to observe directly.

CHAPTER 5 COMMENSURATE-INCOMMENSURATE TRANSITIONS IN MAGNETIC BUBBLE ARRAYS WITH PERIODIC LINE PINNING

In this chapter we present microscopic observations of commensurate (C) - incommensurate (I) phase transitions which occur as the bubble concentration is varied in two-dimensional magnetic bubble arrays subject to periodic line pinning. The pinning lines consist of parallel permalloy bars lithographically fabricated on top of the garnet film. Two different pinning periodicities are used. At the long pinning periodicity we have identified an incommensurate polycrystalline phase and a commensurate smectic phase. At the short pinning periodicity which also has a weaker pinning strength, we have observed a even-odd symmetry breaking phase where the symmetry between even and odd numbered pinning lines is broken. For both pinning periodicities the structure function shows a smooth migration of Bragg peaks as the bubble concentration decreases. This indicates a second order (or weakly first order) commensurate-incommensurate-commensurate transition. This phase transition takes place via continuous rotation of the array orientations.

This chapter is organized as follows. In Section 5.1 we review the background and the motivation for our C-I transition experiment. In Section 5.2 we introduce the concept of commensurability and review theories of C-I transitions. In Section 5.3 we describe the experimental procedure. In Sections 5.4 to 5.6 observations on samples with a long pinning periodicity and moderate pinning strength are presented. In Section 5.4 we discuss the identification of the commensurate and incommensurate phases occurring during the C-I-C transition from the bubble array images and their corresponding structure functions. In Section 5.5 we discuss the nature of the C-I-C transition by examination of the migrating

peaks in structure function plots. In Section 5.6 we show how the translational orders of the bubble array evolve with bubble concentration. In Sections 5.7 and 5.8 results from samples with a short pinning periodicity and weak pinning strength are presented. In Section 5.7 we show how an even-odd symmetry breaking phase occurs as the bubble concentration reduces. In Section 5.8 we discuss the C-I-C transition at this new pinning condition and compare it with the case at long period pinning condition. We also compare our results with isotropic melting in the bubble arrays. In Section 5.9 we summarize the major results of this experiment.

5.1 Introduction

A system subject to a periodic pinning potential often demonstrates commensurate and incommensurate phases. When the density or temperature of such a system changes, the system commonly undergoes phase transitions between commensurate and incommensurate phases as a result of competition between internal interactions, thermal energy, and the external pinning strength. Theoretical and experimental investigations of commensurability effects and C-I phase transitions have been carried out since the late 1970s, and a variety of physical systems with different periodic pinning structures have been studied. The structural characteristics of monolayers of krypton adsorbed on graphite as well as the critical behavior of its C-I transition have attracted considerable theoretical attention [Pokrovskii and Talapov, 1978; Pokrovsky and Talapov, 1979; Schulz, 1980; Villain, 1980; Coppersmith *et al.*, 1981; 1982]. Burkov and Pokrovsky [1980 and 1981] postulated that the behavior of the critical current of a thin thickness modulated superconducting film [Martinoli *et al.*, 1974; Daldini *et al.*, 1981] can be understood from the standpoint of two-dimensional C-I transitions. Balents and Simon [1995a] predicted that commensurability effects in large Josephson junctions with periodic defects are

equivalent to those of defect-free junctions near zero field. Their prediction has been confirmed experimentally by Itzler and Tinkham [1995a and 1995b]. Ivlev, Kopnin, and Pokrovsky [1990] and Levitov [1991] investigated the possible structures of a vortex lattice in strong layered superconductors with the magnetic field parallel to the layers. Balents and Nelson [1994; 1995] investigated the C-I phase transitions of vortex arrays in layered superconductors when the pinning is weak and postulated that a flux liquid can freeze into a smectic phase. It is of considerable theoretical and experimental interest to understand how C-I transitions take place and to determine the order of the phase transitions in an experimental system. The nature of the C-I transitions is interesting not only in its own right because of the presence of novel structured phases but also because these transitions are important to the transport properties of these materials.

The magnetic bubble system is an excellent experimental system to study C-I transitions because we can introduce artificial pinning of desired geometry and controllable pinning strength. In addition, the computer-video techniques described in Chapter 3 allow us to observe directly how C-I phase transitions take place in real time. It is our hope that direct observation and understanding of C-I phase transitions in the magnetic bubble system will serve as a bridge between theoretical predictions and experimental results and provide detailed microscopic picture for future theoretical work.

5.2 Theory of Commensurate-Incommensurate Transitions

Figure 5.1 illustrates commensurate and incommensurate bubble arrays with periodic line pinning. We choose the pinning line direction as the $\hat{x}$ direction and the perpendicular direction as the $\hat{z}$ direction. The concept of commensurability is relevant for periodically structured systems in periodic media. As shown in the figure, a magnetic bubble array with periodic line pinning is such a system. If the period of the bubble row spacing is a_{row} and the period of the pinning lines is the spacing p between the centers of two adjacent

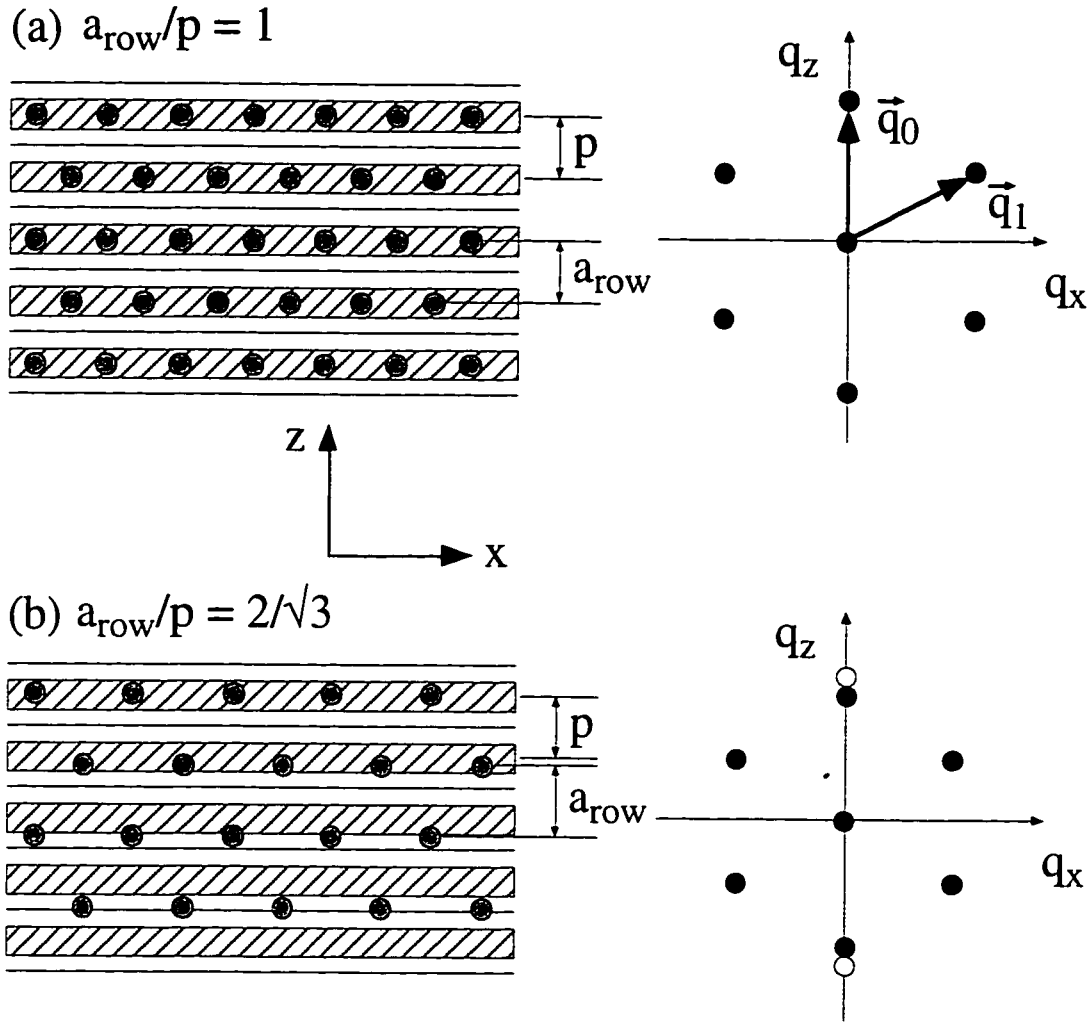

Fig. 5.1 Schematic illustration of bubble arrays and corresponding structure functions in the (a) commensurate and (b) incommensurate phases. The hatched areas are the pinning lines and the solid lines are boundaries separating neighboring pinned regions. The open circles in the structure function plot in (b) indicate the location of the reciprocal lattice vectors of the periodic pinning lines.

lines, then the system is in a commensurate (or in-registry) phase when the ratio a_{row}/p is a rational number, as for the array shown on the left of Fig. 5.1(a); the system is in an incommensurate (or out-of-registry) phase when a_{row}/p is an irrational number, as for the array shown on the left of Fig. 5.1(b). We can determine the commensurability of a system by direct observation of the array and the periodic pinning lines.

In addition to direct observation, we can also determine the commensurability of a system and identify the crystal structure of the commensurate and incommensurate phases using structure function analysis. The structure function can be introduced as follows. We define a bubble concentration function for a two-dimensional magnetic bubble array as

$$\rho(\vec{r}) = \sum_{j=1}^{N} \delta\left(\vec{r} - \vec{r}_j\right), \qquad \text{with} \quad \int_{\text{Area}} \rho(\vec{r}) dA = N, \tag{5.2.1}$$

where $\vec{r}_j$ is the position of the jth bubble center and N is the total number of bubbles over the field of view. The Fourier transform of $\rho(\vec{r})$ is:

$$\rho(\vec{q}) = \sum_{j=1}^{N} e^{i\vec{q}\bullet\vec{r}_j}. \tag{5.2.2}$$

The structure function is then defined as [Nelson, Rubinstein, and Spaepen, 1982]

$$S(\vec{q}) = \left|\rho(\vec{q})\right|^2. \tag{5.2.3}$$

On the right of Fig. 5.1 are the structure functions for the two bubble arrays shown on the left of this figure. There are six symmetric peaks on these structure function plots, indicated by the six solid dots. These peaks arise from the six-fold symmetry of the triangular bubble array. Comparison of the peak locations of $S(\vec{q})$ on q_z axis with the peak locations of the reciprocal lattice vectors of the periodic pinning lines tells us whether the

array is commensurate or incommensurate. The reciprocal lattice vectors of the periodic pinning are a series of periodic one-dimensional sharp peaks on q_z axis with periodicity $2\pi/p$. The reciprocal lattice vectors of the bubble array are a series of periodic peaks on q_z axis with periodicity $2\pi/a_{row}$. When the array is commensurate, there is a periodic overlap of the two sets of peaks. For example in Fig. 5.1(a), $a_{row}/p = 1$, and the two sets of peaks along q_z axis overlap completely. When the array is incommensurate, the two sets of peaks do not overlap and the relative location of the two sets of peaks is not periodic, as shown on the right of Fig. 5.1(b), where the empty circles are from pinning lines. The other peaks which are not on q_z axis, referred to as off-axis peaks in the rest of this chapter, tell us the structural order of the array: the location of the off-axis peaks reveals the crystal structure of the array and the sharpness of the off-axis peaks reveals the degree of order of the array.

Commensurate-incommensurate transitions often take place in a weakly pinned system when the density or temperature of the system changes. For weak pinning an object can move across the pinning sites under forces applied by the array internally. As the density or temperature of the system changes, the relative strength of the pinning energy, thermal energy, and object-object interaction will also change. As a result the system will rearrange its structure to minimize its total energy, thereby leading to a series of C-I phase transitions. Because periodic pinning introduces an additional broken symmetry to the system, a number of new phases are likely to appear during the C-I transitions. Though a theoretical phase diagram for the bubble array with periodic line pinning has not been computed, theoretical phase diagrams for similar systems have been proposed. Balents and Nelson [1994; 1995] postulated that in layered superconductors the system will freeze into an intermediate "smectic" phase between the flux liquid (high temperature) and crystal / glass (low temperature) phases. At intermediate temperatures, the flux lines are easier to move within the region between two layers than across layers, so the flux lattice melts in the direction parallel to the layers while order persists in the perpendicular direction

to form a smectic phase. Coppersmith *et al.* [1981; 1982] proposed that in monolayer krypton adsorbed on graphite a fluid phase is expected between the commensurate and incommensurate solid phases as the surface density of krypton atoms increases. When the array periodicity is much longer than the pinning periodicity, a symmetry breaking phase is expected where a periodic subset of the pinning lines are occupied by the bubbles [Balents and Nelson, 1994; 1995].

For a strongly pinned system, the objects are confined to their original pinning sites and do not cross over to their neighboring pinning sites under internally applied forces. Commensurate-incommensurate transitions do not occur in such systems, which remain commensurate. New types of crystal structures can form in strongly pinned arrays by changing the spacing between objects along the pinning direction [Ivlev, Kopnin, and Pokrovsky, 1990; Levitov, 1991].

To characterize the structural order of the commensurate or incommensurate bubble arrays, we define a structural translational order parameter

$$\rho_S\left(x_j, z_j\right) = \exp\left(i\vec{q}_l \bullet \vec{r}_j\right), \tag{5.2.4}$$

where $\vec{r}_j = (x_j, z_j)$ is the coordinate of the jth bubble and $\vec{q}_l$ represents the off-axis reciprocal lattice vector of the array. There are total four off-axis reciprocal lattice vectors for a triangular bubble array. Based on $\rho_S(x_j, z_j)$, a structural translational correlation function $C_{T,S}(\Delta x, \Delta z)$ can be defined as [Balents and Nelson, 1995]:

$$C_{T,S}(\Delta x, \Delta z) = \left\langle \rho_S(x_i, z_i)\rho_S^*\left(x_j, z_j\right)\right\rangle, \tag{5.2.5}$$

where $\Delta x = |x_i - x_j|$ and $\Delta z = |z_i - z_j|$ are the bubble separations along and perpendicular to the pinning line direction. The angular brackets indicate an average over all pairs of bubbles separated by $(\Delta x, \Delta z)$. The function $C_{T,S}(\Delta x, \Delta z)$ characterizes correlations of the

structural order, similar to $G_T(r_{ij})$ defined in Eqn. (4.3.1): the value $C_{T.S}(\Delta x, \Delta z) = 1$ means that the array is a perfect crystal and the value $C_{T.S}(\Delta x, \Delta z) = 0$ means that array is completely disordered.

A commensuration translational order parameter $\rho_C(x_j, z_j)$ is defined associated with the reciprocal lattice vectors of the periodic pinning lines:

$$\rho_C(x_j, z_j) = \exp(i\vec{q}_0 \bullet \vec{r}_j), \tag{5.2.6}$$

where $\vec{q}_0$ is the smallest reciprocal lattice vector on the q_z axis arising from the periodic subset of the pinning lines occupied by bubbles. This order parameter measures the deviation of a bubble from the center of an occupied pinning line. Based on $\rho_C(x_j, z_j)$, a commensurability translation correlation function can be defined as [Balents and Nelson, 1995]:

$$C_{T.C}(\Delta x, \Delta z) = \langle \rho_C(x_i, z_i) \rho_C^*(x_j, z_j) \rangle, \tag{5.2.7}$$

where the angular brackets represent an average over all pairs of bubbles separated by $(\Delta x, \Delta z)$.

5.3 Experimental Method

Periodic pinning lines are provided by an array of parallel permalloy bars fabricated on top of the bubble film. Figure 5.2(a) illustrates a cross section of a garnet sample. The middle layer with arrows is the garnet film. The bottom hatched layer is the substrate. The dark rectangles on the top of the garnet film represent the cross section of a periodic array of permalloy bars which pin bubbles. In our experiment, each permalloy bar is 6 μm wide. These pinning lines cover the bubble array over an area 1 cm x 1 cm. Two pinning

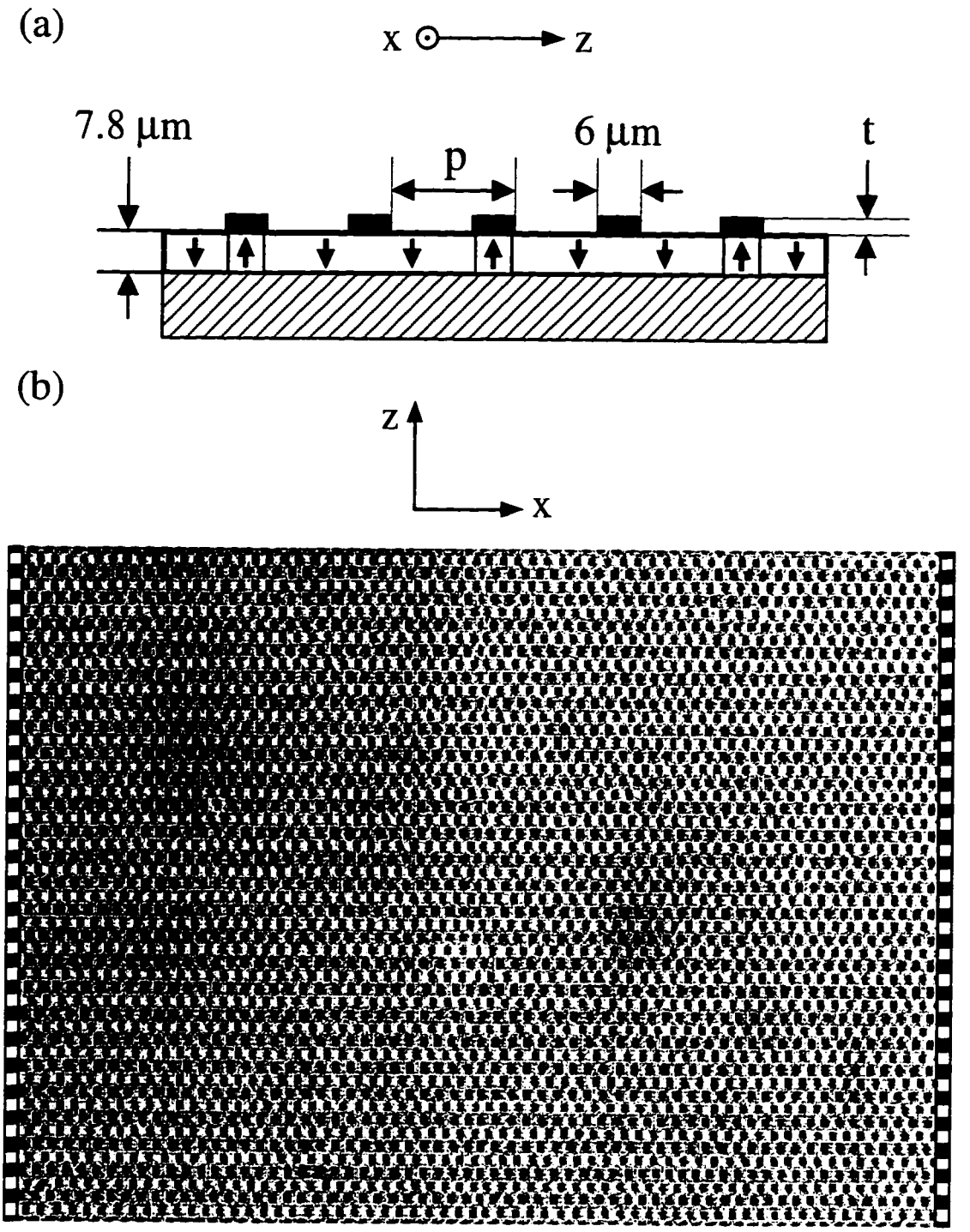

Fig. 5.2 (a) Schematic cross section of garnet sample: the white layer indicates the garnet with magnetic bubble domains indicated by up arrows; the gray rectangles indicate the cross section of a periodic array of permalloy lines on the film surface, which pin bubbles; the hatched layer indicates the substrate. (b) Bubble array image visualized in an optical microscope via the Faraday rotation, size 705 µm x 517 µm. The black squares on the left and right sides represent pinned rows of bubbles; the white squares represent unpinned rows.

periodicities have been investigated: p = 20 μm and p = 10 μm. For each periodicity C-I transitions have been observed at a number of permalloy thicknesses. Final data were taken on samples with thickness t = 51 Å for p = 20 μm and t = 37 Å for p = 10 μm. The pinning strength is moderate for the former set of parameters to weak for the latter set of parameters: bubbles move across pinning lines during annealing at incommensurate bubble concentrations. In addition to the line pinning, there is a weak random point-like pinning due to substrate roughness described above in Chapter 2.

In our experiment we study the C-I phase transitions by recording bubble array images with fixed bubble agitation for a series of decreasing bubble concentration as follows. The effective temperature is generated by an ac magnetic field H_{ac} of fixed frequency 40 Hz. The bubble concentration ρ is reduced by increasing the external perpendicular bias field H_B in small steps. After each increment of H_B, the array is first annealed at H_{ac} = 20.7 Oe for 30 minutes, and then further annealed at a lower H_{ac} = 13.6 Oe for 15 minutes.

All images used for analyses are taken at this low ac field to minimize thermal fluctuations. Figure 5.2(b) is a grayscale image taken from the long periodicity pinning sample with t = 51 Å and p = 20 μm. It shows a commensurately pinned bubble array with every other row of bubbles pinned by the permalloy bars. The locations of the permalloy bars are indicated by black blocks in the vertical strips on the left and right side of the image. The white blocks in the bars indicate the locations of unpinned rows. Periodic parallel pinning produces a triangular bubble array for this example with nearest neighbors oriented along the pinning line direction $\hat{x}$ as shown in the figure. It is worth pointing out that due to the periodic parallel line pinning, the single crystal triangular array extends over the entire area covered by pinning lines and contains over 800,000 bubbles at high bubble concentration. The size of this single crystal array is much larger than would occur without periodic line pinning.

5.4 Overview of Commensurate-Incommensurate Transitions

In this and the following two sections we present our observations of the C-I-C transition as a function of bubble concentration ρ in the magnetic bubble array subject to periodic line pinning with long periodicity $p = 20\ \mu m$ and $t = 51$ Å. The initial bubble array at high bubble concentration is a commensurate triangular array with every other row of bubbles pinned. Figure 5.3 shows how the number of bubbles per row (bubble row concentration) responds to a reduction in bubble concentration in the pinned and unpinned rows. As shown for $\rho > 7000\ mm^{-2}$, the reduction in bubbles per row is the same for pinned and unpinned rows. This occurs because the bubble-bubble interaction energy is stronger than the pinning energy: the role of pinning lines in minimizing the total energy is to provide a preferred array orientation rather than making a bubble row concentration difference between the pinned and unpinned rows. For $3000\ mm^{-2} < \rho \leq 7000\ mm^{-2}$, the bubble row concentration for the unpinned rows decreases much faster than that for the pinned rows. This difference between the pinned and unpinned rows arises from the reduction in the bubble-bubble interaction with increased spacing: some bubbles move from unpinned rows to the neighboring pinned rows to minimize the total energy. As shown in Fig. 5.3, all bubbles in the unpinned rows have collapsed for $\rho \leq 3000\ mm^{-2}$. For smaller ρ, reductions in bubble concentration are realized by taking bubbles from the pinned rows.

Figure 5.4 is a series of bubble array images taken as the bubble concentration changes. The average bubble concentrations ρ (bubbles/mm^2) are shown on the top left of each image in Fig. 5.4. The images are ordered from the highest bubble concentration on the top left to the lowest bubble concentration on the bottom right. Only part of the digitized array is shown. Topological defects are identified using Voronoi constructions and plotted on these images to illustrate the microscopic nature of array during the C-I phase transitions. A dislocation is a bound pair of a five-fold and a seven-fold disclination.

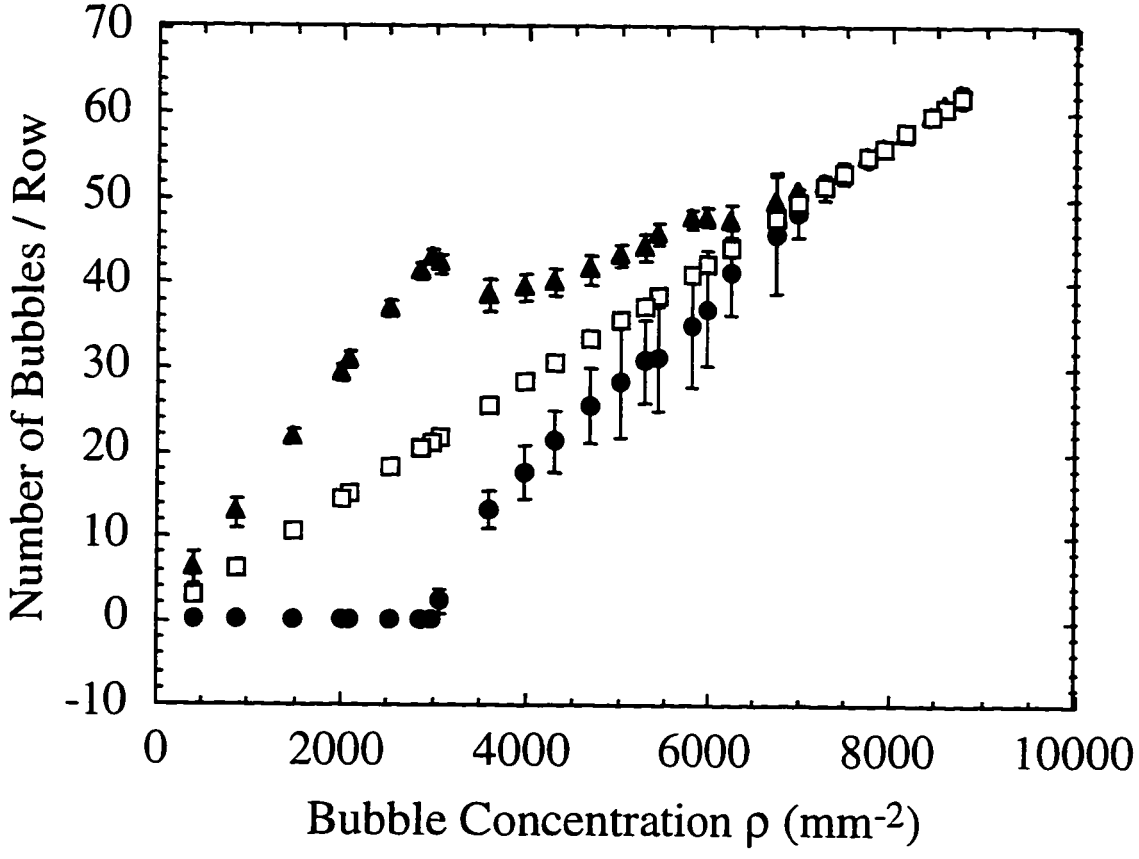

Fig. 5.3 Average bubble row concentration vs bubble concentration ρ. Black triangles represent average bubble row concentration for the pinned rows; black circles represent average bubble row concentration for the unpinned rows; open squares represent bubble row concentration averaged over all bubbles, regardless of pinning condition. The error bars are standard deviations of the number of bubbles per row.

The direction of a dislocation is normally represented using a Burgers vector which is a vector required to complete a circuit passing around the dislocation and through dislocation-free parts of the array [Hull and Bacon, 1984]. In two-dimensional triangular arrays, the Burgers vector is always perpendicular to the line connecting the five-seven pair. Figures 5.5(a) to 5.5(i) are plots of the structure functions $S(\vec{q})$ corresponding to Figs. 5.4(a) to 5.4(i). The structure functions are computed over the entire imaged area of 705 μm x 517 μm. A Hanning window with cylindrical symmetry is applied to the bubble center data in order to reduce the amplitude of possible spurious features.

Using Figures 5.4 and 5.5 together, we can identify the commensurate and incommensurate phases which occur as the bubble concentration is reduced and study the pathway by which these phase transitions take place. We start with the high concentration commensurate phase. As shown in Fig. 5.4(a), at high bubble concentration ρ the average bubble row spacing is about 10 μm, half of the pinning periodicity. The resulting bubble array is a commensurate triangular array with two rows of bubbles per pinning line: one pinned row and one unpinned row. The nearest neighbor bond is along the pinning line direction $\hat{x}$. The word "bond" refers to the line connecting adjacent bubbles determined using Voronoi constructions. There are few dislocations which are far away from each other, with only one present in Fig. 5.4(a). All dislocations have their Burgers vectors in the $\hat{x}$ direction: this orientation minimizes their interaction with the pinning potential because dislocations with Burgers vectors along other directions would be accompanied by missing rows of bubbles in the pinning direction. The corresponding structure factor $S(\vec{q})$ in Fig. 5.5(a) has two sharp peaks at $q_z = \pm 4\pi/p$, indicating a commensurate array. The off-axis peaks are broadened somewhat by random substrate disorder. These peaks have Lorentzian shapes, indicating a short translational order. The four off-axis peaks along with two peaks on q_z axis suggest a quasi-long range orientational order. We refer to this phase as a dislocated triangular array. Such systems are also often referred to as hexatics [Nelson and Halperin, 1979; Seshadri and Westervelt, 1991; Grier *et al.*, 1991; Imry and

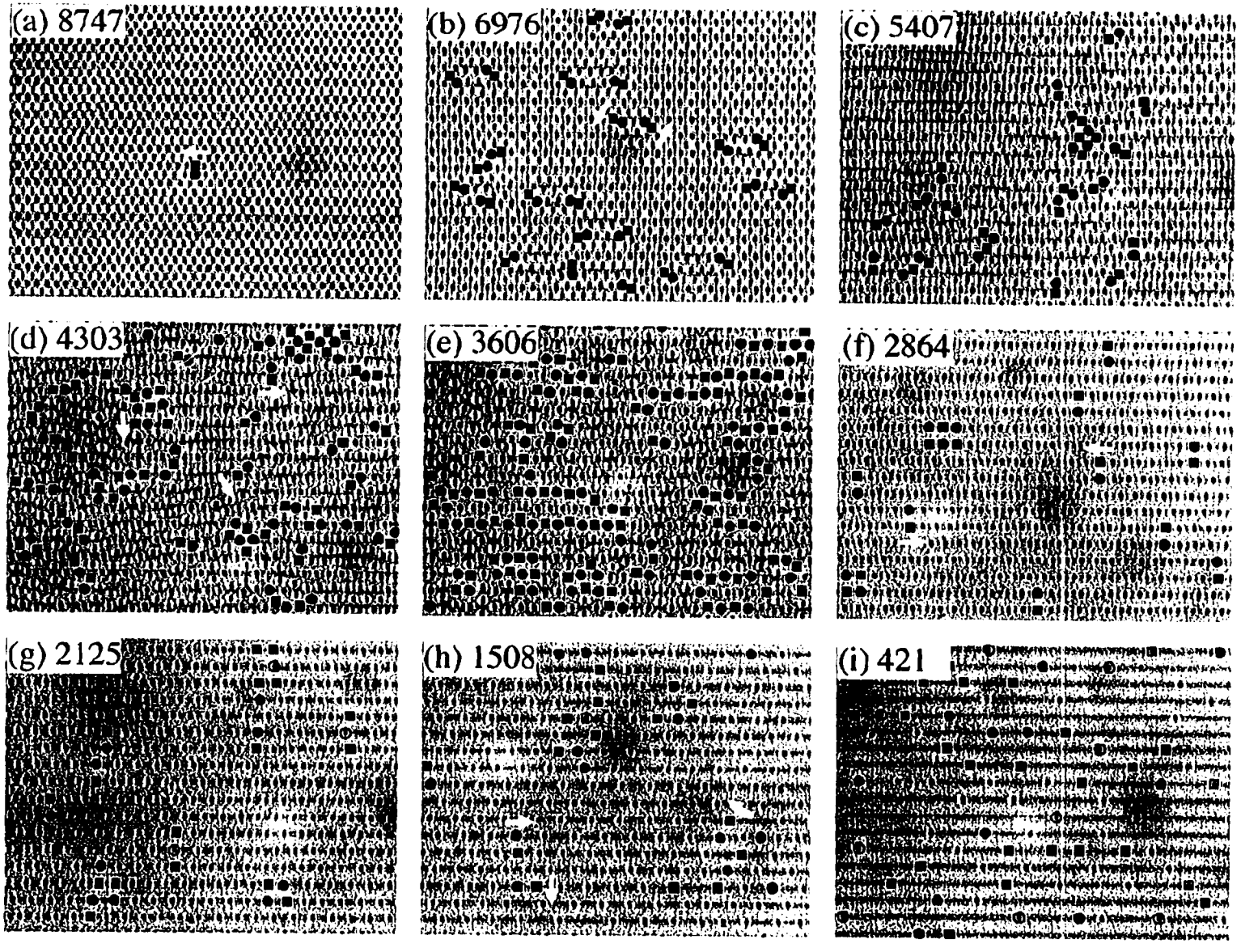
(a) 8747
(b) 6976
(c) 5407
(d) 4303
(e) 3606
(f) 2864
(g) 2125
(h) 1508
(i) 421

Fig. 5.4 Overview of C-I transitions in real space as the bubble concentration ρ is reduced; ρ (mm^{-2}) is indicated on the top left of each 410 μm x 351 μm image. Black squares, black circles, open squares, and open circles represent topological defects: 5-fold, 7-fold, < 5-fold, and > 7-fold disclinations respectively. A bound 5-fold and 7-fold pair of disclinations is a dislocation. The white arrows indicate the direction of the Burgers vectors.

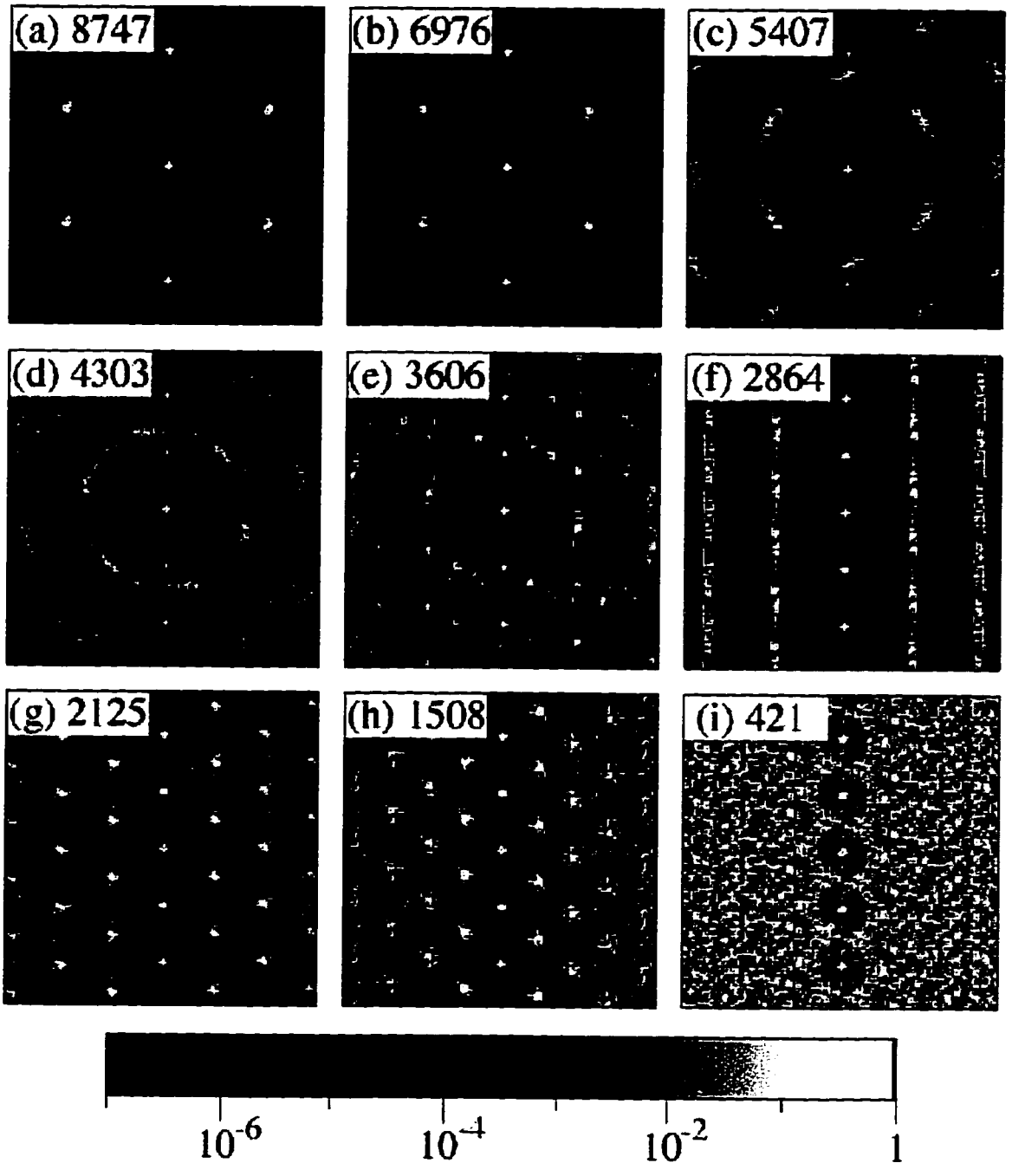

Fig. 5.5(color) Structure functions $S(\vec{q})$ computed from bubble center locations correponding to Figs. 5.4(a) to 5.4(i) showing C-I transitions. The origin at $q = 0$ is at the center of each image; the pinning lines are parallel to the horizontal q_x axis; the q_z axis is vertical.

Ma, 1975]. The two fuzzy vertical stripes in Fig. 5.5(a) can be ignored because their intensity is ~ 10^{-4} smaller than the intensity at the center of the peaks. Observations of the annealing process in samples with and without line pinning indicate that the pinning stabilizes orientational order as one would expect from theory [Burkov and Pokrovskii, 1980; Burkov and Pokrovsky, 1981; Balents and Nelson, 1994; 1995].

As the bubble concentration is reduced from $\rho = 8747$ mm^{-2} to 7277 mm^{-2}, not shown in Figs. 5.4 and 5.5, the bubble array remains a commensurate array. The reduction in ρ is achieved by uniform collapse of bubbles in both pinned and unpinned rows. The bubble array is stretched and slightly sheared along the $\hat{x}$ direction as follows: the $\hat{x}$ components q_x of the off-axis peaks of the structure function decrease while the $\hat{z}$ components q_z shift slightly with the width of the peaks constant. A uniaxial strain in the pinning direction $\hat{x}$ results from the competition between the pinning potential and reduced bubble-bubble interaction [Burkov and Pokrovsky, 1981; Ivlev, Kopnin, and Pokrovsky, 1990]. The dislocation concentration increases only slightly. The dislocations in this regime are isolated and have horizontal Burgers vectors.

Figures 5.4(b) to 5.4(d) and Figures 5.5(b) to 5.5(d) show how the bubble array makes the transition from a commensurate triangular array to an incommensurate polycrystalline phase as the bubble concentration is reduced. In this regime, bubbles are seen to move from unpinned rows to neighboring pinned rows during annealing, and the average number of bubbles per row in the unpinned rows decreases faster than that in the pinned rows. In addition, some bubbles are no longer positioned at the center of the pinning lines. These phenomena happen because the interaction potential ($1/r^3$) decreases sharply as ρ decreases. As shown in Fig. 5.4(b) the reduction in bubble concentration is accomplished by the removal of partial rows of unpinned bubbles as indicated by pairs of dislocations with antiparallel Burgers vectors oriented $\pi/3$ radians from the pinning lines. As the bubble concentration is reduced further in Figs. 5.4(c) and 5.4(d), the array rotates locally to form a polycrystalline triangular array, and the dislocations group together to

form grain boundaries. The structure factor in Fig. 5.5(b) develops a new diffuse peak located along the $\hat{z}$ axis with wavevector q_z below the pinning wavevector $4\pi/p$. The wavevector of this diffuse peak decreases with bubble concentration and the peak broadens in the angular direction to form a ring for the polycrystalline array in Fig. 5.5(d). As shown in Fig. 5.4(d), this incommensurate polycrystalline phase has substantial disorder. A disordered incommensurate phase has also been observed in monolayer krypton adsorbed on graphite by Moncton, *et al.* [1981] using synchrotron x-ray scattering method.

A commensurate smectic phase forms as the bubble concentration is reduced further as shown in Figs. 5.4(e) and 5.4(f). The periodicity of the sharp peaks along q_z axis in Fig. 5.5(f) is half of that in Fig. 5.5(a), in agreement with direct observation of array images: the array in Fig. 5.4(f) is a new commensurate phase with one row of bubbles per pinning line. The smectic phase is characterized by order along $\hat{x}$ but disorder along $\hat{z}$ as demonstrated by a series of diffuse vertical stripes in the structure factor plot in Fig. 5.5(f): the bubbles in each pinned row form a periodic one-dimensional array, but the phases of these one-dimensional arrays in different rows are not well correlated. For the smectic phase shown in Fig. 5.4(f), the relatively few dislocations present have Burgers vectors oriented parallel to the $\hat{x}$ direction, otherwise the missing rows would be parallel to the pinning lines.

A transition from a commensurate smectic array to a commensurate triangular array occurs as the bubble concentration continues to decrease, as shown in Figs. 5.4(g) and 5.4(h). In the smectic phase in Fig. 5.4(f), bubbles are compressed in rows along the pinning lines. As the concentration is reduced, the bubble spacing within rows approaches the spacing appropriate for a commensurate triangular array in Fig. 5.4(g), then exceeds this spacing in Fig. 5.4(h) as the commensurate array is stretched along the $\hat{x}$ direction. In both Figs. 5.4(g) and 5.4(h) the array continues to show disorder in the alignment of pinned rows of bubbles. The peaks in the structure factor plot in Fig. 5.5(g) corresponds to the commensurate triangular array and the diffuse stripes correspond to the disorder in

row alignment. In Fig. 5.4(h) the dislocations no longer have a preferred direction, and the disordered background in the structure factor is diffuse. Comparing the commensurately pinned triangular arrays in Figs. 5.5(h) and 5.5(a), we can see that the low concentration triangular array in Fig. 5.5(h) possesses twice the bubble spacing and broader off-axis peaks.

Finally, as shown in Figs. 5.4(i) and 5.5(i), as the bubble concentration is reduced further to $\rho = 421$ mm^{-2}, the array melts into a modulated liquid: the dislocations unbind into isolated disclinations (Fig. 5.4(i)), and the structure function (Fig. 5.5(i)) becomes a superposition of a diffuse background and sharp peaks at $q_z = \pm 2\pi/p$ and $\pm 4\pi/p$ along the $\hat{z}$ axis due to the pinning potential.

A phase diagram summarizing our observations is presented in Fig. 5.6. At high bubble concentration, the array is a commensurate dislocated triangular array. As ρ decreases, internal stresses are created in the array and force the orientation of the triangular lattice to rotate locally, leading to an incommensurate polycrystalline phase. Upon continuing decrease of the bubble concentration, the array first forms a commensurate smectic phase, which is ordered in the pinning direction but disordered in the perpendicular direction, then forms a new commensurate dislocated triangular array with approximately twice the bubble spacing of the previous triangular array, and finally melts into a modulated liquid phase.

5.5 Nature of Commensurate-Incommensurate-Commensurate Transition

In this section we use structure function analyses to examine the nature of the phase transitions between the high concentration commensurate triangular array in Fig. 5.5(a) and the commensurate smectic phase in Fig. 5.5(f). As discussed in the previous section, a diffuse peak is developed along the q_z axis in the structure function at incommensurate

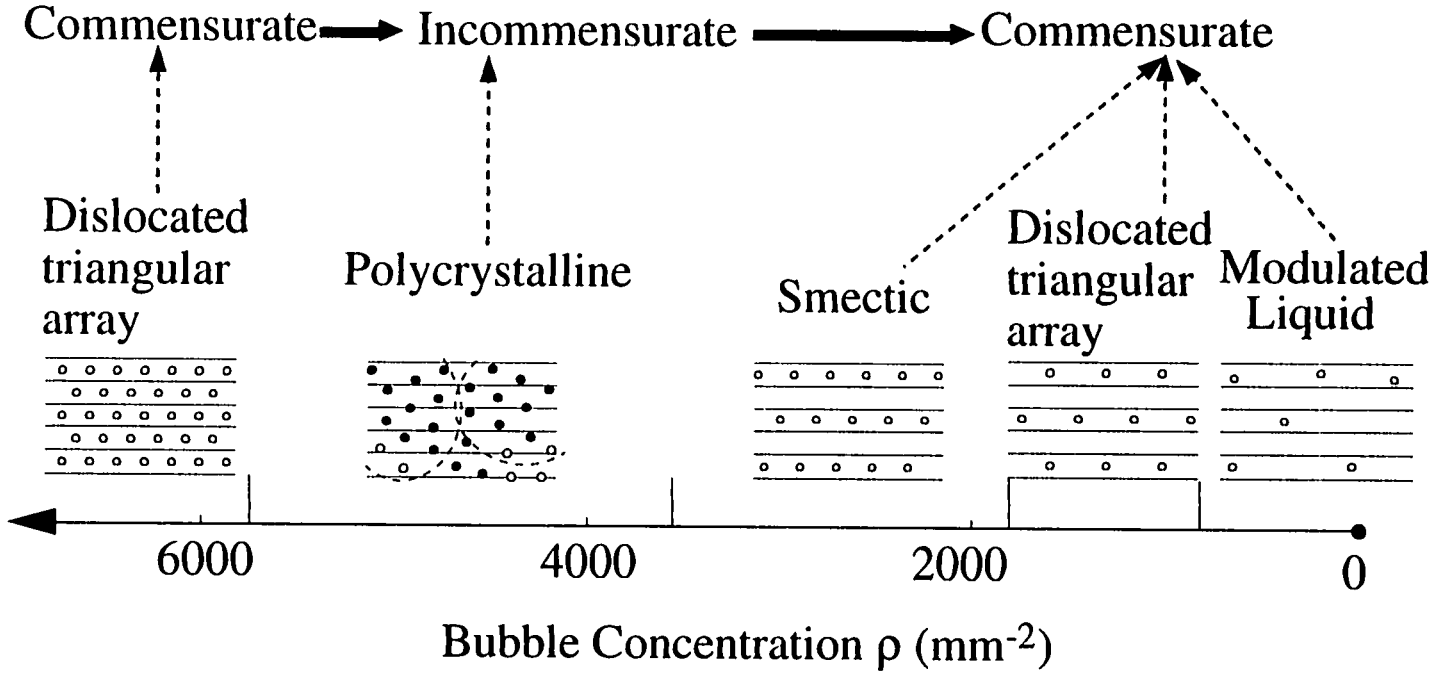

Fig. 5.6 Phase diagram for bubble arrays with periodic pinning with p = 20 μm and t = 51 Å. The dashed lines with arrows point to whether the phase is a commensurate or an incommensurate phase.

bubble concentrations. From Figs. 5.5(b) to 5.5(e), the diffuse peak decreases from the first commensurate peak $q_z = 4\pi/p$ to the second commensurate peak $q_z = 2\pi/p$ as bubble concentration decreases. We determined the center of the diffuse peak Q_z using a Lorentzian fit and plotted it as a function of bubble concentration in Fig. 5.7. As shown in the figure, the diffuse peak shifts smoothly from $q_z = 4\pi/p$ to $q_z = 2\pi/p$ as the bubble concentration ρ is reduced. Above $\rho = 7000$ mm^{-2} and below $\rho = 3500$ mm^{-2} the diffuse peak is absent and the array is commensurate. The smooth migration of the diffuse peak suggests that the C-I-C transition is a second order (or weakly first order) transition. A second order (or weakly first order) C-I-C transition is also supported by the rotation mechanism by which the array evolves as ρ changes. Second order C-I transitions have been predicted for the krypton absorbed on graphite system and for layered superconductor systems [Coppersmith *et al.*, 1981; 1982; Balents and Nelson, 1994; 1995].

If one looks carefully at Fig. 5.5, one can also notice the appearance of two peaks on the q_z axis at wavevectors $q_z = \pm 2\pi/p$, which is half of the q_z value for the initial high concentration commensurate phase. These peaks arise from the periodic pinning potential rather than from any strong first order transition. To understand this we can consider the bubble array as a one-dimensional lattice in the $\hat{z}$ direction, with each basis cell consisting of a row of bubbles. The local Fourier component can be written as

$$e^{i\vec{q}\bullet\vec{r}_i} \cdot \sum_{\vec{r}_j \in \text{row}} e^{i\vec{q}\bullet\vec{r}_j} \qquad (5.6.1)$$

where the summation is the form factor and is over all the bubbles in the row. The phases determined by $\vec{q}\bullet\vec{r}_i$ differ by 180° for neighboring pinned and unpinned rows. In Fig. 5.5(a), the form factors for neighboring pinned and unpinned rows are identical because their row concentrations are the same, so their local Fourier components cancel each other, leading to the absence of the two peaks at $q_z = \pm 2\pi/p$. At incommensurate

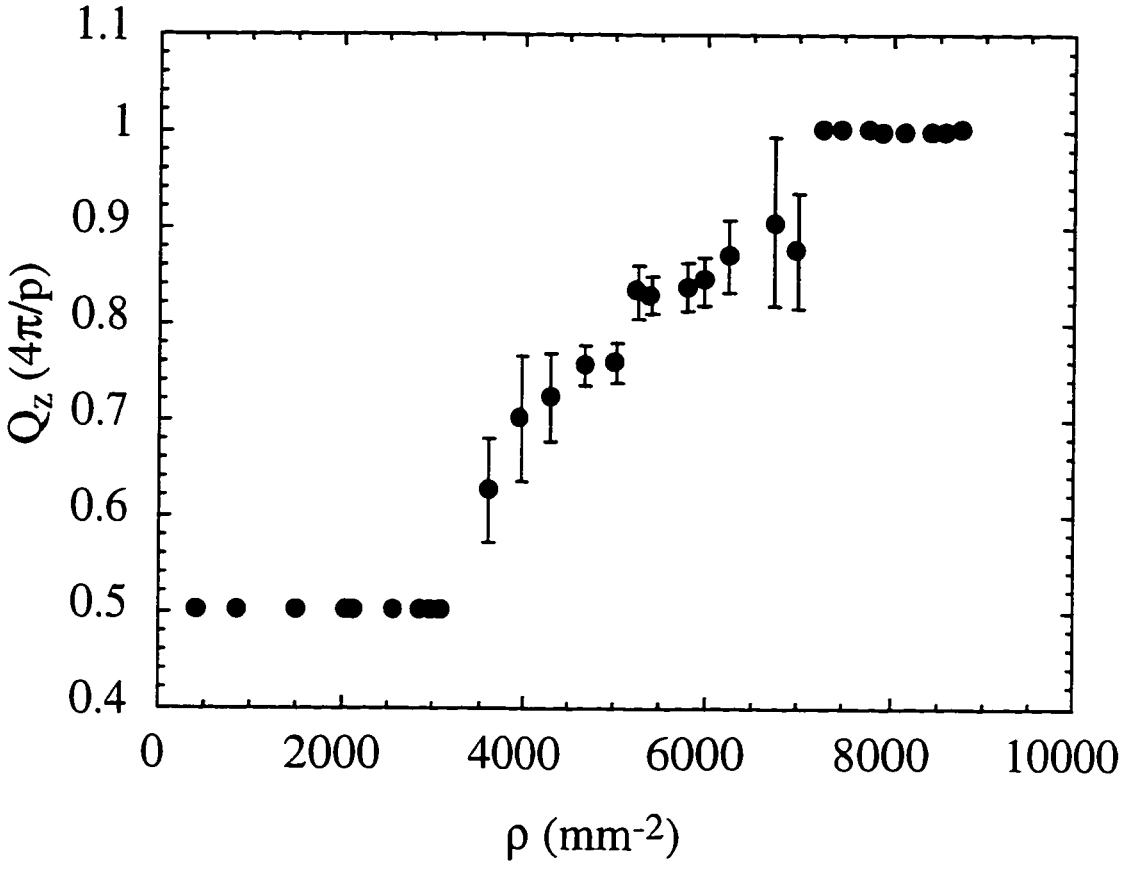

Fig. 5.7 Smooth migration of the wavevector Q_z of the diffuse peak vs bubble concentration ρ. The error bars represent the full width at half maximum.

bubble concentrations the bubble row concentration for the pinned rows is higher than that for the unpinned rows, so the form factors for neighboring pinned and unpinned rows do not cancel, thus the peaks appear. The gradual increase of the peak intensity from Figs. 5.5(b) to 5.5(f) is a result of the increasing difference in the bubble row concentrations between the neighboring pinned and unpinned rows.

5.6 Translational Correlations

The structural translational correlation function $C_{T,S}(\Delta x, \Delta z)$ (Eqn. (5.2.5)) and the commensuration translational correlation function $C_{T,C}(\Delta x, \Delta z)$ (Eqn. (5.2.7)) can be calculated from bubble center data. These functions provide a quantitative measure of structure in the commensurate and incommensurate phases. The reciprocal lattice vectors $\vec{q}_0$ and $\vec{q}_1$ defined in Eqns. (5.2.5) and (5.2.7) are determined from the peaks in the structure function without using a Hanning window. Application of a Hanning window changes the peak location even though it can suppress spurious features.

Figure 5.8 shows contour plots of the structural translational correlation function $C_{T,S}(\Delta x, \Delta z)$ at nine bubble concentrations decreasing from (a) to (i); the number on the top left of each plot is the bubble concentration in bubbles/mm^2. These correlation functions $C_{T,S}(\Delta x, \Delta z)$'s correspond to the data presented in Figs. 5.4 and 5.5. Each plot covers 150 μm in the $\hat{x}$ and $\hat{z}$ directions. Curve-fits show that $C_{T,S}(\Delta x, \Delta z)$ follows exponential decay for all measured bubble concentrations. Two lengths are used to describe the structural translational correlation of the bubble array: $\xi_{T,S}{}^x$ and $\xi_{T,S}{}^z$. The lengths $\xi_{T,S}{}^x$ and $\xi_{T,S}{}^z$ are defined as the exponential decay lengths of $C_{T,S}(\Delta x, \Delta z)$ along the $\hat{x}$ and $\hat{z}$ directions respectively:

$$C_{T,S}(\Delta x, 0) \sim \exp\left(-\Delta x / \xi_{T,S}{}^x\right), \tag{5.6.1}$$

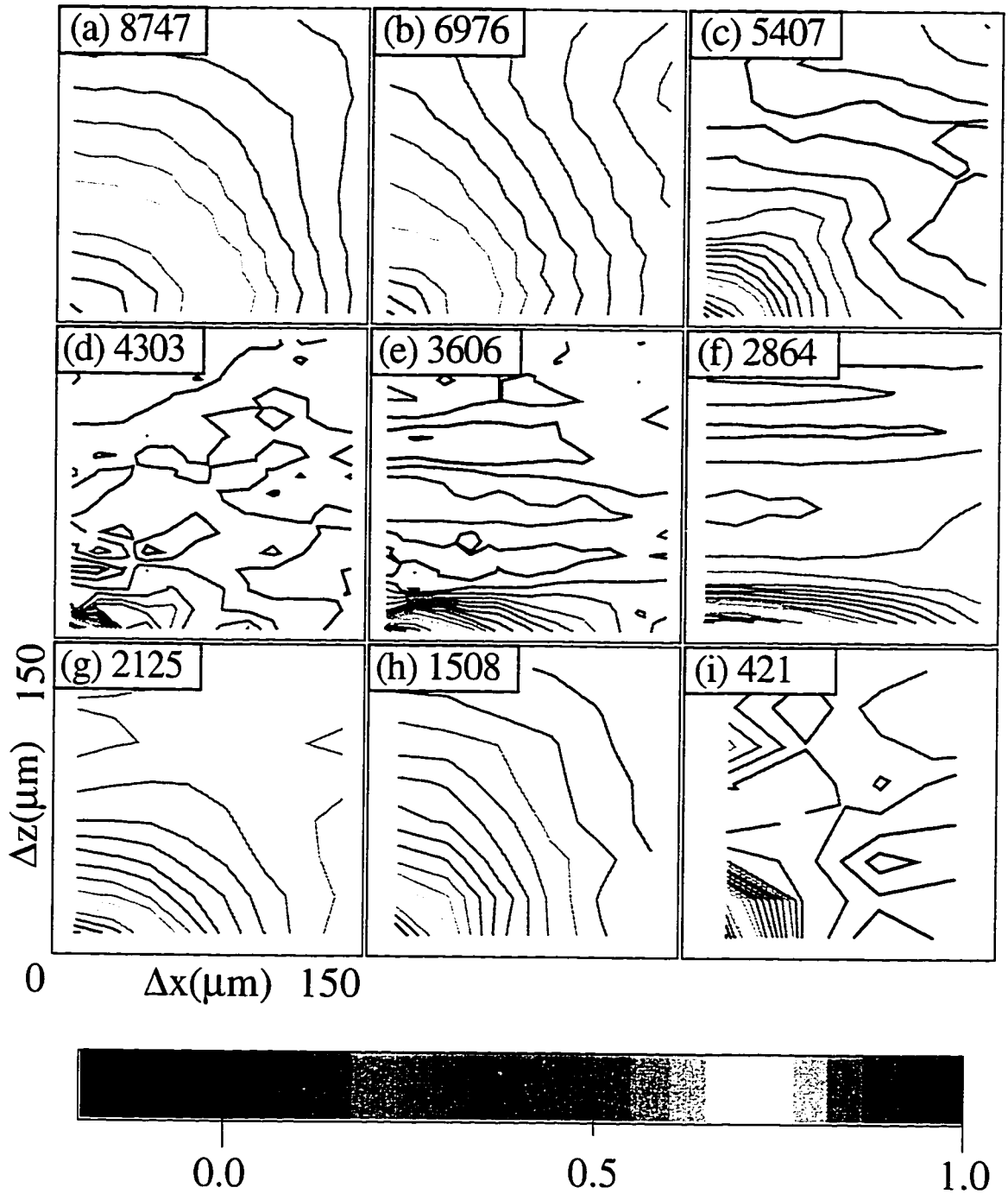

Fig. 5.8(color) Contour plots of structural translational correlation function $C_{T,S}(\Delta x, \Delta z)$ vs bubble separations Δx and Δz for nine bubble concentrations. Δx is in the horizontal direction and Δz is in the vertical direction; both are plotted for up to 150 μm. The bubble concentration ρ (mm^{-2}) is indicated at the upper left of each plot.

and

$$C_{T,S}(0, \Delta z) \sim \exp\left(-\Delta z/\xi_{T,S}{}^{z}\right). \tag{5.6.2}$$

Figure 5.9 shows the measured correlation lengths $\xi_{T,S}{}^{x}$ and $\xi_{T,S}{}^{z}$ vs the bubble concentration ρ determined from exponential fits to the data.

Figures 5.8 and 5.9 show how the structural translational correlation changes as the bubble concentration ρ decreases. Figure 5.8(a) shows $C_{T,S}(\Delta x, \Delta z)$ for the dislocated triangular array at high bubble concentration. As shown in the figure, $C_{T,S}(\Delta x, \Delta z)$ is isotropic. The correlation lengths $\xi_{T,S}{}^{x}$ and $\xi_{T,S}{}^{z}$ ($\geq$ 40a as shown in Fig. 5.9) are comparable to the size of the field of view. Such long translational correlation lengths exist because periodic line pinning stabilizes the array. From Figs. 5.8(a) to 5.8(d), as the array moves from the commensurate triangular array to the incommensurate polycrystalline phase, the structural translational order decreases isotropically. Figure 5.9 shows that both correlation lengths $\xi_{T,S}{}^{x}$ and $\xi_{T,S}{}^{z}$ decrease from $\geq$ 40a in Fig. 5.8(a) to ~ 4a in Fig. 5.8(d). The deterioration of translation order arises from the increased dislocation density in the array associated with rotation of the local array orientation. From Figs. 5.8(d) to 5.8(f), as the array moves from the incommensurate polycrystalline phase to the commensurate smectic phase, the structural translational order becomes anisotropic: the order improves in the $\hat{x}$ direction but remains very short in the $\hat{z}$ direction. At the smectic phase, $\xi_{T,S}{}^{x} \cong$ 20a. From Figs. 5.8(f) to 5.8(h), as the array moves from the smectic phase to the second dislocated triangular array, the structural translational order becomes isotropic again. In this new triangular array, both lengths $\xi_{T,S}{}^{x}$ and $\xi_{T,S}{}^{z}$ are about 10a. There is more disorder at the bubble concentration ρ = 1508 mm^{-2} in Fig. 5.8(h) than at

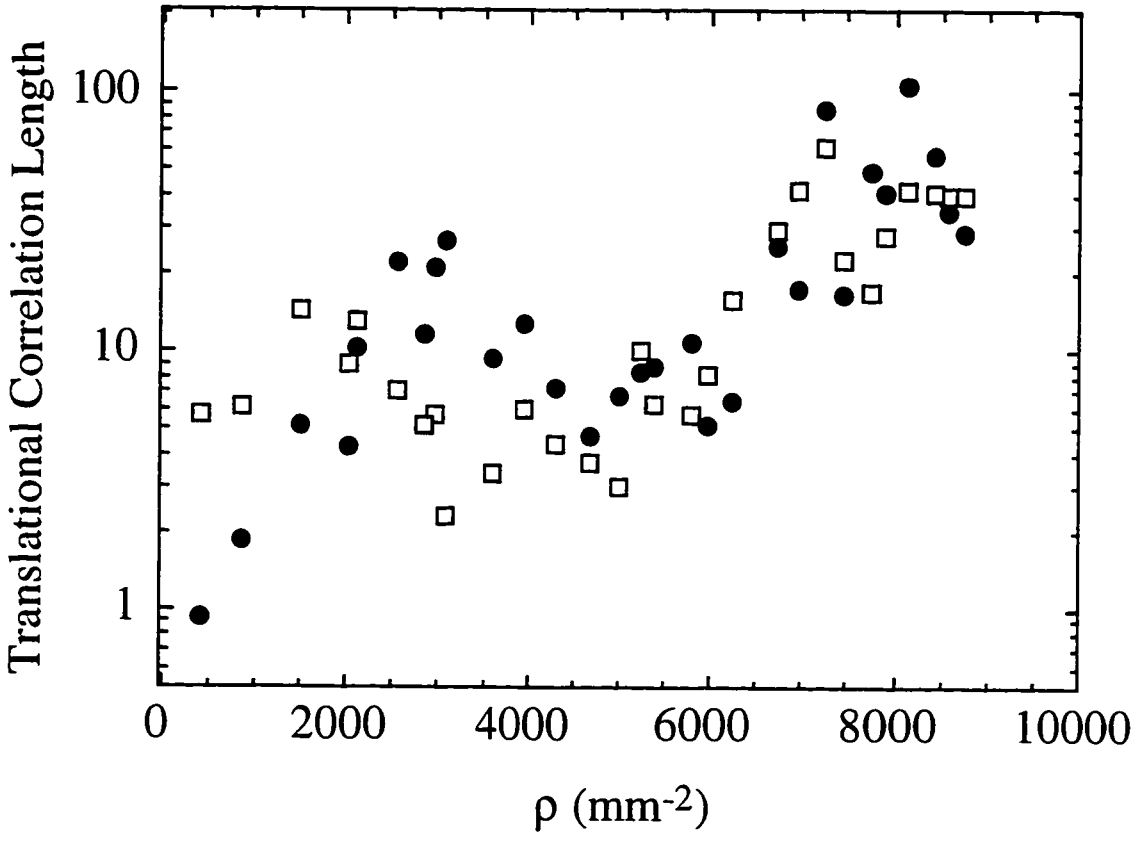

Fig. 5.9 Structural translational correlation lengths vs bubble concentration ρ along two particular directions: the black dots are $\xi_{T,S}{}^{x}$, in unit of a_x,; the open squares are $\xi_{T,S}{}^{z}$, in unit of a_z.

$\rho = 8747\ mm^{-2}$ in Fig. 5.8(a). In the modulated liquid phase in Fig. 5.8(i), the structural translational order is destroyed by unbinding of dislocations.

Plots of the commensurate translational correlation functions $C_{T,C}(\Delta x, \Delta z)$ corresponding to Fig. 5.8 are shown in Fig. 5.10. Figure 5.10(a) and Figs. 5.10(f) to 5.10(i) are for commensurate bubble concentrations, while Figs. 5.10(b) to 5.10(e) are for incommensurate concentrations. As can be easily seen from Fig. 5.10, $C_{T,C}(\Delta x, \Delta z)$ is quasi-long ranged (i.e. algebraic decay) when the array is in a commensurate phase but the order deteriorates drastically once the array becomes incommensurate. The correlation function $C_{T,C}(\Delta x, \Delta z)$ becomes exponential decay at the incommensurate polycrystalline phase. The rapid deterioration of the commensuration translational order at incommensurate concentrations arises form the fact that the local array orientations rotate to reduce the total energy and some bubbles no longer stay at the bottom of the pinning potential.

5.7 Even-Odd Symmetry Breaking

In this and next sections we present our observations of C-I phase transitions in samples with short pinning periodicity $p = 10\ \mu m$ and weak pinning strength $t = 37$ Å. At this pinning periodicity every pinning line is occupied by a row of bubbles at the highest commensurate concentration measured. As the bubble concentration decreases, the system evolves to a triangular array with two pinning lines per row of bubbles. Because the symmetry of even and odd pinning lines is broken, we call this even-odd symmetry breaking. This type of symmetry breaking does not occur in samples with $p = 20\ \mu m$ above because every pinning line is occupied by bubbles.

Figure 5.11 shows a series of processed bubble array images at six decreasing bubble concentrations indicated in upper left corner. These images demonstrate how symmetry breaking occurs. A bubble is coded with dark gray if it belongs to an odd numbered

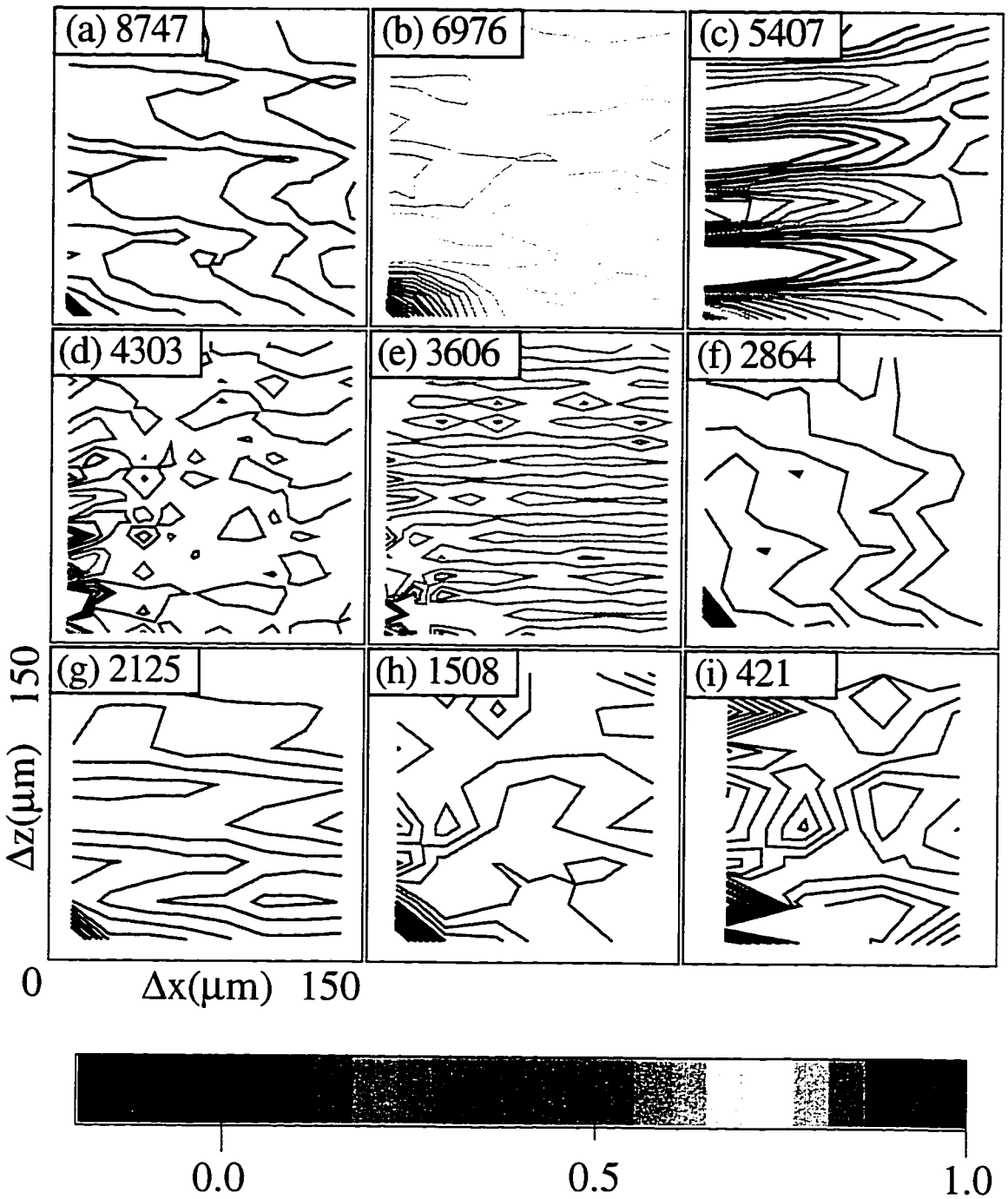

Fig. 5.10(color) Contour plots of commensuration translational correlation function $C_{T,C}(\Delta x, \Delta z)$ vs bubble separation Δx and Δz for nine bubble concentrations. Δx is in the horizontal direction and Δz is in the vertical direction; both are plotted for up to 150 μm. The bubble concentration $\rho(mm^{-2})$ is indicated at the top left of each plot.

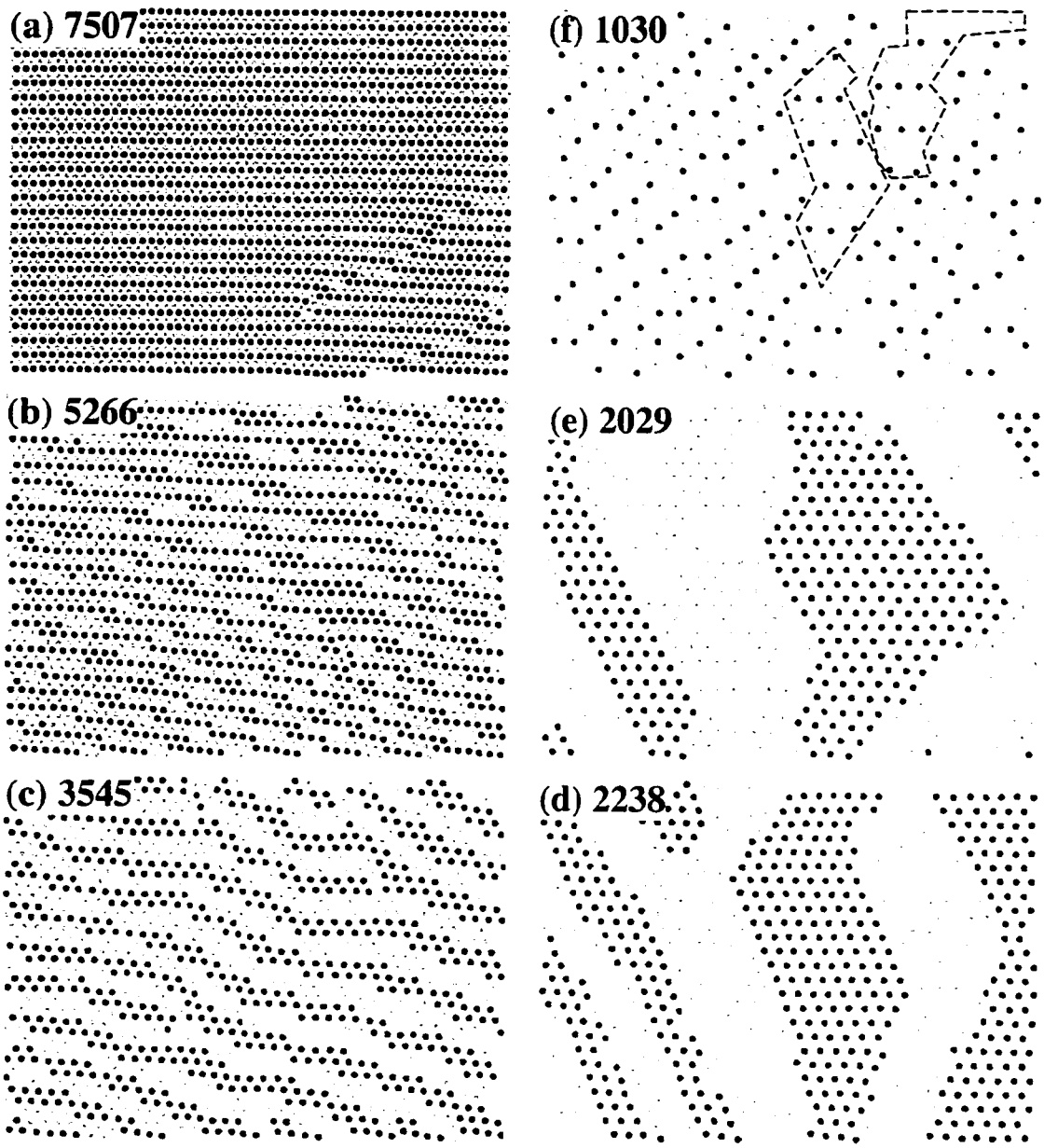

Fig. 5.11 Processed bubble array images to show how even-odd symmetry breaking happens. The dark dots represent bubbles in the odd numbered pinning lines; the light dots represent bubbles in the even numbered pinning lines. The separation of dark and light bubbles indicates even-odd symmetry breaking. The areas surrounded by dashed lines in (e) have 3 pinning lines per row of bubbles.

pinning line, and a bubble is coded with light gray if it belongs to an even numbered pinning line. We can study how the even-odd symmetry breaking happens by observing how bubbles coded with different shades move as the bubble concentration decreases.

Figure 5.11(a) shows a commensurate triangular array at high bubble concentration. There is some cross over of bubble rows from one pinning line to the neighboring pinning line at the lower right corner. The nearest neighbor bond of the array is parallel to the pinning lines. The alternating dark and light bubble rows indicate that both odd and even numbered pinning lines are occupied and there is no symmetry breaking in Fig. 5.11(a).

In Figs. 5.11(b) and 5.11(c), the entire array rotates to lower its energy as the bubble concentration decreases. As shown in the figures, the array remains a single domain, but the nearest neighbor bond is no longer parallel to the pinning direction. This rotation mechanism also accounts for the formation of the incommensurate polycrystalline phase in samples with $p = 20$ μm. We can also see in these two figures that the dark and light bubbles begin to separate into groups. In Fig. 5.11(c) two dark rows and two light rows alternate.

In Figs. 5.11(d) and 5.11(e), the rotation of array orientation stops, the bubbles stabilize at the center of the nearest pinning line, and the size of the dark and light bubble domains increases. An even-odd symmetry breaking phase occurs in Fig. 5.11(e) where the separation between the dark and light domains is maximum: there are only three dark and three light bubble domains over the field of view. In the dark domain only odd numbered pinning lines are occupied, while in the light domain only even numbered pinning lines are occupied . We did not observe a single crystal array over the field of view with only dark or only light bubbles. The dark and light domains coexist because they have the same energy. It is interesting to notice that these domains form a "striped" phase which has domain walls approximately perpendicular to the pinning lines. Domain walls cost energy, so it would be ideal to have a single domain in order to minimize the energy. However, in the striped phase the internal stress along the domain walls is very weak, thus

the additional energy needed for the domain walls is small. One way to single out one configuration would be to set the pinning strength of odd and even numbered pinning lines slightly different. The extreme situation where the pinning strength of all odd or all even pinning lines is zero, i.e. twice the periodicity, has been discussed in Sections 5.4 to 5.6. In that case, the new commensurate phase does have only one configuration.

When the bubble concentration is further reduced, the bubble-bubble interaction is too weak to maintain a triangular array. Figure 5.11(f) shows a disordered bubble array at very low bubble concentration. It is interesting to see that some domains have three pinning lines per row of bubbles, as shown in the areas surrounded by dashed lines. These small domains are symmetry breaking regions where the pinning lines with $n = 3m$ and $n = 3m+1$, $3m+2$ ($m = 0, 1, 2, ...$) are no longer equivalent.

Figures 5.12(a) to 5.12(f) show plots of the structure functions corresponding to the data in Figs. 5.11(a) to 5.11(f). The features in Fig. 5.12 confirm our direct analyses of the bubble array images in Fig. 5.11:

1) In Figures 5.12(b) to 5.12(c) the six reciprocal lattice vectors have clearly rotated slightly, while in Fig. 5.12(d) the rotation has disappeared.

2) In Figure 5.12(e) the peaks at the second commensurate peaks $q_z = \pm 2\pi/p$ are not sharp because of the cancellation between dark and light bubble domains.

3) In Figure 5.12(f) there are three vaguely recognizable peaks between the origin and the first commensurate peak, associated with the regions having three pinning line per row of bubbles.

5.8 Further Discussion of Commensurate-Incommensurate Transitions

In this section we compare the commensurate-incommensurate transitions for the two pinning conditions: short period $p = 10$ μm and $t = 51$ Å and long period $p = 20$ μm and $t = 51$ Å, and contrast these with isotropic melting.

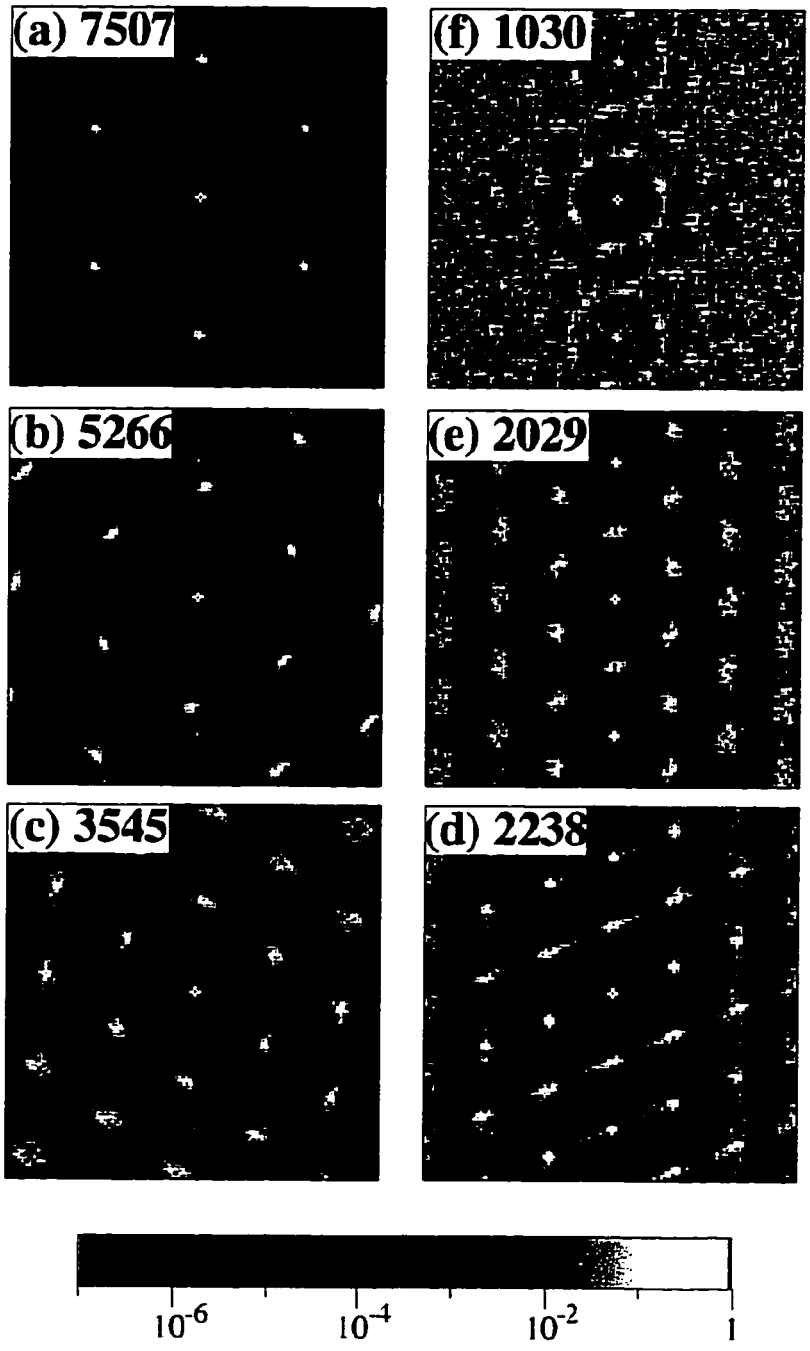

Fig. 5.12(color) Structure functions S(q) corresponding to Figs. 5.11(a) to 5.11(f) showing the C-I transitions at p = 10 μm and t = 37 Å.

The phase diagram of a system subject to periodic pinning depends on two factors: pinning periodicity and strength. A comparison of the structure function plots in Fig. 5.12 for short pinning period and weak pinning strength with Fig. 5.5 for long pinning period and moderate pinning strength reflects the similarity and difference between samples with different pinning periodicity and strength. In both pinning conditions, the migration of the peaks from the first commensurate peak to the second commensurate peak is continuous, indicating that the C-I-C transition is a second order (or weakly first order) transition. The phase transitions take place via rotation of the array orientations. For long period and moderate pinning condition in Fig. 5.5, the stress in the array is more difficult to relax, so the rotation leads to a polycrystalline phase; for short period and weak pinning condition in Fig. 5.12, the stress is easier to relax, so the rotation leads to a rotated triangular array. The smectic phase does not appear for the short period and weak pinning condition in Fig. 5.12 because the pinning is too weak: internal stress can be relaxed so the phases of the one-dimensional arrays are well correlated. In Fig. 5.12 where $p = 10\ \mu m$, the second commensurate peaks turn on when the migrating peaks arrive, rather than gradually turning on as in Fig. 5.5 where $p = 20\ \mu m$. This is because at $p = 10\ \mu m$, every row of bubbles is pinned and the reduction in the bubble row concentration is uniform at all bubble concentrations.

The phase transitions in systems with periodic pinning are different from those without periodic pinning. Seshadri and Westervelt [1991] studied the melting of a magnetic bubble array without any external pinning. They observed a continuous phase transition from hexatic to liquid phase. In bubble arrays without periodic line pinning, the phase transition is driven by the unbinding of dislocations. The structure function shows broadening of the six peaks and no rotation of array orientation is observed. The phase transitions in bubble arrays with periodic line pinning is more complex in that rotation of array orientations, symmetry breaking phases, and smectic phases all can happen.

5.9 Summary

In this chapter we have reported our observation of the commensurate-incommensurate-commensurate phase transition in two-dimensional magnetic bubble arrays subject to periodic line pinning with moderate to weak pinning strength. The periodic lines introduce a preferred orientation for the commensurate bubble array: the nearest neighbor bond is always parallel to the pinning lines, as expected from the theory by Balents and Nelson [1995]. As bubble concentration changes, the array orientation rotates either locally or globally depending on the pinning strength. Using direct imaging and structure function analyses, we have identified a number of phases in the bubble system, including an incommensurate polycrystalline phase and a commensurate smectic phase. The phase transitions between commensurate and incommensurate phases are second order (or weakly first order) as indicated by the smooth migration of diffuse peaks from the first commensurate peaks to the second commensurate peaks. This migration agrees with previous experimental results [Moncton *et al.*, 1981] and theoretical predictions [Coppersmith *et al.*, 1981; 1982; Balents and Nelson, 1994; 1995]. we have also observed an even-odd symmetry breaking phase in the bubble array when the pinning periodicity is smaller than the bubble row spacing, associated with preferential occupation of a periodic subset of the pinning lines by the bubbles.

Direct observations of the commensurate-incommensurate-commensurate transition in magnetic bubble system where both pinning periodicity and strength are controllable provide detailed information about every stage of the commensurate-incommensurate transitions. We hope that the results from this experiment will provide some insight for future theoretical work and help understanding of other systems in which a direct observation of the commensurate-incommensurate transition is difficult.

CHAPTER 6 CONCLUSIONS

In this chapter we summarize the major results of the experiments presented in previous chapters and we also present ideas for future work. In this thesis we have studied collective transport phenomena and commensurate-incommensurate phase transitions in the two-dimensional magnetic bubble system. These experiments have enriched our knowledge about the structural and dynamical properties of two-dimensional statistical systems. These experiments have demonstrated that the magnetic bubble system is an excellent model system in which to study two-dimensional statistical physics because of its real time observation and controllable pinning.

In Chapter 4 we discussed collective transport of the two-dimensional magnetic bubble array subject to a random substrate potential. The bubble arrays in this case are triangular arrays with zero or very few isolated dislocations. We measured the velocity-force response at a series of ac agitation fields. Data show that this response follows the power law $v \propto F^3$. The effective thermal fluctuations at these ac fields are characterized by the standard deviation σ of the bubble displacement over 24 minutes in the absence of any applied force. A similar σ/a ($= 0.039 \pm 0.004$) was found for all these ac fields, indicating similar effective temperature at these fields. This explains why the exponent in the power law remains constant at these ac fields. Comparison of σ/a with the Lindemann criterion shows that the temperature is well below the melting temperature. The power law behavior of the bubble velocity-force response agrees with the theoretical prediction for two-dimensional elastic media [Batrouni and Hwa, 1994; Carraro and Nelson, 1996].

The spatiotemporal behavior of the transport was examined using captured bubble array images. The bubbles are found to move in clusters and the velocity histogram deviates from Gaussian distribution at nonzero forces. This clearly shows that the bubble

motion is collective. Sequential time resolved images show that the bubble motion is nonuniform during short time intervals, but uniform over long times. The measured velocity-velocity correlation length increases monotonically with the applied force, which may suggest that the force range is below the zero temperature depinning threshold. This microscopic examination of spatiotemporal motion in a system subject to random pinning not only reveals the nature of collective transport but also fills a gap in our understanding of friction and drag.

In Chapter 5 we discussed commensurate-incommensurate transitions in magnetic bubble arrays subject to periodic line pinning, which occur as the bubble concentration decreases. Direct observations show that C-I transitions take place via rotation of the bubble array orientations. Under moderate pinning condition the bubble array rotates locally and an incommensurate polycrystalline phase is formed, while under weak pinning the bubble array rotates globally and an incommensurate triangular array is formed. Structure function analyses show that as the array undergoes C-I-C transition, a diffuse peak emerges and migrates from the first commensurate peak to the second commensurate peak, indicating a second order (or weakly first order) phase transition. Periodic pinning introduces broken symmetry to the system, resulting in a richer phase diagram than that in the absence of periodic pinning. We have observed a commensurate smectic phase in which translational order exists in the pinning direction but not in the perpendicular direction. We have also observed an even-odd symmetry breaking phase with two pinning lines per row of bubbles in which the symmetry between odd and even numbered pinning lines is broken.

We conclude this thesis by discussing some remaining issues and also pointing out future directions. First, we discuss some theoretical issues. There has been a considerable amount of theoretical work on collective transport and C-I transitions for systems ranging from charge density waves to type II superconductors. However a theory specifically for the magnetic bubble system is lacking. A theoretical model for the bubble system including

bubble-bubble interaction, substrate pinning, permalloy pinning, and effective thermal fluctuations would be valuable, making quantitative comparison of observation results and theoretical predictions possible. For example, in the collective transport experiment, knowing the bubble-bubble interaction, substrate pinning, and effective temperature, we could calculate the values of the critical temperature, the exponent in the power law velocity-force response, and the zero temperature depinning threshold, and then compare with our measurements. In the C-I transition experiment, knowing the pinning potential due to the permalloy bars, we could obtain a theoretical phase diagram and compare it with our observation.

Now we turn to an interesting project related to our collective transport work. In the collective transport experiment we investigated the elastic flow of a bubble array subject to weak random pinning. Transport under strong pinning is equally interesting. Theory and computer simulations have predicted that the transport is characterized by channel flow and is accompanied by plastic deformation in the array. Strong random pinning in the bubble system can be achieved by a random array of permalloy disks. The disk size, thickness, and separation between neighboring disks have to be chosen carefully in order to observe the channel flow.

Finally, we discuss interesting projects related to periodic pinning. In Chapter 5 we investigated the C-I transitions in the bubble arrays subject to weak periodic pinning. One natural extension of this work is to study the phase transitions in the bubble system subject to strong periodic pinning. Theory predicts that several new types of crystal structures can form [Ivlev, Kopnin, and Pokrovsky, 1990; Levitov, 1991]. The chromium mask with $p = 10\ \mu m$ can be used here for fabrication of the permalloy pinning bars. However the permalloy bars should be thick enough so that bubbles can only move within the bars but can not cross over to other bars. Another extension of the C-I transition work is to study phase transitions in the bubble system subject to other periodic pinning geometries, such as a periodic array of honeycomb structures. The bubble system under honeycomb pinning

mimics the rare-gas atoms adsorbed on graphite. Observation of the phase transitions in this system is interesting, because a combination of direct imaging and structure function analyses can map out the phase diagram. Comparison of this result with existing theory and results from scattering measurements on krypton adsorbed on graphite systems may provide new insight into the nature of the C-I transitions. It would be also interesting to study the phase transitions in the bubble system subject to a square or a triangular array of permalloy disks. Such a system mimics vortices subject to columnar pinning [Reichhardt *et al.*, 1996]. The transport behavior of the above systems would be a very interesting problem to investigate.

APPENDIX A SHEAR FLOW

In this appendix we report our measurements of shear flow in a magnetic bubble array in which half of the array is permanently pinned by a random array of permalloy disks. The flow is driven by a uniform force acting on all bubbles equally. We are interested in the behavior of the width of the shear region near the interface as the force decreases. This shear width δ is analogous to the dynamic glass correlation length ξ_G in vortex glass theory [Fisher, Fisher, and Huse, 1991; Fisher, Tokuyasu, and Young, 1991]. Seshadri and Westervelt [1993a, 1993b] measured the shear width δ at H_{ac} = 14.1 Oe and observed that δ is of the order of the translational correlation length at all bubble concentrations. In our measurement, we reduced the ac field to H_{ac} = 11.9 Oe and measured the dependence of δ on the force. We observed that as the force decreases, δ increases to at least 5 times the translational correlation length ξ_T as the force decreases.

Shear Flow Theory

We used the same geometry as the one in the forced flow measurement [Seshadri and Westervelt, 1993a and 1993b]. This geometry was originally suggested by Marchetti and Nelson [1990, 1991]. Figure A.1(a) illustrates the geometry. The bottom part of the array is strongly pinned so that no motion is possible in this region. The top part of the array is only subject to weak random pinning due to substrate roughness. A uniform in-plane driving force $\bar{F}$ is applied parallel to the interface between the strongly and weakly pinned regions. The equation of motion can be written as

$$\bar{F} = -\gamma\bar{v} + \eta\nabla_{\perp}^{2}\bar{v}, \qquad (A.1)$$

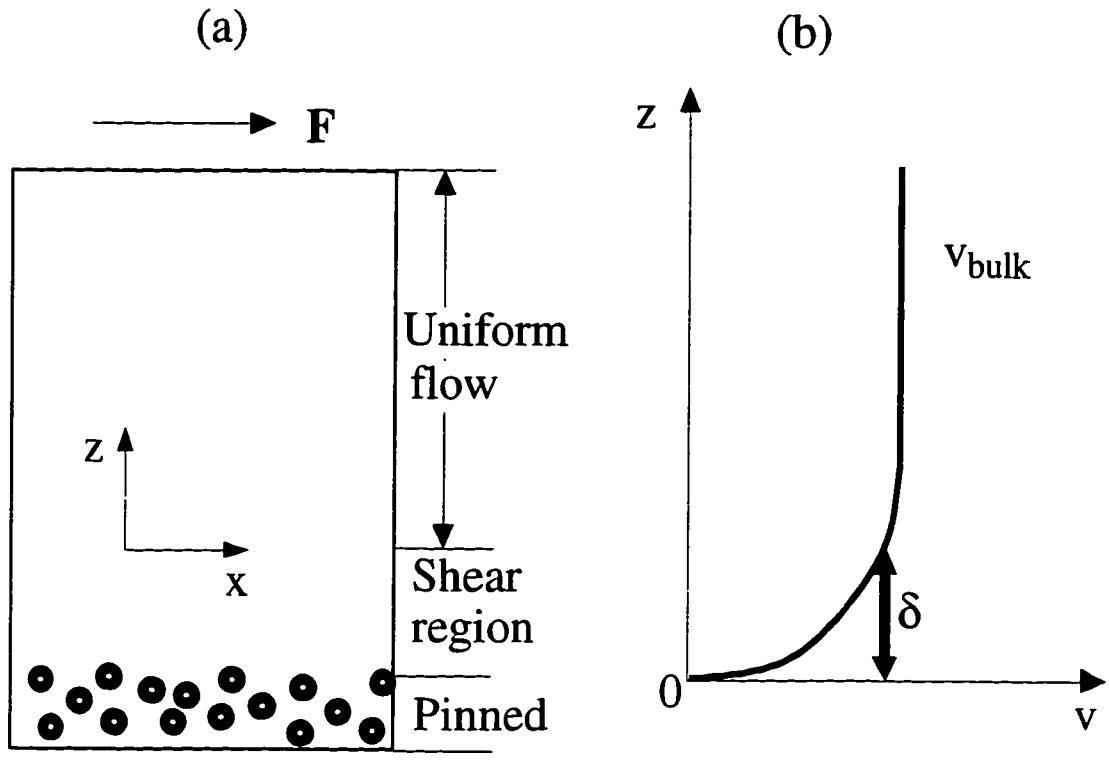

Fig. A.1 Illustration of shear flow theory and experimental scheme. (a) Idealized experimental geometry for shear flow measurement. (b) Velocity profile.

where γ is the friction coefficient associated with the substrate pinning and η is the shear viscosity associated with the bubble-bubble interaction. We choose the direction parallel to the interface as the $\hat{x}$ direction and the direction normal to the interface as the $\hat{z}$ direction. Figure A.1(b) is a sketch of a possible velocity profile in the $\hat{z}$ direction. In the strongly pinned region the bubble velocity v is zero. Away from the interface the flow is uniform with $v = F/\gamma$. The region near the interface is the shear region. In this region the velocity v has a profile given by

$$v(z) = v_{bulk}\left(1 - e^{-z/\delta}\right), \tag{A.2}$$

where v_{bulk} is the average velocity in the uniform flow region and δ is the width of the shear region:

$$\delta = (\eta/\gamma)^{1/2}. \tag{A.3}$$

The shear width δ in shear flow measurement is analogous to the vortex glass correlation length ξ_G [Fisher, Fisher, and Huse, 1991; Fisher, Tokuyasu, and Young, 1991] because they both measure the distance over which information about a boundary condition is conveyed in a flowing array. Vortex glass theory [Fisher, Fisher, and Huse, 1991; Fisher, Tokuyasu, and Young, 1991] predicts that the glass correlation length ξ_G will grow as the vortex array becomes more glassy. However it is difficult to measure ξ_G because it is a dynamical rather than a static correlation length. In this experiment we indirectly study ξ_G by measuring the shear width δ from velocity profile using the geometry illustrated in Fig. A.1(a).

Experimental Method

The sample is taken from a LLC garnet in which the random substrate roughness is very weak. Figure A.2 is an image of bubble array with half-plane pinning. The half-plane pinning consists of a random array of permalloy disks. Each disk is 50 Å thick and 12 μm in diameter. The average spacing between the centers of neighboring two permalloy disks is 30 μm. This pinning condition effectively prevents the bottom half of the bubble array from moving during application of driving forces.

In our experiment, the bubble array is annealed for 48 hours after nucleation to produce a triangular array with a translational correlation length $\xi_T = 8a$ (see Eqn. (4.3.3)) and quasi-long range orientational order. The bubble array is continuous across the interface. Bubble motion is recorded at a bubble concentration $\rho = 3518$ mm^{-2} and a 40 Hz ac magnetic field $H_{ac} = 11.9$ Oe. We recorded bubble motion at a series of increasing driving forces. Each force is applied for 1 minute. After each application of the force, the array is given ample time to relax to avoid formation of bubble concentration gradient. At each force, the measurement is repeated at two areas of the sample: area I is shown in Fig. A.2 and area II is the area right above area I, with greater z. Two areas are measured so that we can better determine the bulk velocity, because the bubble motion in area II is rather uniform and can be treated as uniform flow region.

Experimental Results

Figure A.3 shows the bulk velocity v_{bulk} vs the driving force F, obtained from area II. The bulk velocity is obtained by averaging over all the bubbles in the area. In our measurement $H_{ac} = 11.9$ Oe is smaller than H_{ac} used in forced flow experiment [Seshadri and Westervelt, 1993a and 1993b]. The resulting bubble array is more glassy at this low ac field. As shown the velocity-force response is nonlinear at small forces. Figure A.4 shows the velocity profiles at four forces, obtained from area I. The velocity is calculated

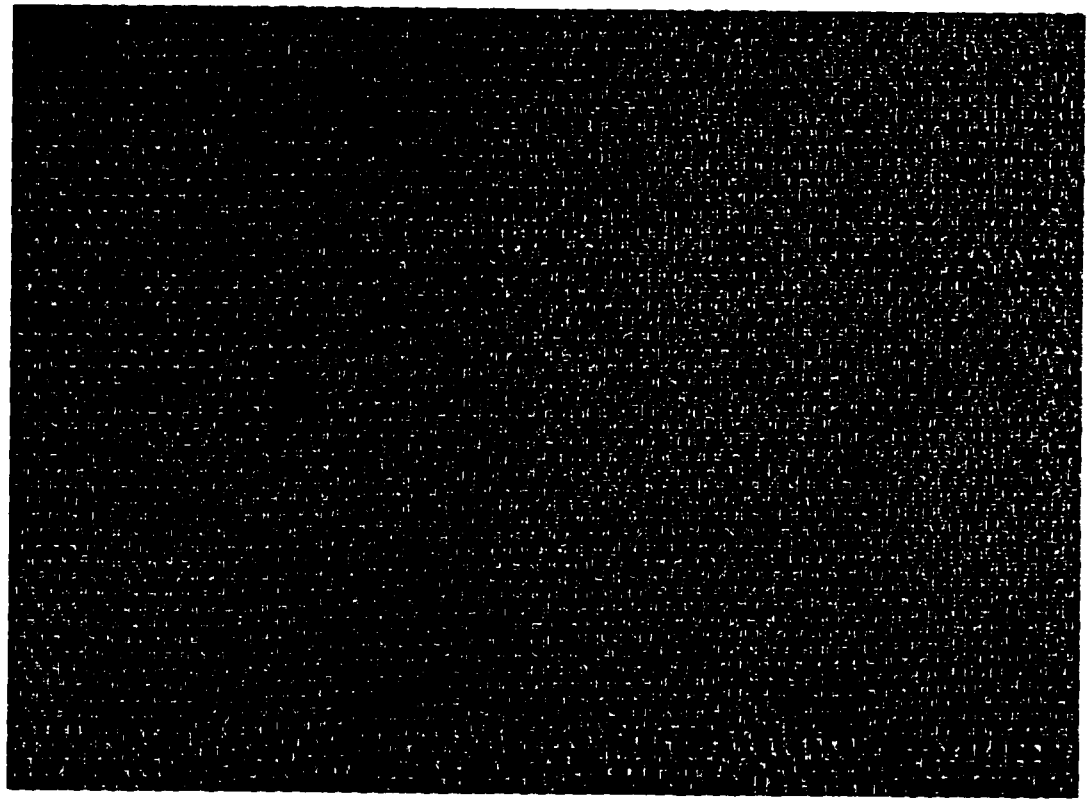

Fig. A.2 Image of the magnetic bubble array with half-plane pinning. The image size is 1074 x 788 μm^2. The bigger black dots near the bottom of the image are permalloy disks.

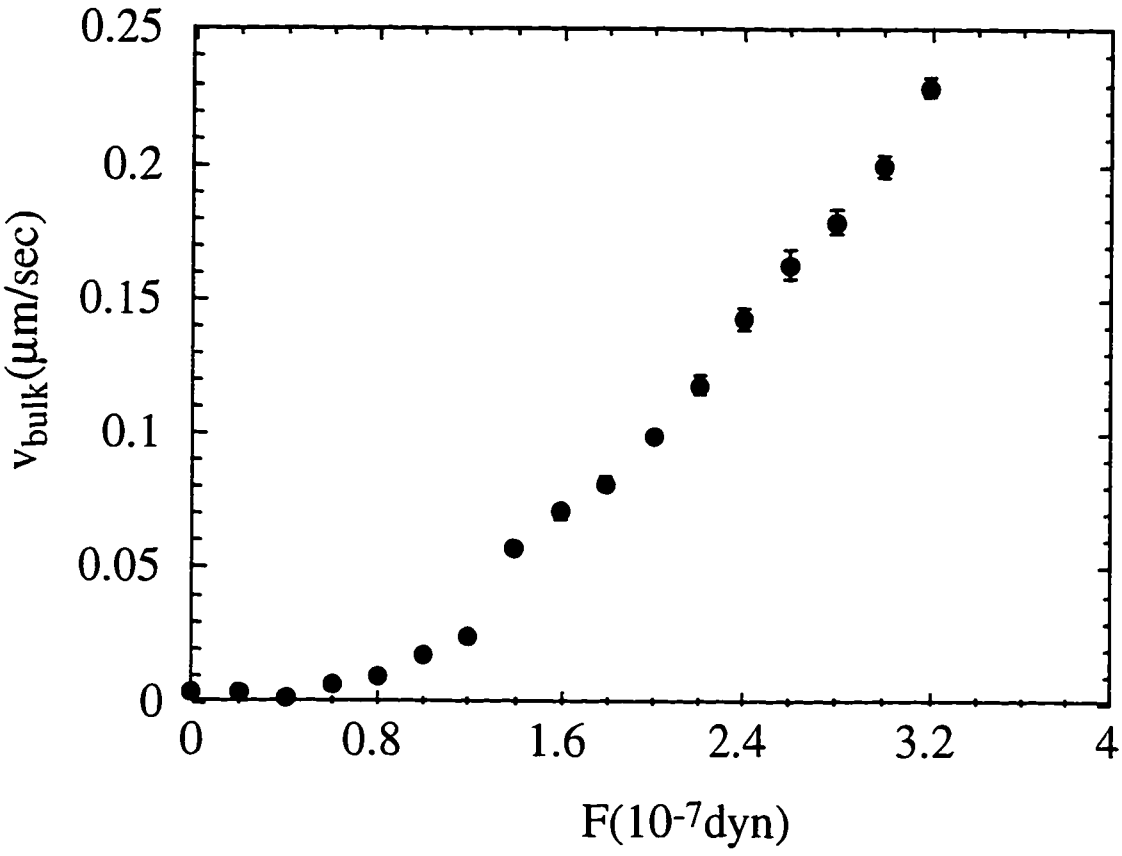

Fig. A.3 Average bulk velocity v_{bulk} vs the driving force F at a bubble concentration $\rho = 3518\ mm^{-2}$ and $H_{ac} = 11.9$ Oe.

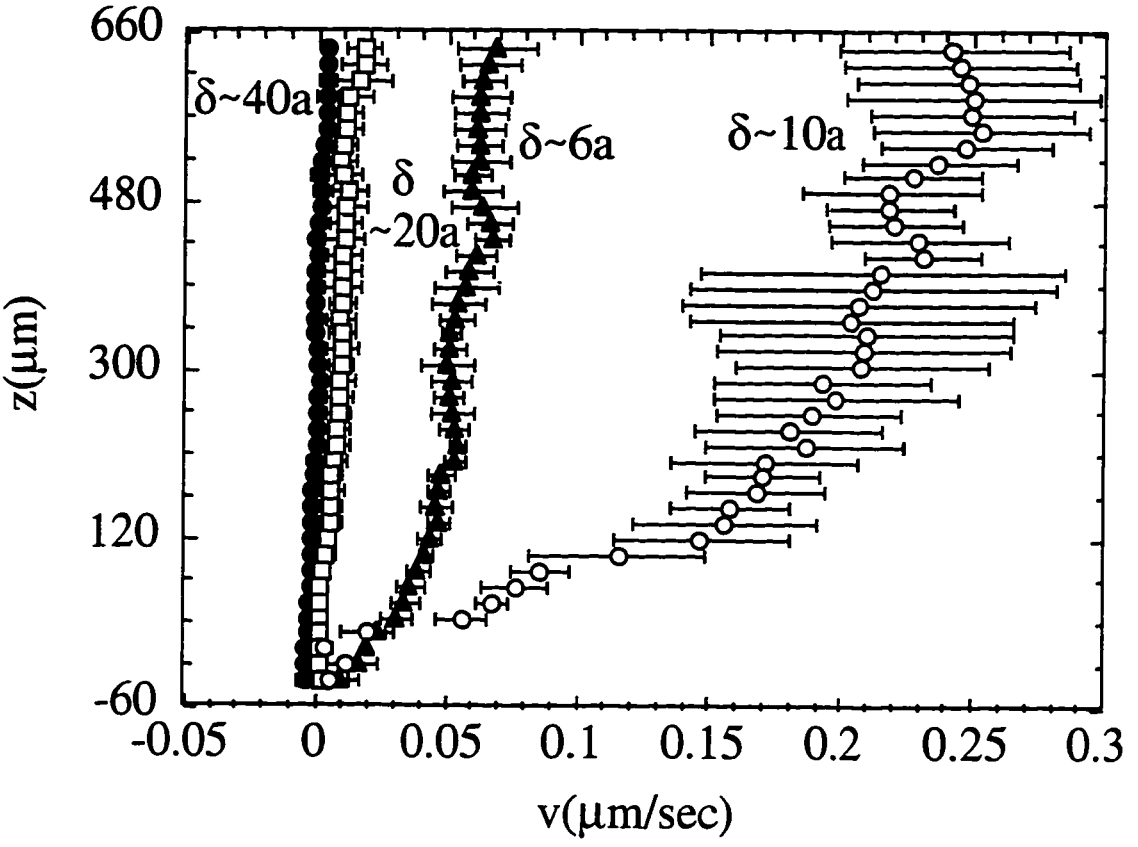

Fig. A.4 Velocity profiles in shear region at four driving forces $F = 0.6 \times 10^{-7}$ dyn (black dots), $F = 0.8 \times 10^{-7}$ dyn (open squares), $F = 1.6 \times 10^{-7}$ dyn (black triangles), and $F = 2.4 \times 10^{-7}$ dyn (open circles).

by first dividing the bubble array in area I into 22 equal sections along the $\hat{z}$ direction and then averaging over all the bubbles within each region. The error bars represent the velocity fluctuations in the $\hat{x}$ direction. The shear width δ can be obtained from the velocity profile using Eqn. (A.2): we use the corresponding velocity data from Fig. A.3 as v_{bulk} in Eqn. (A.2). As the force decreases from 2.4 x 10^{-7} dyn to 0.6 x 10^{-7} dyn, the shear width δ increases from the order of the translational correlation length $\xi_T = 8a$ to the size of the imaging area ~ $5\xi_T$. The increasing of the shear width δ suggests that the glass correlation length ξ_G might increase to several times the translational correlation length ξ_T and further indicates that ξ_G might diverge when the array becomes more glassy, as expected from vortex glass theory [Fisher, Fisher, and Huse, 1991; Fisher, Tokuyasu, and Young, 1991].

APPENDIX B
SAMPLE CODE OF IMAGE PROCESSING AND DATA ANALYSIS APPLICATIONS

Image processing and data analysis code was developed for our Silicon Graphics IRIS Indigo workstation equipped with Entry Graphics and IndigoVideo card. Source code can be found under the directory /usr/people/junmin/BubbleAnalyze/src. Code involving image processing and display will only operate on the above machine, while other code is portable and should work for most UNIX workstations with little modification. Even though the code we developed is for analysis of the magnetic bubble system, the application of our code is not limited to the bubble system. It can be easily adapted to analyze systems such as vortices in high T_c superconductors, colloidal systems and blood cells in medical imaging.

The references from Silicon Graphics were useful for writing codes related to videos and images. *Digital Media Programming Guide: Audio, MIDI, Video, and Compression* has useful examples on image capturing. *Graphics Library Programming Guide, Volume I and II* and *Graphics Library Windowing and Font Library Programming Guide with Font Library Man Pages* have useful examples on window handling and image writing, manipulation, and display.

The three sample C codes listed in this appendix were selected from image acquisition, processing, and data analysis respectively. The image acquisition application *LiveVideo.c* can capture single video frame or a sequence of video frames at constant time intervals. We use video input source 1 for capturing. Luma delay is set to 3 for optimal image quality. Both input source and luma delay can be accessed from *Video Control Panel*, a commercial application for Silicon Graphics workstations. The application *Video Control Panel* can

capture video images, but it is not ideal for our purpose. It can not save grabbed images as grayscale images, and in continuous capturing mode the time interval is controlled by clicking the mouse each time a frame is captured, therefore the user does not have precise control of the timing. The image processing application *FindCenters.c* is used to determine the center locations of magnetic bubbles within an image frame from a grayscale bubble array image. The application *StrucFuncw.c* computes the structure function of a bubble array according to the bubble center data. It uses a Hanning window with cylindrical symmetry to suppress the effect of finite image size.

```
/*** LiveVideo.c      8/14/93                    ***
 *                                                *
 * captures video frames at constant time         *
 * intervals, and save as SGI grayscale images.   *
 */

#include <stdio.h>
#include <stdlib.h>
#include <string.h>
#include <svideo.h>
#include <gl/gl.h>
#include <gl/image.h>
#include
  </usr/people/4Dgifts/iristools/include/lum.h>
#include <gl/device.h>

#define GRABFRAME  "gry."

/* rgbbuf can't be an automatic variable */
static char rgbbuf[307200 * sizeof(long)];

/* concatenate number to string */
char *con_num_to_str ( char s1[], int n1, long n)
{
  char s2[12];
  int  i, t, temp;

  if (n > 99999)
    exit(2);
  temp = n;
  for ( i = 0; i < n1; i++)
    s2[i] = s1[i];

  if ((t = temp / 10000) != 0)
  {
    s2[n1] = t + '0';
    temp = temp % 10000;
  }
  else
    s2[n1] = '0';

  if ((t = temp / 1000) != 0)
  {
    s2[n1+1] = t + '0';
    temp = temp % 1000;
  }
  else
    s2[n1+1] = '0';

  if ((t = temp / 100) != 0)
  {
    s2[n1+2] = t + '0';
    temp = temp % 100;
  }
  else
    s2[n1+2] = '0';

  if ((t = temp / 10) != 0)
  {
    s2[n1+3] = t + '0';
    temp = temp % 10;
  }
  else
    s2[n1+3] = '0';
  s2[n1+4] = temp + '0';
  s2[n1+5] = '\0';
  return (s2);
}

/* grayscale RGB data to grayscale, and dump      *
 * grayscale data to image file.                  *
 */
void dump_image(char *out_file, char *data)
{
  IMAGE *image;
  short rbuf[640];
  short gbuf[640];
  short bbuf[640];
  short obuf[640];
  int x, y;

  image=iopen(out_file, "w", RLE(1), 2, 640, 480);
    for (y = 0; y < 480; y++)
  {
    for (x = 0; x < 640; x++)
    {
        bbuf[x] = *(data + 1);
      gbuf[x] = *(data + 2);
      rbuf[x] = *(data + 3);
        data += 4;
    }
    rgbrowtobw(rbuf,gbuf,bbuf,obuf,640);
    putrow(image, obuf, y, 0);
  }
    iclose(image);
}

main (int argc, char *argv[])
{
  long     dev, still_win, live_win;
  short    val;
  SVhandle V;
  svCaptureInfo svci;
  int   hz, i = 0, capture_period, total_frames;
  void *captureData;
  char *out_file;

  if (argc < 3)
  {
     printf ("usage: LiveVideo <sec/frame>    \
<total frames>\n");
     exit(2);
  }

  /* open window */
  foreground();
  prefsize(640, 480);
    still_win = winopen("Grabbed Frame");
  RGBmode();
  gconfig();
  pixmode (PM_SIZE, 32);

  prefsize(640, 480);
    live_win = winopen("Live Video");


  /* open video device */
  if ((V = svOpenVideo()) == NULL)
```

```
{
  svPerror("open");
  exit(1);
}

/* associate video input with GL window */
if (svBindGLWindow(V, live_win,
  SV_IN_REPLACE) < 0)
{
  svPerror("bind gl window");
  svCloseVideo(V);
  exit(1);
  }

capture_period = atoi (argv[1]);
total_frames = atoi (argv[2]);
svci.width  = 640;
svci.height = 480;
svci.format = SV_YUV411_FRAMES;
svci.size   = 2;
svci.samplingrate = 30;
        /* frame rate = 1 frame/sec. */

/* event loop */
hz = getgdesc(GD_TIMERHZ);
noise(TIMER0, hz);
qdevice(LEFTMOUSE);
qdevice(TIMER0);
qdevice(ESCKEY);
  qdevice(WINQUIT);
  qdevice(WINSHUT);

  while (1)
{
  dev = qread(&val);
  switch (dev)
  {
    case LEFTMOUSE:
    if (val != 1)  /* grab on key press. */
      break;
    if (svInitContinuousCapture(V, &svci)< 0)
    {
      svPerror("init cap");
      exit(1);
    }
    break;

    case TIMER0:
    {
      long fieldID;

      svGetCaptureData(V, &captureData,
        &fieldID);
      if (captureData)
      {
      svYUVtoRGB(TRUE, captureData,
            (long *)rgbbuf,
         svci.width, svci.height);
        svUnlockCaptureData(V, captureData);

      if((i%capture_period)==0 &&
        i<(total_frames-1)*capture_period+1)
      {
        winset (still_win);
          lrectwrite(0, 0, svci.width-1,
            svci.height-1, (unsigned long *)rgbbuf);
          out_file = con_num_to_str(GRABFRAME,
            4, fieldID);
          dump_image (out_file, rgbbuf);
          winset (live_win);
        }
        ++i;
        if (i >= ((total_frames-1)*capture_period+1))
          svEndContinuousCapture(V);
        }
        }
        break;

      case ESCKEY:
          if (val)   /* exit on key up */
        break;

      case WINQUIT:
      case WINSHUT:
        if (i < ((total_frames-1)*capture_period+1))
          svEndContinuousCapture(V);
          svCloseVideo(V);
         winclose(still_win);
         winclose(live_win);
          exit(0);
          break;
    }
    }
}
```

```
/*** FindCenters.c        9/20/93                    ***
 *                                                    *
 *  image processing to obtain bubble centers.        *
 *  Further Improvements if possible:                 *
 *  1. use scale() to zoom in and out image.          *
 *  2. make scroll bar to view zoomed image.          *
 *  3. save hand corrected image at either zoom
 *     in or out mode.                                */

#include <stdio.h>
#include <string.h>
#include <stdlib.h>
#include <math.h>
#include <gl/gl.h>
#include <gl/image.h>
#include
</usr/people/4Dgifts/iristools/include/izoom.h>
#include <gl/device.h>

#define X    0
#define Y    1
#define FALSE 0
#define TRUE  1

unsigned long *imgbuf;
unsigned short  parray[480][640];
short row[640], buf[20];
int  menu, size;
IMAGE *aimage, *bimage;
long  ctrx, ctry;

void black_and_white_image (char *in_file,
```

```
        char *out_file)
{
  IMAGE *in_img, *out_img;
  short thresh=232, sbuf[640];
  int  i, j, ix, iy, x, y;
  int rc;
  char *tmp_file;

  in_img = iopen (in_file, "r");
    if(!in_img)
  {
    fprintf(stderr,"bw_image: can't open image \
file %s\n",in_file);
    exit(1);
    }

  out_img = iopen(out_file,"w",RLE(1),2,
            640,480);

  /* store pixel values in an array for intensity
      equalization */
  for(y=0; y < 480; y++)
  {
     getrow(in_img, row, y, 0);
    for(x=0; x < 640; x++)
      parray[y][x] = row[x];
  }
  iclose(in_img);

  /* intensity equalization */
  for (j = 0; j < 23; ++j)
  {
    for (i = 0; i < 31; ++i)
    {
      /* find average grayscale value of area
          20pixels x 20pixels */
      rc = 0;
      for ( iy=10+20*j; iy < 10+20*(j+1); iy++)
        for (ix=10+20*i; ix < 10+20*(i+1); ix++)
        rc += parray[iy][ix];
      rc = rc/400.0 + 0.5;

      /* subtract average grayscale value for each
          small image */
      for ( iy=10+20*j; iy < 10+20*(j+1); iy++)
        for (ix=10+20*i; ix < 10+20*(i+1); ix++)
        {
        parray[iy][ix] = parray[iy][ix] - rc + 255;
            /* +255 to make parray positive */
        if (parray[iy][ix] < thresh)
              /* threshold image */
            parray[iy][ix] = 0;
        else
            parray[iy][ix] = 255;
        }
    }
  }

/* set edges white to reduce equalization error and
    save computer time */
for(ix=0; ix<640; ix++)
{
  for(iy=0; iy<10; iy++)
    parray[iy][ix]=255;
  for(iy=470; iy<480; iy++)
    parray[iy][ix]=255;
  }
  for(iy=10; iy<470; iy++)
  {
    for(ix=0; ix<10; ix++)
      parray[iy][ix]=255;
    for(ix=630; ix<640; ix++)
      parray[iy][ix]=255;
  }

  /* write thresholded image to file and display it */
  for(y=0; y < 480; y++)
  {
    for(x=0; x < 640; x++)
      row[x] = parray[y][x];
    putrow(out_img, row, y, 0);
  }
  iclose(out_img);
    imgbuf = (unsigned long *)
malloc(307200*sizeof(long));
  imgbuf = (unsigned long *)
longimagedata(out_file);
  lrectwrite(0,0,639,479,(unsigned long *)imgbuf);
  free(imgbuf);
}

int getimgrow(short *xbuf, int y)
{
   getrow(aimage,xbuf,y,0);
}

int putimgrow(short *xbuf, int y)
{
   putrow(bimage,xbuf,y,0);
}

void zoom_image(char *in_file, char *out_file,
    float zoom_factor)
{
  int anx, any, bnx, bny;

  aimage = iopen(in_file, "r");

  anx = aimage->xsize;
  any = aimage->ysize;
  bnx = anx * zoom_factor;
  bny = any * zoom_factor;

  bimage = iopen(out_file, "w", RLE(1), 2,
           bnx, bny);
  filterzoom(getimgrow, putimgrow, anx, any, bnx,
           bny, IMPULSE,1.0);
  iclose(aimage);
  iclose(bimage);

  winconstraints();
  if (zoom_factor == 1.5)
  {
    winconstraints();
      prefposition(20, 979, 10, 729);
    winconstraints();
  }
  else
```

```
  {
    winconstraints();
      prefposition(180, 819, 90, 569);
    winconstraints();
  }
  if(REDRAW)
    reshapeviewport();
    imgbuf = (unsigned long *)
malloc(bnx*bny*sizeof(long));
  imgbuf = (unsigned long *)
longimagedata(out_file);
  lrectwrite(0,0,bnx-1,bny-1, (unsigned long
*)imgbuf);
}

void remove_dirts(short p[],short gray_value)
{
  long org[2];
  int i;
  short sqrdata[4][2], erasor_size = 4;

  ortho2(19.5, 979.5, 9.5, 729.5);
  sqrdata[0][X]=p[X];
  sqrdata[0][Y]=p[Y];
  sqrdata[1][X]=p[X]+erasor_size;
  sqrdata[1][Y]=p[Y];
  sqrdata[2][X]=p[X]+erasor_size;
  sqrdata[2][Y]=p[Y]+erasor_size;
  sqrdata[3][X]=p[X];
  sqrdata[3][Y]=p[Y]+erasor_size;
  RGBcolor(gray_value, gray_value, gray_value);
  bgnpolygon();
  for(i = 0; i <4; i++)
    v2s(sqrdata[i]);
  endpolygon();
}

void dump_image(char *out_file, unsigned long
      *data, short xsize, short ysize)
{
  IMAGE *image;
  short obuf[960];
  int x, y;

  image = iopen(out_file, "w", RLE(1), 2, xsize,
          ysize);
    for (y = 0; y < ysize; y++)
  {
    for (x = 0; x < xsize; x++)
    {
        obuf[x] = *data;
        data++;
    }
    putrow(image, obuf, y, 0);
  }
    iclose(image);
}

/* recursive function to extract center of a black
    area. */
void find_center_of_a_bubble(int x, int y)
{
  int a, b, i;
  int left_edge, right_edge;

  /* find left edge */
  a=x;
  left_edge=FALSE;
  while(left_edge == FALSE)
  {
    if(parray[y][a-1]==0)
      a -= 1;
    if(parray[y][a-1] != 0)
      left_edge = TRUE;
  }

  /* find right edge */
  b=x;
  right_edge=FALSE;
  while(right_edge == FALSE)
  {
    if(parray[y][b+1]==0)
      b += 1;
    if(parray[y][b+1] != 0)
      right_edge =TRUE;
  }

  /* count number of black pixels in row y and sum
      center coordinates */
  for(i=a; i<=b; i++)
  {
    parray[y][i]=255;
    size += 1;
    ctrx += i;
    ctry += y;
  }

  for(i=a; i<=b; i++)
  {
    if(parray[y-1][i]==0)
      find_center_of_a_bubble(i, y-1);
    if(parray[y+1][i]==0)
      find_center_of_a_bubble(i, y+1);
  }
}

/* average to obtain positions of center of        *
*   individual black area, display the extracted    *
*   bubble centers on screen and store center       *
*   coordinates in data file.                      */

void find_centers(char *in_file, char *data_file)
{
  IMAGE *image;
  int   x, y;
  int   filter = 10, total = 0, avesize=0;
  FILE *fp;
  short vert[4][2]={{199, 109}, {800, 109},
      {800, 550}, {199, 550}};

  /* read image to a 2d array */
  image = iopen(in_file, "r");
  for(y=0; y<480; y++)
  {
    getrow(image, row, y, 0);
    for(x=0; x<640; x++)
      parray[y][x]=row[x];
  }
```

```
iclose(image);

/* set boundaries of coordinates of
   find_center_of_a_bubble */
for(x=0; x<640; x++)
{
  parray[0][x]=255;
  parray[479][x]=255;
}
for(y=1; y<479; y++)
{
  parray[y][0]=255;
  parray[y][639]=255;
}

/* clear black area along edges, including those
     within 440x600 but connected
   to the edges. */
for(y=0; y<21; y++)
  for(x=0; x<640; x++)
    if (parray[y][x]==0)
    {
      ctrx = 0;
      ctry = 0;
      size = 0;
      find_center_of_a_bubble(x, y);
    }

for(y=20; y<480; y++)
  for(x=619; x<640; x++)
    if (parray[y][x]==0)
    {
      ctrx = 0;
      ctry = 0;
      size = 0;
      find_center_of_a_bubble(x, y);
    }

for(y=459; y<480; y++)
  for(x=0; x<620; x++)
    if (parray[y][x]==0)
    {
      ctrx = 0;
      ctry = 0;
      size = 0;
      find_center_of_a_bubble(x, y);
    }

for(y=20; y<460; y++)
  for(x=0; x<21; x++)
    if (parray[y][x]==0)
    {
      ctrx = 0;
      ctry = 0;
      size = 0;
      find_center_of_a_bubble(x, y);
    }

fp = fopen(data_file, "w");

/* find bubble centers */
for(y=20; y<460; y++)
  for(x=20; x<620; x++)
    if (parray[y][x]==0)
    {
      ctrx = 0;
      ctry = 0;
      size = 0;
      find_center_of_a_bubble(x, y);
      if(size>=filter)  /* remove small dirts */
      {
        total += 1;   /* count number of bubbles
                         on the image */
        fprintf(fp, "%10.6f %10.6f\n",
          (float)ctrx/size, (float)ctry/size);
                    /* unit: pixels */
        ctrx = (float)ctrx/size + 0.5;
        ctry = (float)ctry/size + 0.5;
        avesize += size;
        /* set grayvalue of bubble center to 1 to
           avoid endless loop */
        parray[ctry][ctrx] = 1;
      }
    }
  fprintf(fp, "%10.6f %10.6f\n", 0.0, 0.0);
  fprintf(fp, "%4i %4i\n", total, avesize/total);
  fclose(fp);

  /* display bubble centers. */
  image = iopen("bw.tmp", "w", RLE(1), 2, 640,
480);
  for(y=0; y<480; y++)
  {
    for(x=0; x<640; x++)
      row[x]=parray[y][x];
    putrow(image, row, y, 0);
  }
  iclose(image);
    imgbuf = (unsigned long *)
malloc(307200*sizeof(long));
  imgbuf = (unsigned long *)
longimagedata("bw.tmp");
  lrectwrite(0, 0, 639, 479,
    (unsigned long *)imgbuf);

  ortho2(179.5, 819.5, 89.5, 569.5);
  RGBcolor(0,0,0);
  bgnline();
    v2s(vert[0]);
    v2s(vert[1]);
    v2s(vert[2]);
    v2s(vert[3]);
    v2s(vert[0]);
  endline();
}

void define_menus()
{
  menu = newpup();
  addtopup(menu, "BLACK AND WHITE", 0);
  addtopup(menu, "ZOOM IN", 0);
  addtopup(menu, "SAVE AND ZOOM OUT", 0);
  addtopup(menu, "FIND CENTERS", 0);
}

main(int argc, char *argv[])
{
  long win, dev;
```

```
  short val, mval[2], sel;
  char out_file[15] = {"bw."},
centers_file[15]={"ctrs."};
  int leftmouse_down = 0, leftshiftkey_down = 0;

  if (argc < 2)
  {
    printf ("usage: FindCenters <input \
filename>\n");
    exit(1);
  }

  /* allocate the memory for the pixel data to be
      then fed to lrectwrite */
    imgbuf = (unsigned long *)
malloc(307200*sizeof(long));
  imgbuf = (unsigned long *)
longimagedata(argv[1]);

  /* open window and set display mode */
  foreground();
  minsize(640, 480);
  win = winopen ("Find Bubble Centers");
  RGBmode();
  gconfig();
  define_menus();

  /* draw original image */
  lrectwrite(0,0,639,479,(unsigned long *)imgbuf);
  free(imgbuf);

  out_file[3] = *(argv[1] + 4);
  out_file[4] = *(argv[1] + 5);
  out_file[5] = *(argv[1] + 6);
  out_file[6] = *(argv[1] + 7);
  out_file[7] = *(argv[1] + 8);

  centers_file[5] = *(argv[1] + 4);
  centers_file[6] = *(argv[1] + 5);
  centers_file[7] = *(argv[1] + 6);
  centers_file[8] = *(argv[1] + 7);
  centers_file[9] = *(argv[1] + 8);

  /* event loop */
  qdevice(LEFTMOUSE);
  qdevice(LEFTSHIFTKEY);
  qdevice(MOUSEX);
  qdevice(MOUSEY);
  qdevice(MENUBUTTON);
  qdevice(ESCKEY);
    qdevice(WINQUIT);
    qdevice(WINSHUT);
    while (1)
  {
    dev = qread(&val);
    switch (dev)
    {
      case MENUBUTTON:
        if (val)  switch(sel = dopup(menu))
        {
          case 1: /* obtain black and white image */
            black_and_white_image (argv[1],
                out_file);
            break;
          case 2: /* zoom out */
             zoom_image(out_file, "bw.tmp", 1.5);
            break;

          case 3: /* save and zoom in */
            lrectread(0, 0, 959, 719,
              (unsigned long *)imgbuf);
            dump_image("bw.tmp", imgbuf, 960,
                720);
            free(imgbuf);
            zoom_image("bw.tmp", out_file,
                0.666667);
            break;

          case 4: /* find centers */
             find_centers(out_file, centers_file);
            lrectread(0, 0, 639, 479,
              (unsigned long *)imgbuf);
            dump_image("bw.tmp", imgbuf, 640,
              480);
            free(imgbuf);
            break;
        }
        break;

      case LEFTMOUSE:
        leftmouse_down = val;
        break;

      case LEFTSHIFTKEY:
        leftshiftkey_down = val;
        break;

      case MOUSEX:
        mval[X] = val;
        break;

      case MOUSEY:
        mval[Y] = val;
        if(leftmouse_down)
        {
        if(leftshiftkey_down)
          remove_dirts(mval,0);
        else
          remove_dirts(mval,255);
        }
        switch(sel)
        break;

      case ESCKEY:
         if (val)    /* exit on key up */
        break;

      case WINQUIT:
      case WINSHUT:
        winclose(win);
        freepup(menu);
          exit(0);
          break;
    }
  }
}
```

```
/*** StrucFuncw.c        6/5/95                ***
 *                                              *
 * calculates structure factor of the bubble array .  *
 * A Hanning window is used to get rid of effect of  *
 * finite system.                               *
 */

#include <stdio.h>
#include <stdlib.h>
#include <math.h>
#include <string.h>

struct pt
{
  float x;
  float y;
  float d;
  float w;
};

int   total;
struct pt *ctrlist;
char  *ctr_file;

void read_in(char *in_file);
void compute_structure_function();

main(int argc, char *argv[])
{
  if(argc < 2)
  {
     printf("usage: StrucFuncw ctrs.nnnnn.nn\n");
    exit(1);
  }

  ctr_file=argv[1];
  read_in(ctr_file);
  compute_structure_function();
}

void read_in(char *in_file)
{
  int      tmp;
  float    lsp;
  struct pt  ctr, *ptr;
  FILE    *fp;

  fp=fopen(in_file, "r");
  fscanf(fp,"%i %f",&total, &lsp);

  ctrlist=(struct pt *)malloc(total*sizeof(ctr));
  if(ctrlist==NULL)
  {
    printf("malloc failed.\n");
    exit(2);
  }

  for(ptr=ctrlist;ptr<ctrlist+total;ptr++)
  {
    fscanf(fp,"%f %f %i",&ptr->x,&ptr->y,&tmp);
    ptr->x-=319.5;
       /* in order to use a Hanning window */
    ptr->y-=239.5;
    ptr->d=sqrtf(ptr->x*ptr->x+ptr->y*ptr->y);
    ptr->w=0.5*(1.0+cosf(0.0142799*ptr->d));
  }
}

void compute_structure_function()
{
  int   i, j, l;
  float  kx, ky, k0, s1, s2, s3, s4, kxdx, kydy;
  FILE *fp;

  strcat(ctr_file,".sw");
  fp=fopen(ctr_file,"w");
  fprintf(fp,"kx      ky      s       log(s)\n");

  k0=1.0/50.0;   /* last number is bin size of k */

  s1=0.0;
  for(l=0;l<total;l++)
  if(fabsf((ctrlist+l)->d)<220)
    s1+=(ctrlist+l)->w;
  s1=s1*s1;
  s2=log10f(s1);
  fprintf(fp,"%-9.4f %9.4f %10.2f %10.4f\n",
       0.0,0.0,s1,s2);

  for(i=1;i<=50;i++)
  {          /* upper limit is bin size of k */
    kx=i*k0;
    s1=0.0;
    s2=0.0;
    s3=0.0;
    s4=0.0;
    for(l=0;l<total;l++)
   if(fabsf((ctrlist+l)->d)<220)
   {
      kxdx=kx*((ctrlist+l)->x);  /* ky=0 */
      s1+=(ctrlist+l)->w*fcos(kxdx);
      s2+=(ctrlist+l)->w*fsin(kxdx);
      kydy=kx*((ctrlist+l)->y);  /* kx=0 */
      s3+=(ctrlist+l)->w*fcos(kydy);
      s4+=(ctrlist+l)->w*fsin(kydy);
   }
    s1=s1*s1+s2*s2;
    s2=log10f(s1);
    s3=s3*s3+s4*s4;
    s4=log10f(s3);
    fprintf(fp,"%-9.4f %9.4f %10.2f %10.4f\n",
       kx,0.0,s1,s2);
    fprintf(fp,"%-9.4f %9.4f %10.2f %10.4f\n",
       -kx,0.0,s1,s2);
    fprintf(fp,"%-9.4f %9.4f %10.2f %10.4f\n",
       0.0,kx,s3,s4);
    fprintf(fp,"%-9.4f %9.4f %10.2f %10.4f\n",
       0.0,-kx,s3,s4);
}


for(i=1;i<=50;i++) /* kx !=0, ky !=0 */
{
  kx=i*k0;
  for(j=1;j<=50;j++)
 {
 ky=j*k0;
 s1=0.0;
```

```
    s2=0.0;
      s3=0.0;
      s4=0.0;
    for(l=0;l<total;l++)
    if(fabsf((ctrlist+l)->d)<220)
    {
       kxdx=kx*((ctrlist+l)->x);
       kydy=ky*((ctrlist+l)->y);
       s1+=(ctrlist+l)->w*fcos(kxdx+kydy);
       s2+=(ctrlist+l)->w*fsin(kxdx+kydy);
       s3+=(ctrlist+l)->w*fcos(-kxdx+kydy);
       s4+=(ctrlist+l)->w*fsin(-kxdx+kydy);
    }
      s1=s1*s1+s2*s2;
    s2=log10f(s1);
      s3=s3*s3+s4*s4;
    s4=log10f(s3);
    fprintf(fp,"%-9.4f %9.4f %10.2f %10.4f\n",
        kx,ky,s1,s2);
    fprintf(fp,"%-9.4f %9.4f %10.2f %10.4f\n",
        -kx,-ky,s1,s2);
    fprintf(fp,"%-9.4f %9.4f %10.2f %10.4f\n",
        -kx,ky,s3,s4);
    fprintf(fp,"%-9.4f %9.4f %10.2f %10.4f\n",
        kx,-ky,s3,s4);
    }
  }
  fclose(fp);
  free(ctrlist);
}
```

REFERENCES

Babcock, K. L., and R. M. Westervelt, Phys. Rev. Lett. **63**, 175 (1989a).

Babcock, K. L., *Cellular Domain Patterns in Magnetic Garnet Films*, Ph.D. thesis (Department of Physics, Harvard University, Cambridge, MA, 1989b).

Babcock, K. L., R. Seshadri, and R. M. Westervelt, Phys. Rev. A **41**, 1952 (1990).

Babcock, K. L., and R. M. Westervelt, Phys. Rev. Lett. **64**, 2168 (1990).

Balents, L., and D. R. Nelson, Phys. Rev. Lett. **73**, 2618 (1994).

Balents, L., and S. H. Simon, Phys. Rev. B **51**, 6515 (1995).

Balents, L., and D. R. Nelson, Phys. Rev. B **52**, 12951 (1995).

Batrouni, G. G., and T. Hwa, Phys. Rev. Lett. **72**, 4133 (1994).

Belt, R. F., and J. B. Ings, SPIE J. **753**, 142 (1987).

Bishop, D. J., P. L. Gammel, D. A. Huse, and C. A. Murray, Science **255**, 165 (1992).

Bobeck, A. H., Bell Syst. Tech. J. **46**, 1901 (1967).

Bruinsma, G., and G. Aeppli, Phys. Rev. Lett. **52**, 1547 (1984).

Buhrer, C. F., J. Appl. Phys. **40**, 4500 (1969).

Burkov, S. E., and V. L. Pokrovskii, JETP Lett. **32**, 263 (1980).

Burkov, S. E., and V. L. Pokrovsky, J. Low Temp. Phys. **44**, 423 (1981).

Cape, J. A., and G. W. Lehman, J. Appl. Phys. **42**, 5732 (1971).

Carlson, J. M., and J. S. Langer, Phys. Rev. Lett. **62**, 2632 (1989).

Carraro, C., and D. R. Nelson, preprint, 1996.

Chikazumi, S., *Physics of Magnetism* (Wiley, New York, 1964).

Chinn, M. D., and S. C. Fain, Jr., Phys. Rev. Lett. **39**, 146 (1977).

Coppersmith, S. N., D. S. Fisher, B. I. Halperin, P. A. Lee, and W. F. Brinkman, Phys. Rev. Lett. **46**, 549 (1981).

Coppersmith, S. N., D. S. Fisher, B. I. Halperin, P. A. Lee, and W. F. Brinkman, Phys. Rev. B **25**, 349 (1982).

Coppersmith, S. N., Phys. Rev. Lett. **65**, 1044 (1990).

Daldini, O., P. Martinoli, J. L. Olsen and G. Berner, Phys. Rev. Lett. **32**, 218 (1974).

Deeter, M. N., Appl. Optics **35**, 154 (1996).

Eppler, W. R., and M. H. Kryder, J. Phys. and Chem. of Sol. **56**, 1479 (1995).

Eschenfelder, A. H., *Magnetic Bubble Technology, 2nd Ed.* (Springer-Verlag, New York, 1981).

Feder, H. J. S., and J. Feder, Phys. Rev. Lett. **66**, 2669 (1991).

Feigel'man, M. V., V. B. Geshkenbein, A. I. Larkin, and V. M. Vinokur, Phys. Rev. Lett. **63**, 2303 (1989).

Fisher, D. S., Phys. Rev. Lett. **50**, 1486 (1983).

Fisher, D. S., Physica B **126**, 409 (1984).

Fisher, D. S., Phys. Rev. B **31**, 1396 (1985).

Fisher, D. S., in *Nonlinearity in Condensed Matter*, edited by A. P. Bishop, D. K. Campbell, P. Kumar, and S. E. Trullinger (Springer-Verlag, New York, 1987).

Fisher, D. S., M. P. A. Fisher, and D. A. Huse, Phys. Rev. B **43**, 130 (1991).

Fisher, M. P. A., T. A. Tokuyasu, and A. P. Young, Phys. Rev. Lett. **66**, 2931 (1991).

Fortune, S., Algorithmica **2**, 153 (1987).

Fu, H., Z. Yan, S. K. Lee, and M. Mansuripur, J. Appl. Phys. **78**, 4076 (1995).

Fukuyama, H., and P. A. Lee, Phys. Rev. B **17**, 535 (1978).

Garel, T., and S. Doniach, Phys. Rev. B **26**, 325 (1982).

Geller, S., H. J. Williams, G. P. Espinosa, R. C. Sherwood, and M. A. Gilleo, Appl. Phys. Lett. **3**, 21 (1963).

Grier, D. G., C. A. Murray, C. A. Bolle, P. L. Gammel, and D. J. Bishop, Phys. Rev. Lett. **66**, 2270 (1991).

Grinstein, G., and J. Fernandez, Phys. Rev. B **29**, 6389 (1984).

Grüner, G., Rev. Mod. Phys. **60**, 1129 (1988).

Hecht, E., *Optics, 2nd Ed.* (Addison-Wesley, Reading, MA, 1987).

Höfelt, M. H. H., J. Appl. Phys. **44**, 414 (1973).

Horn, P. M., R. J. Birgeneau, P. Heiney, and E. M. Hammonds, Phys. Rev. Lett. **41**, 461 (1978).

Hu, J., and R. M. Westervelt, Phys. Rev. B **51**, 17279 (1995).

Hu, J., and R. M. Westervelt, submitted to Phys. Rev. B, (1996).

Hull, D., and D. J. Bacon, *Introduction to Dislocations, 3rd Ed.*, International Series on Materials Science and Technology, Vol. 37 (Pergamon Press, New York, 1984).

Huse, D. A., M. P. A. Fisher, and D. S. Fisher, Nature **358**, 553 (1992).

Imry, Y., and S. Ma, Phys. Rev. Lett. **35**, 1399 (1975).

Itzler, M. A., and M. Tinkham, Phys. Rev. B **51**, 435 (1995a).

Itzler, M. A., and M. Tinkham, Phys. Rev. B **51**, 9411 (1995b).

Ivlev, B. I., and N. B. Kopnin, J. Low Temp. Phys. **80**, 161 (1990).

Ivlev, B. I., N. B. Kopnin, and V. L. Pokrovsky, J. Low Temp. Phys. **80**, 187 (1990).

Jensen, H. J., A. Brass, and A. J. Berlinsky, Phys. Rev. Lett. **60**, 1676 (1988a).

Jensen, H. J., A. Brass, Y. Brechet, and A. J. Berlinsky, Phys. Rev. B **38**, 9235 (1988b).

Kittel, C., Phys. Rev. **70**, 965 (1946).

Kittel, C., Rev. Mod. Phys. **21**, 541 (1949).

Ko, M., and E. Garmire, Appl. Optics **34**, 1692 (1995).

Koch, R. H., V. Foglietti, W. J. Gallagher, G. Koren, A. Gupta, and M. P. A. Fisher, Phys. Rev. Lett. **63**, 1511 (1989).

Kooy, C., Philips Tech. Rev. **19**, 286 (1958).

Kosterlitz, J. M., and D. J. Thouless, J. Phys. C **6**, 1181 (1973).

Kwok, W. K., J. Fendrich, U. Welp, S. fleshler, J. Downey, and G. W. Crabtree, Phys. Rev. Lett. **72**, 1088 (1994).

Landau, L., and E. Lifshitz, Physik. Zeits. Sowjetunion **8**, 153 (1935).

Landau, L. D., and E. M. Lifshitz, *Theory of Elasticity*, Vol. 7 of Course of Theoretical Physics, 3rd English Ed. (Pergamon, New York, 1986).

Lee, P. A., and T. M. Rice, Phys. Rev. B **19**, 3970 (1979).

Levitov, L. S., Phys. Rev. Lett. **66**, 224 (1991).

Levy, M., R. Scarmozzino, R. M. Osgood, Jr., R. Wolfe, F. J. Cadieu, H. Hedge, C. J. Gutierrez, and G. A. Prinz, J. Appl. Phys. **75**, 6286 (1994).

Malozemoff, A. P., and J. C. Slonczewski, *Magnetic Domain Walls in Bubble Materials* (Academic Press, New York, 1979).

Marchetti, M. C., and D. R. Nelson, Phys. Rev. B **42**, 9938 (1990).

Marchetti, M. C., and D. R. Nelson, Physica C **174**, 40 (1991).

Martinoli, P., H. Beck, M. Nsabimana, and G.-A. Racine, Physica B **107**, 455 (1981).

Molho, P., J. L. Porteseil, Y. Souche, J. Gouzerh, and J. C. S. Levy, J. Appl. Phys. **61**, 4188 (1987).

Moncton, D. E., P. W. Stephens, R. J. Birgeneau, P. M. Horn and G. S. Brown, Phys. Rev. Lett. **46**, 1533 (1981).

Mori, H., and Y. Asahara, Appl. Optics **35**, 1083 (1996).

Murray, C. A., and D. H. Van Winkle, Phys. Rev. Lett. **58**, 1200 (1987).

Murray, C. A., and R. A. Wenk, Phys. Rev. Lett. **62**, 1643 (1989).

Narayan, O., and D. S. Fisher, Phys. Rev. B **49**, 9469 (1994).

Nelson, D. R., and B. I. Halperin, Phys. Rev. B **19**, 2457 (1979).

Nelson, D. R., M. Rubinstein, and F. Spaepen, Phil. Mag. A **46**, 105 (1982).

Nelson, D. R., and V. M. Vinokur, Phys. Rev. Lett. **68**, 2398 (1992).

O'Dell, T. H., Rep. Prog. Phys. **49**, 589 (1986).

Pokrovskii, V. L., and A. L. Talapov, Sov. Phys. JETP **48**(3), 579 (1978).

Pokrovsky, V. L., and A. L. Talapov, Phys. Rev. Lett. **42**, 65 (1979).

Reichhardt, C., J. Groth, C. J. Olson, S. Field, and F. Nori, preprint (1996).

Schulz, H. J., Phys. Rev. B **22**, 5274 (1980).

Schwartz, M., *Principles of Electrodynamics* (Dover, New York, 1972).

Seshadri, R., and R. M. Westervelt, Phys. Rev. Lett. **66**, 2774 (1991).

Seshadri, R., *Melting, Pinning, and Forced Flow of Two-Dimensional Magnetic Bubble Arrays,* Ph.D. thesis (Department of Physics, Harvard University, Cambridge, MA, 1992a).

Seshadri, R., and R. M. Westervelt, Phys. Rev. B **46**, 5142 (1992b).

Seshadri, R., and R. M. Westervelt, Phys. Rev. B **46**, 5150 (1992c).

Seshadri, R., and R. M. Westervelt, Phys. Rev. Lett. **70**, 234 (1993a).

Seshadri, R., and R. M. Westervelt, Physica D **66**, 223 (1993b).

Seshadri, R., and R. M. Westervelt, Phys. Rev. B 47, 8620 (1993c).

Seul, M., L. R. Monar, L. O'Gorman, and R. Wolfe, Science **254**, 1616 (1991).

Seul, M., and R. Wolfe, Phys. Rev. Lett. **68**, 2460 (1992a).

Seul, M., and R. Wolfe, Phys. Rev. B **46**, 7519 (1992b).

Seul, M., and R. Wolfe, Phys. Rev. B **46**, 7534 (1992c).

Seul, M., and C. A. Murray, Science **262**, 558 (1993).

Seul, M., J. Phys. I France **4**, 319 (1994).

Stokes, J. B., D. A. Weitz, J. P. Gollub, A. Dougherty, M. O. Robbins, P. M. Chaikin, and H. M. Lindsay, Phys. Rev. Lett. **57**, 1718 (1986).

Thiele, A. A., Bell Syst. Tech. J. **48**, 3287 (1969).

Thiele, A. A., Bell Syst. Tech. J. **50**, 725 (1971).

Tsai, Y.-C., and Y. Shapir, Phys. Rev. Lett. **69**, 1773 (1992).

Vallette, D. P., and J. P. Gollub, Phys. Rev. E **47**, 820 (1993).

Villain, J., in *Ordering in Strongly Fluctuating Condensed Matter Systems*, edited by T. Riste (Plenum, New York, 1980).

Villain, J., Phys. Rev. Lett. 52, 1543 (1984).

Woolhouse, G. R., and P. Chaudhari, Phil. Mag. **31**, 161 (1974).

Young, A. P., Phys. Rev. B **19**, 1855 (1979).